A Search for Pre-Transit Absorption Features in Spectra of Hot Jupiters

Dissertation
zur Erlangung der Würde des Doktors der Naturwissenschaften
der Fakultät für Mathematik, Informatik und Naturwissenschaften
Fachbereich Physik
der Universität Hamburg

vorgelegt von

Sebastian-Ingo Kohl aus Hamburg

Hamburg

2021

Gutachter der Dissertation:	Prof. Dr. J.H.M.M. Schmitt Prof. Dr. Klaus-Peter Schröder
Zusammensetzung der Prüfungskommission:	Prof. Dr. J.H.M.M. Schmitt Prof. Dr. Peter Hauschildt Prof. Dr. Jochen Liske Prof. Dr. Ansgar Reiners Prof. Dr. Robi Banerjee
Vorsitzender der Prüfungskommission:	Prof. Dr. Jochen Liske
Datum der Disputation:	12.01.2022
Vorsitzender des Fach-Promotionsausschusses PHYSIK:	Prof. Dr. Wolfgang Hansen
Leiter des Fachbereichs PHYSIK:	Prof. Dr. Günter H. W. Sigl
Dekan der Fakultät MIN:	Prof. Dr. Heinrich Graener

Abstract

In the past it was claimed that the transit of the hot Jupiter HD 189733 b is preceded by a bow shock. The authors arrived at this conclusion by the comparison of CaII H&K light curve with the light curves of the Balmer lines. While the former did not show any evidence for pre-transit absorption signals, the latter does show a distinct absorption signal preceding the planetary transit. The authors rule out a stellar origin because of the discrepancy of the CaII and Balmer lines. This work deals with the question if bow shocks are a ubiquitous phenomenon and if they are temporally stable. In the case of HD 189733 b no indications for bow shocks could be found in TIGRE data of the year 2017. Further, it could be shown that the existence of bow shocks cannot be proven in the planetary systems WASP-69, WASP-131, KELT-7 as well as KELT-20. Instead, the observational data allows to derive upper limits for the strengths of the bow shocks. These depend on the telescope and on the brightness of the host star and range between 2 und 6 mÅ. This is considerably lower than the value of 13mÅ postulated in the literature for HD 189733 b. For this reason the question is if an alternative explanation exists for the observed phenomena in the HD 189733 system. A possible explanation is stellar activity. An example are prominences of sufficient size and temperature. If they are sufficiently cool and extended they are faint in the CaII K light but bright in the Hα light. Similar problems can also occur during transit. An example are different transit observations of KELT-7 b. These show that the transit depths in Hα are variable. This variability is caused by active regions on the stellar surface. A fundamental problem for the interpretation of the observations is that the relevant extrasolar planetary systems cannot yet be spatially resolved although this is essential to explore the spatial structure of prominences of other stars. For this reason the astrophysical nature of the observed peculiarities currently remains an open question.
The absence of the bow shock allows to impose limits on the strength of the planetary magnetic field. The assumption that the bow shock occured before observations started yields planetary magnetic fields between 155G and more than 18kG. These values are significantly higher than the value of 4G of Jupiter and thus seem to be unrealistic. Alternatively, the passage of bow shock and planet could be temporally so close that the observation data cannot resolve the components. In this case the limits for the planetary magnetic field range between 3,2mG and 0,3G. On the other hand, these values seem to be unreasonable low.
The observed spectra not only depend on the physical processes in the planetary system, but are affected by various processes while on their way towards the spectrograph. First, the starlight has to traverse the interplanetary medium. If this possesses its own absorption lines, distorsions are introduced. For nearby stars such distorsions should be negligible. This assumption has been doubted in the literature and therefore it has been validated for a few examples. These show that a correct stellar model is essential to avoid misinterpretations. Another problem is the passage of stellar light through the atmosphere of the Earth. The atmosphere imprints various absorption lines on the stellar spectrum. This is especially problematic in the vicinity of the Hα line when stellar and telluric lines blend. These line blends yield an increase in the equivalent width of the Hα line. Its strength depends on the local meteorological condition and is therefore temporally variable.
All these observations require considerable accuracies of the spectrographs employed. Even small instrumental distorsions can lead to significant distorsions of the observed spectra. Especially spectrographs with a resolution around 20,000 are prone to this. For instance, a decrease in spectral resolution to 15,000 in combination with a radial velocity shift of +900m/s leads to an increase of the equivalent width of the Hα line by 5mÅ. Possible reasons for this are an increase in seeing in combination with thermal expansion of spectrograph components. If this happens during pre-transit phase such a signal can be misinterpreted as a planetary absorption feature. At higher spectral resolutions of about 80,000 these nuisances are on the order of 2mÅ and thus smaller.

Zusammenfassung

In der Vergangenheit wurde für den heißen Jupiter HD 189733 b behauptet, dass dessen Transit eine Bugstoßwelle vorausgeht. Dieses Ergebnis erhalten die Autoren durch den Vergleich der CaII H&K-Lichtkurve mit den Lichkurven der Balmer-Linien. Während Erstere keinerlei Anzeichen für Prätransitabsorptionssignale zeigt, zeigt letztere ein deutliches Absorptionssignal vor Beginn des Transits. Einen stellaren Ursprung schließen die Autoren aufgrund der Diskrepanz von CaII- und Balmer-Linien aus. Diese Arbeit widmet sich der Fragestellung, ob solche Bugstoßwellen ein allgemeines Phänomen und zeitlich stabil sind. Im Fall von HD 189733 konnten in TIGRE-Daten aus dem Jahr 2017 keine

Bugstoßwellen mehr gefunden werden. Es konnte weiterhin gezeigt werden, dass diese sich auch in den Planetensystemen WASP-69, WASP-131, KELT-7 sowie KELT-20 nicht nachweisen ließen. Stattdessen lassen sich aus den Beobachtungen obere Limits für deneren Stärke ableiten. Diese sind sowohl vom verwendeten Teleskop als auch von der Helligkeit des Zentralsterns abhängig und liegen zwischen 2 und 6 mÅ. Dies ist deutlich niedriger als der in der Literatur postulierte Wert von 13mÅ für HD 189733 b. Aus diesem Grund stellt sich die Frage, ob sich das beobachtete Phänomen bei HD 189733 auch anderweitig erklären lässt. Ein möglicher Erklärungsansatz ist hierbei stellare Aktivität. Beispielsweise könnten Protuberanzen geeigneter Größe und Temperatur zur Erklärung herangezogen werden. Sofern diese ausreichend kühl und ausgedehnt sind, sind diese sehr leuchtschwach im CaII K-Licht, hingegen hell im Hα-Licht. Ähnliche Probleme können sich auch während des Transits selbst ergeben. Beispielsweise haben Transitbeobachtungen von KELT-7 b gezeigt, dass dessen Transittiefe im Hα-Licht variabel ist. Eine Erklärung hierfür sind Aktivitätsgebiete auf dessen Oberfläche. Ein grundsätzliches Problem bei der Interpretation der Beoabchtungen ist, dass sich mit heutiger Technologie die untersuchten Planetensysteme noch nicht räumlich auflösen lassen, um beispielweise die räumliche Struktur von Protuberanzen bei anderen Sternen zu untersuchen. Aus diesem Grund muss zum jetzigen Zeitpunkt die astrophysikalische Natur der beobachteten Eigenheiten offen bleiben.
Das Fehlen der Bugstoßwelle innerhalb der beobachteten Transitphasen erlaubt Rückschlüsse über die Stärke des planetarischen Magnetfeldes zu ziehen. Unter der Annahme, dass die Bugstoßwelle vor Beginn der jeweiligen Beobachtungen auftrat, ergibt sich ein planetarisches Magnetfeld zwischen 155G und über 18kG. Diese Werte ist deutlich höher als der für Jupiter beobachtete Wert von 4G und erscheinen daher unrealistisch. Alternativ bestünde die Möglichkeit, dass die Passage von Bugstoßwelle und Planet zeitlich derart eng zusammenfallen, dass diese Komponenten in den Beobachtungsdaten nicht mehr aufgelöst werden können. In diesem Fall ergeben sich planetarische Magnetfelder zwischen 3,2mG und 0,3G. Diese Werte erscheinen jedoch abwegig niedrig.
Die beobachten Spektren hängen jedoch nicht ausschließlich von den physikalischen Prozessen in den betrachteten Planetensystemen ab, sondern sind auf ihrem Weg bis zum Spektrographen mehreren verfälschenden Einflüssen ausgesetzt. Zunächst muss das Sternlicht das interstellare Medium durchqueren. Sofern dieses eigene Absorptionslinien aufweist, führt dies zu entsprechenden Verfälschungen. Für nahe Sterne sollten eventuelle Absorptionslinien in den meisten Fällen allerdings schwach ausgeprägt sein. An dieser Annahme wurden jedoch Zweifel geäußert, sodass diesem Problem an einigen Beispielen auf den Grund gegangen wurde. Hierbei zeigt sich, dass eine korrekte Modellierung des stellaren Spektrums essentiell ist, um derartige Fehlinterpretationen zu verhindern. Ein weiteres Problem ergibt sich im Rahmen der Passage des Sternlichts durch die Erdatmosphäre. Diese fügt dem Spektrum eigene Linien hinzu. Insbesondere im Bereich der Hα-Linie können diese problematisch sein, wenn sich stellare und tellurische Linien überlagern. Hierdurch kommt es dann zu einer Erhöhung der Äquivalentbreite der Hα-Linie. Deren Stärke hängt von den lokalen meteorologischen Bedingungen ab und ist daher zeitlich variabel.
Alle diese Beobachtungen erfordern erhebliche Genauigkeiten der verwendeten Spektrographen. Bereits geringe instrumentelle Veränderungen können zu erheblichen Verfälschungen der beobachteten Spektren führen. Besonders betroffen sind hierbei Spektrographen mit Auflösungen um die 20.000. Beispielsweise kann eine Erniedrigung der effektiven Auflösung auf 15.000 in Kombination mit einer gleichzeitigen Radialgeschwindigkeitsverschiebung um +900m/s zu einer Erhöhung der Äquivalentbreite der Hα-Linie um 5mÅ führen. Mögliche Gründe hierfür sind eine Erhöhung des Seeings sowie thermische Ausdehnung von Bauteilen des Spektrographen. Passiert dies während der Prätransitphase, kann dieses Signal leicht als planetarische Absorption fehlinterpretiert werden. Bei höheren spektralen Auflösungen um die 80.000 sind die Störungen geriner und liegen bei etwa 2mÅ.

Contents

Chapter 1

Introduction

In the recent past, pre-transit absorption features in the spectra of HD 189733 b have been claimed by optical transmission spectroscopy (Cauley et al. 2015; Cauley et al. 2016). The authors identified absorption features in the Balmer light curves by transit spectroscopy that are not accompanied by corresponding features in the CaII H&K light curve. These they interpreted as bow shocks composed of exospheric hydrogen. Such features have been predicted before by Llama et al. 2013, Vidotto et al. 2010 and Vidotto et al. 2011. In a later publication, Cauley et al. 2017a found that this pre-transit absorption feature is not always present and that stellar activity might play a major role in this enigma and complicating the analysis. Also the results of other groups do not support the assumption of an absorption feature related to the planetary transit. For instance, Barnes et al. 2016 argue that peculiar signals during the pre-transit phase can indeed be a manifestation of stellar activity. It is also problematic that this phenomenon cannot be clearly identified in other planetary systems. For instance Yan and Henning 2018 show that the Hα transit light curve of KELT-9 b does not show any pre-transit absorption features. The same is also true for the transits of KELT-3 b and GJ 436 b (Cauley et al. 2017b). Especially interesting in this regard is a transit of WASP-12 b (Jensen et al. 2018). The authors claim a detection of absorption in Hα. In contrast, the Hβ light curve does not show statistically significant absorption. The aim of this work is to decide whether pre-transit phenomena are ubiquitous or whether they depend on specific properties of the extrasolar planetary system. Especially important in this context are host stars of spectral type A or earlier. Such stars do not show stellar activity (Fossati et al. 2018) and thus the interpretation of the results is potentially easier. However, the drawback is that the majority of planets is not found around these stars but around cooler stars (Ciardi 2020). To shed light on this question I investigate the pre-transit phases of different hot Jupiters. Because not only stellar activity compromises the analysis I also include the impact of interstellar absorption features and instrumental artifacts.
Interstellar absorption introduces absorption lines into stellar spectra (dubbed diffuse interstellar bands or abbreviated DIBs). If such a DIB is located close to a stellar line of interst the two components can produce a line blend. In extrasolar planetary systems the stellar line component is affected by radial velocity wobble due to the planet. In contrast, the DIB component does not follow this RV shift. McCall 2021 gives a comprehensive list of these DIBs in the spectrum of the distant star HD 183143. This work shows that some of the DIBs are found in the neighbourhood of the CaII or Balmer lines. If these are exceptionally strong towards some sightlines they potentially contaminate the stellar spectrum of a planetary host star.
On the one hand, the astrophysical processes discussed in this work require high accuracy. On the other hand spectra are systematically contaminated by telluric absorption features and instrumental artifacts. This raises the question if these systematic errors can contaminate the observation to such an extent that they dominate the observed signal.
The outline of this work is as follows: chapter 2 discusses the impact of telluric absorption features and instrumental artifacts on the spectroscopic observations. This chapter also introduces the instruments that were used to aquire the observations discussed in this work. Chapter 3 discusses the importance of the interplanetary medium for the observations of chromospheric lines. Chapter 4 presents a short summary of the theoretical foundation of bow shocks, discusses the selection criteria for the planetary sample regarded in this work and reconsiders the role of stellar activity in bow shock observations. Chapter 5 discusses the individual transit observations, sheds light on the challenges that particular observations impose and derives the properties of the pre-transit phase. Chapter 6 reviews the implications for the stellar magnetic field and chapter 7 summarizes the main points of this work.

I have published selected parts of my work during the course of this PhD thesis. The results concerning the diffuse interstellar bands in nearby stars have been published partially in Kohl et al. 2016 and the searches for the bow shock in the HD 189733 planetary system have been published in Kohl et al. 2018. For both publications I am the leading author. This implies that I carried out the data ayalysis steps and wrote the manuscript. Nevertheless, my coauthors contributed to this work by input to the manuscript, clarifying discussions and valuable feedback concerning data reduction and analysis steps.

Chapter 2

Spectral Artifacts

The term "Astronomical Spectroscopy" refers to the study of celestial objects by means of spectroscopy. By such studies one is usually solely interested in the intrinstic spectra of celestial sources. Unfortunately, the stellar light first has to pass through the earth's atmosphere. Here, seeing, telluric absorption lines and atmospheric light scattering will imprint its signatures on stellar spectra. Even after the light has reached the spectrograph further degradation might occur due to instrumental artifacts. These are for example radial velocity jitter, defocus and the spectrograph's blaze function. In this chapter I summarise the most important of them. These have to be considered when dealing with ground-based spectroscopic data.

2.1 Telluric lines

For high resolution spectroscopy the most important systematic error is caused by absorption lines of the Earth's atmosphere. An example is given in figure 2.1. It shows a model of the telluric transmission spectrum in the orange to red wavelength region. This wavelength region is covered by the red channel of the HEROS[1] spectrograph. It is clearly visible that telluric lines are not equally scattered over the whole spectrum but concentrated in certain wavelength regions. Here we see molecular oxygen absorption bands located around 6300 and 6900Å. The bands at 6500 and 7250Å are caused by water vapor. Several smaller bands at 5900Å and a wide depression on the left are absorption features of ozone. This model has been calculated with ESO's `molecfit` software package (Smette et al. 2015). `molecfit` directly derives transmission models from observed stellar spectra. Additionally, it uses meteorological data both from local weather stations and from satellite observations as inputs. Since weather stations can only record the meteorological parameters near the ground the latter is important for information about the higher layers of the atmosphere. This information comes from NOAA[2] weather satellites (Stein 2020). Because not all atmospheric parameters are continuously monitored these data are supplemented by a reference atmospheric profile. Further, the code takes into account the spectrograph's resolution, instrumental line profile (e.g. Gaussian line broadening) and local airmass. This information has to be combined with molecular line lists giving position, shape and strength of telluric lines. `molecfit` uses the `HITRAN` (high-resolution transmission) molecular database (Rothman et al. 2009) for this purpose. In combination with the meteorological parameters `molecfit` derives an initial transmission model. This model is used as a starting point for a χ^2 minimisation. Since not all wavelength ranges are equally affected by telluric lines the χ^2 minimisation should be restricted to regions with strong telluric features. In contrast, strong stellar lines should be excluded. This will not only lessen the computational expense but also improve the numerical stability. Another problem associated with stellar lines is that the depth of telluric lines will systematically be too low. Figure 2.1(middle panel) compares the HEROS observation of a K5III star to its best-fitting telluric model. The graphs reveal that several lines are not included in the model. Presumably, these are intrinsic features of the stellar source. For this reason the best solution albeit from a purely mathematical point of view is to decrease the continuum level and to reduce the depths of telluric lines. This will minimise the χ^2. Exclusion of stellar features will therefore lead to a physically meaningful best fit. In principle, the abundance of atmospheric constituents can be inferred from the width and depth of telluric lines. However, this is only possible if such lines are not saturated. An

[1] Further details about this instrument can be found in Schmitt et al. 2014.

[2] NOAA stands for "National Oceanic and Atmospheric Administration" and is the national weather service of the United States of America.

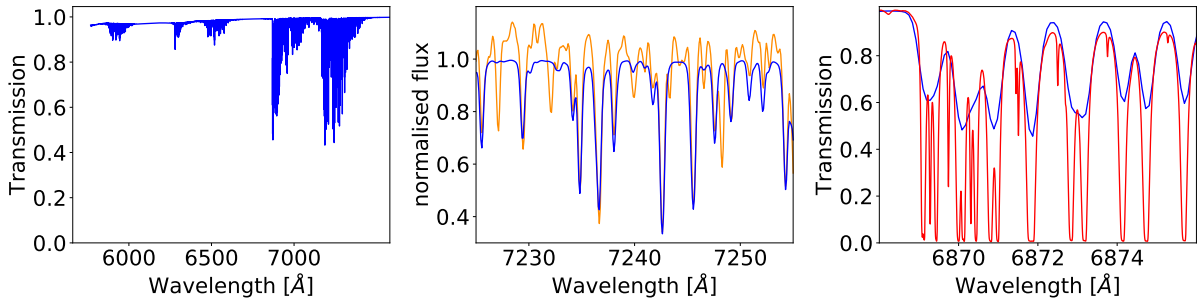

Figure 2.1: Left: Telluric transmission versus wavelength. Scattering processes are not included. Middle: Uncorrected HEROS observation(orange) versus telluric model(blue) for the K5III star HD 29139. Right: Detail of O_2 B band observed at $R \approx$20,000(blue) and $R \approx 10^6$(red).

example might illustrate this problem. The right panel of figure 2.1 shows a telluric region in detail. The red line shows an observed solar spectrum recorded with a resolution of 10^6 (Reiners et al. 2016). The blue line shows a HEROS solar observation. Because the HEROS spectrograph is not equipped with a solar telescope reflected moonlight is used instead. The spectral resolution is 20,000. From the HEROS data alone it is tempting to regard the telluric lines as being moderately deep. A comparison to the high resolution data shows unambiguously the saturation. In this case the line shape of the lower resolution data is completely governed by instrumental broadening. Note that the equivalent widths of the telluric lines are different due to the fact that HEROS is located 2.4km above sea level while Göttingen is located at a height of 150m and thus atmospheric absorption is different. In case of saturated lines a higher number of absorbers in the sightline will lead to a slight broadening of the line's wings. After instrumental broadening the strength of this effect will even be further reduced. Therefore, such small variations are often lost due to a finite signal to noise ratio and therefore the precision of width and depth values are often low.

2.1.1 Consequences of Line Blends

When working on astronomical spectra telluric lines are not only a cosmetic problem but might have far-reaching consequences on scientific conclusions. In figure 2.2 such a problematic scenario is depicted. It shows a blend between a strong broad stellar line and a small narrow telluric line. All lines shown in the plot are completely fictitious. One problem is the determination of equivalent widths (shaded areas in figure 2.2) of stellar lines. If the existence of the telluric component is ignored the measured equivalent width will be too high because the telluric component unintentionally contributes. In many situations the integration band is always located at the same position. Then, this offset may not be problematic. However, in other situations it is necessary to center such an integration band on a certain stellar line. The position of this line is varying during the observing run if stellar radial velocity has to be taken into account. If spectral resolution is high such telluric features can be separately modeled and thereby accounted for. In case of nosiy data or low spectral resolution as shown in the middle plot such an approach is not possible without a telluric absorption model at hand. Additionally, telluric lines will also systematically affect the determination of line positions. In the example discussed here the line minimum is now blueshifted by 6.8km/s. During the course of an observing run this wavelength shift will not be constant. First, due to the spin of the Earth and its motion around the sun the position of stellar lines will be Doppler shifted. In contrast, the positions of telluric lines will be constant at the 5-10m/s level (Reiners et al. 2016). Second, the strength of telluric lines will vary. For example, the relative humidity is generally time-dependent and therefore also the water vapor column above telescope. Especially in the low resolution example both factors will influence the exact position of the blended line minimum. At this point is should be emphasized that this example is somewhat pathologic. In realistic scenarios the problem will admittedly not be as severe as discussed here. Telluric lines might be further apart and not as strong as shown. Bearing in mind that current Doppler exoplanet search programs have RV accuracies below 2m/s (Fischer et al. 2016) such effects should be considered.

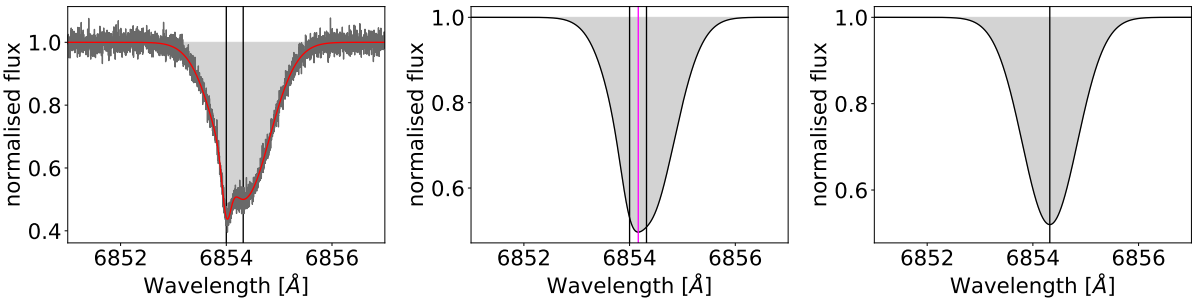

Figure 2.2: Left: Strong broad stellar line located at 6854.32Å plus small narrow telluric line at 6854.00Å. The red line denotes a noise free spectrum while the gray line shows a spectrum with S/N=50. Middle: Same as left noise free plot but degraded to a resolution of 20,000. The magenta line marks the position of the minimum at 6854.16Å. Right: Same as middle plot but without the telluric component.

2.2 Defocus & Seeing

Another problem for high accuracy line depth determinations is that the spectral resolution is not constant but varying. This can affect the equivalent width in a predefined integration band. In figure 2.3 the integration band is such narrow that only the line core of the Hα line will contribute. During the course of the observing run its width varies. In this example the integral decreases while spectral resolution and equivalent width increase. Absorption located inside the integration band at high spectral resolution is convolved outside of it in case of lower resolution. At this place the absorption can no longer contribute to the integral. Different reasons are responsible for this effect. First, the seeing during the night is not constant but depends on meteorological conditions. An example is given in figure 2.4. It shows the total seeing derived from single star observations made by a Differential Image Motion Monitor.[3] During this night a transit observation of WASP-69b has been carried out which will be discussed in chapter 4. Unfortunately, the time series contains a large gap during the first half of the transit. Therefore, the temporal behaviour of the seeing during this period is virtually unknown. In the second half we see a sudden increase in the seeing values by about a factor of two. A comparsion with figure 2.4 reveals that this trend is also reflected by the FWHM values of telluric lines, albeit on a smaller relative scale. It is interesting to note that the peak around 0.13 days is clearly visible in both the seeing and FWHM values. Such an instrumental broadening of telluric lines is not unexpected since the spectral resolution R depends on the size of the seeing disk. Appenzeller 2013 gives $R \propto \delta^{-1}$ where δ is the size of the seeing disk. A worse seeing will therefore reduce the spectral resolution and consequently increase the width of absorption lines. Another problem is thermal expansion both of telescope parts and of the spectrograph. Temperatures are usually falling during the course of a night, especially when the sky is clear. Thermal expansion will now lead to minuscule shrinking of the telescope structure. Therefore, also the focus will slightly change its position. In modern telescopes the refocussing is normally done automatically in short timesteps. Therefore, the effect of temperature variations should be minor. The thermal expansion is not only a problem for the telescope but also for the spectrograph. Here the expansion might lead to a shift or tilt of optical components, the grating or the CCD chip. For this reason many spectrographs are put into vacuum tanks and temperature controlled rooms. However, this might not be true for low-budget spectrographs or older designs that were not built for high precision work.

2.3 RV Jitter

In a perfect world the wavelength axis of a spectrograph would be 100% correct. The nominal wavelength axis as reported by the instrument would therefore totally agree with the true positions as derived from the definition of the meter. Obviously, this is not true for any real instrument. For this reason it is

[3]This device consists of a small telescope with a diameter of a few dozen centimeters. The entrance pupil is stopped down to two small subapertures each with a diameter of a few centimeters. These are $\approx$ 20cm apart. Both subapertures form stellar images. The distance between the images corresponds to the wavefront tilt. Due to seeing the latter varies in time. As stronger the seeing is as higher this variation is. The standard deviation of the wavefront tilt then corresponds to an estimator of the seeing conditions (Sarazin and Roddier 1990). Such a device is installed at the VLT site 100m North of the UT4 telescope. A more detailed description of this instrument can be found in Chiozzi et al. 2016.

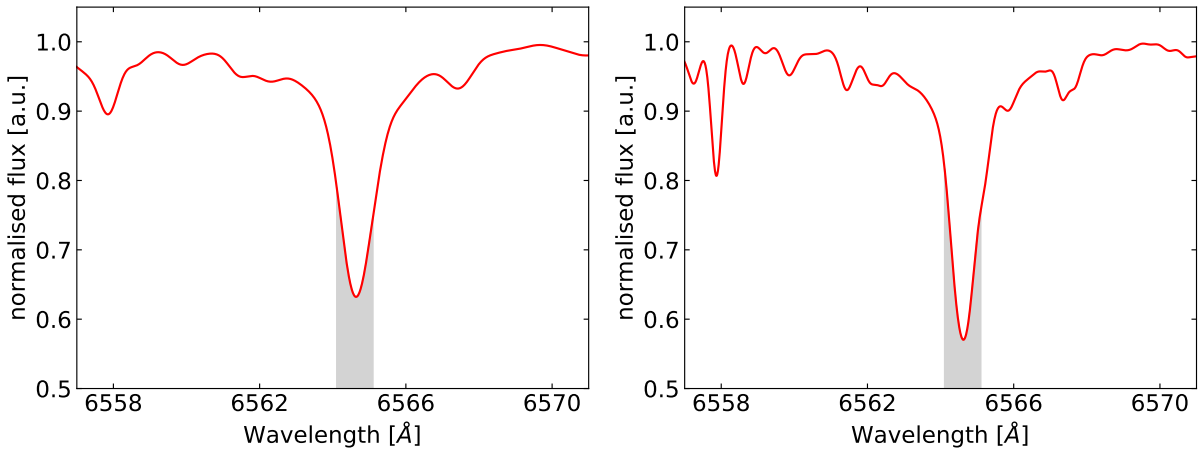

Figure 2.3: Stellar spectrum of the Hα line with R=10,000 (left) amd R=20,000 (right).

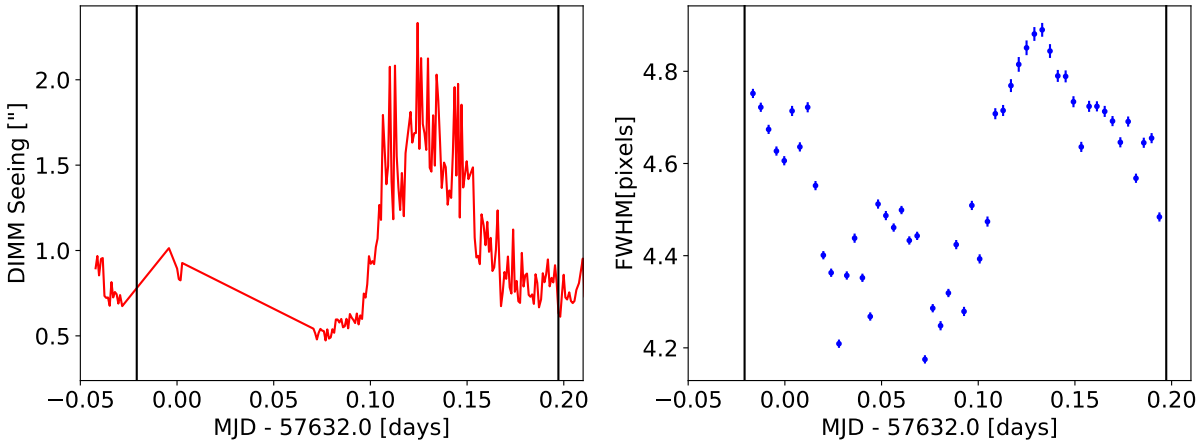

Figure 2.4: Left: Temporal evolution of seeing during night beginning August 31st 2016. Data taken from the online data base referenced in Chiozzi et al. 2016. The vertical lines mark the beginning of the first and end of last exposure. Right: FWHM of telluric lines versus time.

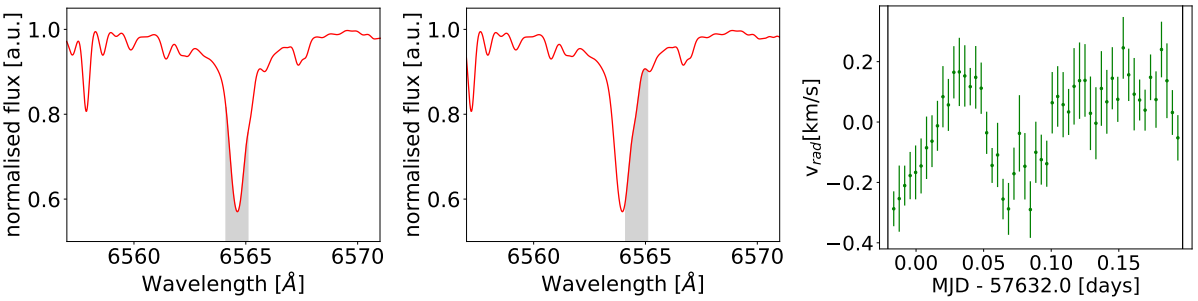

Figure 2.5: Left: PHOENIX model of a star with T =4700K and $\log(g)$ =4.5 degraded to a resolution of 20,000 without radial velocity shift. Such a model closely matches the stellar parameters of the exoplanet host star WASP-69. Middle: the same spectrum but blue shifted by 30km/s. Right: temporal evolution of the RV jitter of UVES during the observing night.

necessary to quantify the inaccuracies and to assess their impact on scientific results. The following example may illustrate this problem. In figure 2.5 I show a synthetic spectrum of WASP-69. For a description of the stellar model I refer to section 2.6 and for a listing of its stellar parameters I refer to table 5.4. Around the Hα line core an integration band with a width of 1Å is shown. The stellar spectrum I now shift by 30km/s while the integration band remains fixed. Such a situation typically occurs when the spectrograph is not RV stabilised. In this case the integral will be affected by a systematic error. The reason for this RV jitter is the image creation by a telescope. Figure 2.6 shows the combination of a telescope and a spectrograph attached to it. For the sake of simplicity a real astronomical telescope is represented by a single lens and the spectrograph is reduced to its main components collimator, disperser, camera and detector. First, the telescope produces a stellar image in the focal plane. This image is then collimated and dispersed. Finally, the camera produces for every color a particular image onto the detector. In figure 2.6 these are represented by converging red, green and blue rays. If the telescope is not ideally guided the stellar source will no longer be in the center of the field of view. Problematic in this context are deviations in dispersion direction. These will be translated into new positions of the particular images. Now the real and the nominal wavelength positions differ resulting in an RV offset as depicted by a second set of blue, green and red rays. For fibre-fed spectrographs similar effects can be observed. The decentering of the stellar image at the fibre entrance leads to a decentering at the fibre exit. Here, the RV jitter depends on the scrambling of the light. Ideally, the light distribution at the exit is completely uniform. In practise, the light distribution depends on the fibre geometry. As pointed out in Lo Curto et al. 2015 hexagonal, octagonal and square fibers produce highly uniform near-field images. In contrast, circular fibres deliver significantly worse results. In addition, also the thermal effects as discussed in section 2.2 will lead to RV jitter if they move optical components in dispersion direction. In practise, the RV jitter of modern instruments is usually much smaller. Currently, the best stellar spectrographs are stable on the 0.8m/s level (Fischer et al. 2016).

2.3.1 Magnitude of RV jitter

Until now, all investigations are based on exaggerated examples that are helpful to demonstrate the phenomena in question. Certainly, this is not very helpful when assessing their impact on scientific results. For this reason I focus on the the temporal evolution of the radial velocity drift of the UVES spectrograph during an observation of WASP-69 carried out on August 1st 2016. It is shown in the right panel of figure 2.5. This instrument is a slit spectrometer without an adaptive optics system. Further details are given in Dekker et al. 2000. The error bar represents the standard deviation of the radial velocities. While the standard deviation is below 130m/s this is not true for the drift of the mean position. It ranges from -300m/s to $+200$m/s over the course of the night.
The determination of the RV jitter works as follows: first I choose 33 telluric lines located in the vicinity of the Hα line. These are roughly equally distributed on either side. Due to their high RV stability these lines are particularly suited to assess the RV stability of the spectrograph. In Reiners et al. 2016 the authors conclude that they are stable at the 5-10m/s level. First, I fitted a Gaussian profile to every telluric line and calculated the line centroid. Then, I averaged all line centroids of a certain line over the different observations to determine the mean line position. With respect to this mean position I calculate the radial velocity. Now I average over all radial velocities of a single spectrum.

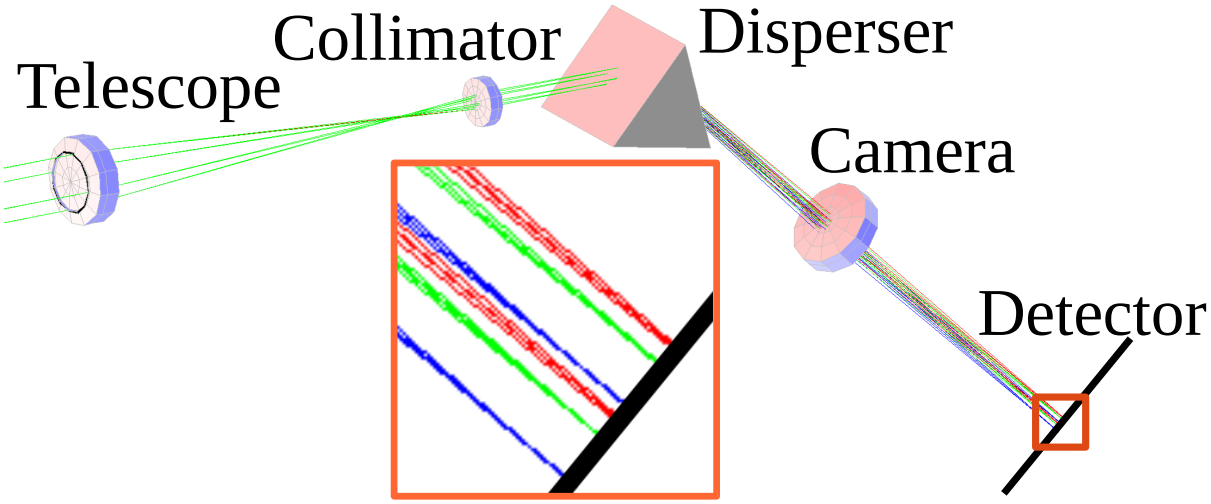

Figure 2.6: The effect of stellar source depositioning on the radial velocity. The big orange square shows a magnification of the small one.

Table 2.1: Coefficients of the wavelength distorsion scenarios, equivalent widths of the Hα and CaI lines as well as $R_{EW} :=$ EW(Hα)/EW(CaI).

scenario	a_0	a_1	a_2	EW(Hα)[mÅ]	EW(CaI)[mÅ]	R_{EW}
A	$+3.8 \cdot 10^5$	$-1.1 \cdot 10^2$	$+8.7 \cdot 10^{-3}$	310	133	2.33
B	$-4.0 \cdot 10^5$	$+1.2 \cdot 10^2$	$-9.2 \cdot 10^{-3}$	329	116	2.84
free	0	1	0	321	126	2.55

2.4 Distorsions of Wavelength Axis

The wavelength axis is usually not only affected by simple RV shifts but arbitrary distortions are possible. In this case the true wavelength λ_t as a function of the nominal wavelength λ_n as reported by the spectrograph could be expressed in the form

$$\lambda_t = \sum_{i=0}^{N} a_i \lambda_n^i \tag{2.1}$$

with coefficients a_i and degree N of the polynomial. Below I focus on three different scenarios. The first is a spectrograph free of wavelength distorsions. In this scenario the nominal wavelength axis corresponds to the true wavelength axis: $\lambda_t = \lambda_n$. Additionally, I define two scenarios with wavelength distorsions. These I label A and B. Definitions of their coefficients a_i are given in table 2.1. In all scenarios I take the identical stellar `PHOENIX` model with parameters appropriate for WASP-69. Figure 2.7 compares the different scenarios both for the Hα(left) and the CaI(right) region. The width of the Hα integration band is 1Å while it is $\pm$0.3Å around line center for the CaI line due to its smaller line width. The vacuum position of the CaI line is 6574.60Å (Kramida 2020). It should be noted that scenarios A and B are only appropriate descriptions of the wavelength axis near the regions shown in figure 2.7. An extrapolation far outside of this region serves no purpose. In practise, a description of the whole wavelength range of the spectrograph would either require a polynomial of higher order, piecewise definitions of low order polynomials in small wavelength ranges or a completely different function. Due to the distorsion the equivalent widths of both lines are systematically affected as table 2.1 points out. Depending on the coefficients the ratio between the equivalent widths may significantly be affected. While it decreases for scenario A it increases for scenario B. This choice of wavelength distorsion scenarios is certainly not representative. It may also happen that the Hα line is heavily affected by distorsions while the CaI line remains undistorted. This could happen if $\lambda_t = \lambda_n$ in the region of the Hα line but $\lambda_t \neq \lambda_n$ outside of that range. Another explanation is that the Hα line is located close to the edge of a CCD chip while the neighbouring photospheric lines are imaged by another detector. Therefore, the absence of equivalent

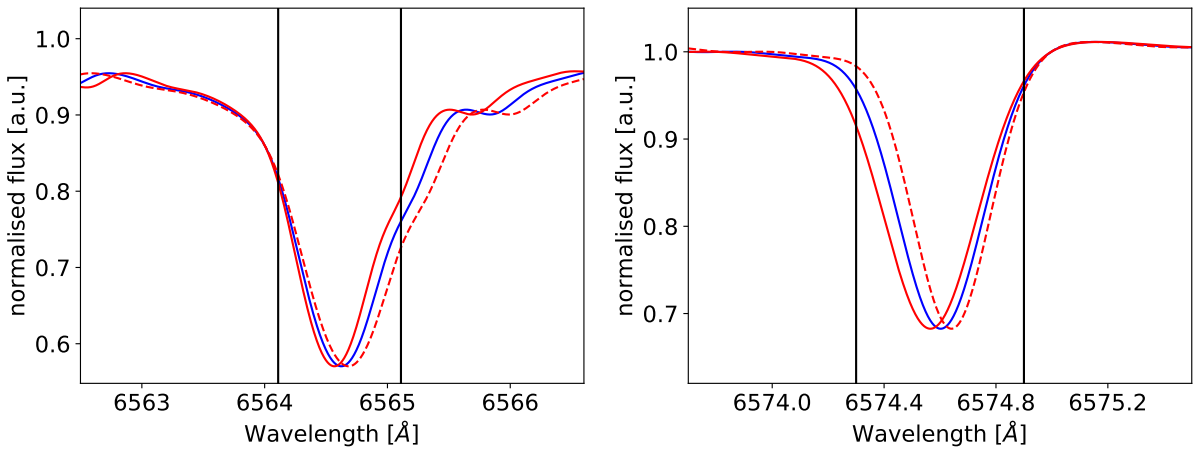

Figure 2.7: Blue: original stellar spectrum with undistorted wavelength axis. Solid red: scenario A. Dashed red: scenario B. The vertical lines denote the integration bands.

width variations in adjacent photospheric control lines are a necessary condition but not sufficient. As outlined in chapter 4 variations due to pre-transit absorption features are expected to be on a level of $\pm$10mÅ. If distorsions of the wavelength axis as described here happen during an observing night this will severely compromise the data quality. To check if this has occurred during an observing run not only the equivalent width of the line of interest should be analysed but also neighbouring photospheric lines should be included. If they are constant within the measurement errors this could imply that also the line of interest is free of major distorsions of the wavelength axis. Whenever possible, also different lines of the same species should be included. For instance, a comparison Hα vs. Hβ or CaII K vs. CaII IRT is helpful to identify instrumental artifacts. If these agree with each other it is probable that they are not of instrumental origin but rather have an astrophysical cause.

2.5 Flat-field Correction

The photon count rate per wavelength bin will not only depend on the intrinsic spectrum of the celestial source and the telluric imprint by absorption features and seeing but also on the wavelength dependent transmission function of the telescope and the spectrograph. In case of grating spectrographs the most important ingredient is the spectrograph's blaze function. Figure 2.8 shows an unreduced observation of the A0V star HR 7001. This spectrum was taken with the HEROS spectrograph on August 29th 2015. It shows the different echelle orders and its apparent flux variations from edge to center. An example of the blaze function of the spectrograph is given in figure 2.9. The vertical lines mark the wavelengths where the contribution between adjacent orders is equal. Additionally, the following optical components will contribute to the total transmission of the optical system: telescope and folding mirrors, optical fibers, lenses, prisms, grating reflectivity, quantum efficiency of solid state detectors and its pixel to pixel variations. In priciple, the transmission of each optical component can be measured in the laboratory. By multiplying all individual transmission functions the total transmission of the optical system can be calculated. In practise, the cumulation of individual small errors will introduce a significant total error. This problem can be circumvented by the application of a flat field. Light of a spectrally broad source is guided through the spectrograph in the same way as stellar photons. This ensures that calibration and science targets are similarly affected by instrumental artifacts. Typical light sources are halogen lamps. Their spectrum is dominated by blackbody radiation and thus the spectral energy distribution over a single echelle order is essentially flat. It should be noted that this procedure normalises the spectrum to the flat-field source. This can be problematic if the temperature of the calibration lamp and the stellar source are extremely different. To obtain a true flux scale the standard star method has to be used. In the framework of this approach the signal as registered by the detector is compared to a stellar spectrum. The spectral energy distribution of the standard star is known by comparison of the stellar flux to a laboratory light source. For example, Hamuy et al. 1992 present such observations. Most of these targets are of early spectral types. Therefore, the spectra are predominantly free of absorption lines which makes the flat-field correction easier. A major drawback of this method is that it can only

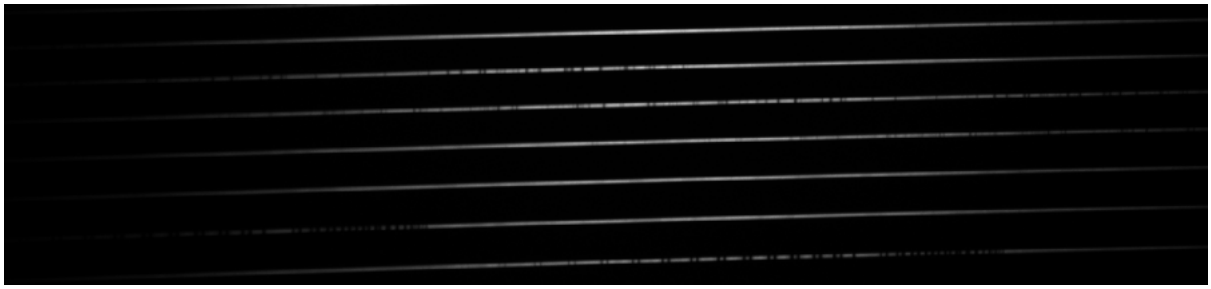

Figure 2.8: Detail of a raw CCD frame of a HR7001 observation.

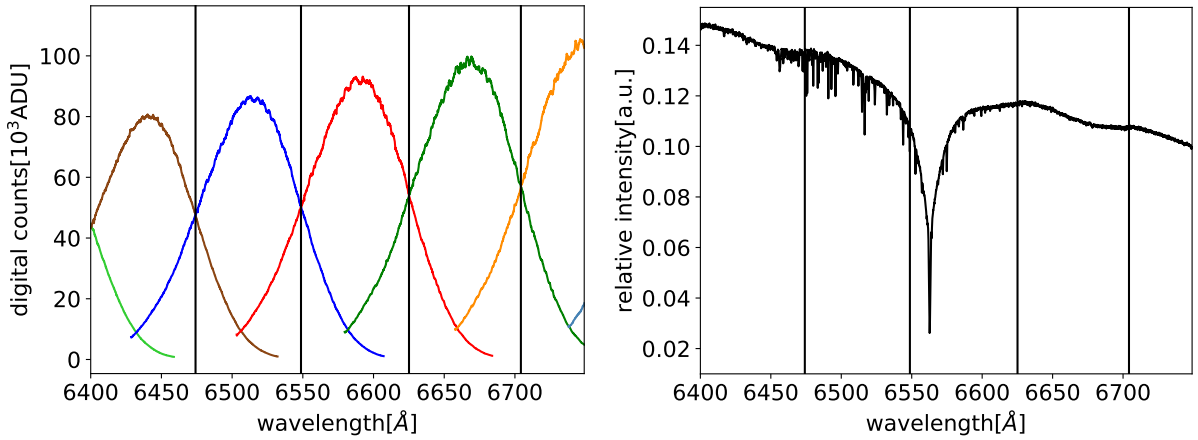

Figure 2.9: Left: blaze function of the HEROS spectrograph. The different colours represent the echelle orders. Right: Stellar spectrum of the A0V standard star HR7001 as produced by the TIGRE data reduction pipeline version 3.1.

be applied during photometric nights when the extinction depends solely on the airmass.
After flat-field correction the different echelle orders have to be merged into a single spectrum. Usually, a weighted average is used where $(S/N)^2$ is the weighting factor. This avoids the inclusion of low S/N data. Figure 2.9 shows also HR7001's merged spectrum. Blueward of the Hα line strong telluric absorption lines are visible. In contrast, these are notably shallower redward of it. Visual inspection reveals that the stellar continuum is affected by small amplitude ripples. These are on the order of 1% and coincide with the overlap regions between adjacent orders.

2.6 Putting Instrumental Artifacts Together

In the preceding sections I have summarised the most important instrumental artifacts. This section now quantifies the impact of them on the derivation of equivalent widths. In real observations all instrumental artifacts modify the stellar spectrum simultaneously in an uncontrollable way. To avoid this I take synthetic stellar spectra and introduce artifacts in a targeted way. This approach allows to disentangle individual artifacts and to assess their impact on observations individually.

Production of Synthetic Stellar Spectra

First I obtain a `PHOENIX` model from the Göttingen Spectral Library (Husser et al. 2013) that matches the stellar parameters as closely as possible. The accuracy of the models is not explicitly assessed in Husser et al. 2013. Instead, the authors compare an observed solar spectrum and a `PHOENIX` model. This reveals that several lines are missing in the model and in some cases the line depths are incorrect. It seems likely that these findings are also correct for other models of this library. This model I broad rotationally by using the `fastRotBroad` software written by Czesla et al. 2019. This algorithm is based on the equations given in Gray 2005. It assumes that the star is spherical and rotates as a rigid body. A numerical integration of the photspheric flux over the whole stellar surface is performed, taking into

account limb darkening and Doppler shifts due to the rotation. As Gray 2005 points out a linear limb darkening is fully sufficient:

$$\frac{I(\mu)}{I(1)} = 1 - u(1-\mu) \tag{2.2}$$

where $I(1)$ is the central intensity, θ is the angle between the line of sight and the outward surface normal, $\mu = \cos(\theta)$ and u is the linear limb-darkening coefficient. For u I adopt the values for the G band given in table 1 of Claret 2019. G denotes the broadband response function of GAIA's astrometric CCDs. Its passband peaks around 6730Å and it is defined in Jordi et al. 2010. The choice of the photometric passband is not critical within the scope of this work. Adopting a different passband would not alter the results significantly. Claret 2019 offers two different values for u. These have been calculated with different algorithms and I average them. Next step is a convolution with a Gaussian kernel. This represents the instrumental response function and degrades the spectral resolution. It then corresponds to the resolving power of the instrument. Finally, I multiply the stellar spectrum by a small constant and sine function and add this result to the stellar spectrum to simulate echelle ripples.

2.6.1 Quantification of Instrumental Artifacts

To explore the impact of instrumental effects I prepare a synthetic spectrum with $T_{eff} = 4700$K, $\log(g) = 4.5$ and $[M/H] = [\alpha/H] = 0.0$. These parameters roughly correspond to the exoplanet host WASP-69. Its exact parameters can be found in table 5.4. First, I produce a grid of synthetic stellar spectra as outlined before. The amplitude of the sine wave is 1% of the stellar continuum. The individual spectra differ in instrumental resolution. Next, I define the width and position of an integration band. Nominally, the integration band is centered e.g. on the Hα line. To take RV jitter into account I shift the band accordingly. Over this integration band I evaluate the equivalent width by Simpson's rule. The results are shown in figures 2.10 and 2.11. Figure 2.10 compares a lower resolution instrument having a nominal spectral resolution of R=20,000 to a higher resolution instrument with R=80,000. As the figure shows the equivalent ranges between 664 and 676 mÅ for the lower and between 662.5 and 664.5 mÅ for the higher resolution spectrograph. Because the wavelength solution of most spectrographs is correct to $\pm$1km/s I restrict the analysis to this range. While the exact spectral resolution is more important in case of lower resolution this is not true for higher resolution. Here, the radial velocity dominates the equivalent width. Interestingly, the magnitude of this effect is on the order of 6‰ at lower spectral resolution while it is below 1‰ at higher resolution. For this reason high-resolution spectrographs are in this context superior to lower resolution instruments. However, high spectral resolution in combination with high signal to noise ratio is not feasible for observations of faint targets at small telescopes. To make things even worse a sufficient temporal resolution of the transit will further limit the number of photons that can be collected during a single exposure. Another question is how spectrographs perform in case of narrow integration bands. The left graph of figure 2.11 analyses this scenario. While the maximal absolute variation of equivalent width is 6mÅ in this case the relative variation is larger in comparison to a broader integration band. Furthermore, the equivalent width is dominated by spectral resolution. This is not surprising as outlined in section 2.2. The same is also true for other stellar lines. For instance, the right plot of figure 2.11 reveals that the equivalent width as a function of RV jitter and spectral resolution looks similar to the results for Hα. It seems that the equivalent width of the TiI line can be used to correct the Hα line. For this reason I examined the integral at Hα as a function of the integral at TiI. This plot is shown in the left panel of figure 2.12. The dashed line shows a quadratic fit to this relation:

$$I_{H\alpha} = a \cdot I_{TiI}^2 + b \cdot I_{TiI} + c \tag{2.3}$$

where $a = 34.3$, $b = -10.9$ and $c = 1.5$. Next, I investigated if the conclusions drawn for WASP-69 are also valid for stars with higher temperatures. For this purpose, I produced a similar plot for a stellar model with T_{eff}=5700K. This is shown in the right panel of figure 2.12. In this case the coefficients of the quadratic fit are $a = 776$, $b = -282$ and $c = 26$. The difference in a, b and c results from the fact that an increase in stellar temperature implies a different ratio between the amplitude of the Hα and the TiI line. Similar fits can also be carried out at other stellar temperatures and will lead to essentially the same results as long as both lines are present.

2.6.2 Correction of Instrumental Effects

Theoretically, equation 2.3 can be used to infer tight relations between different stellar lines. This is valid as long as the observed spectrum is not altered. In practise, such alterations could be caused by

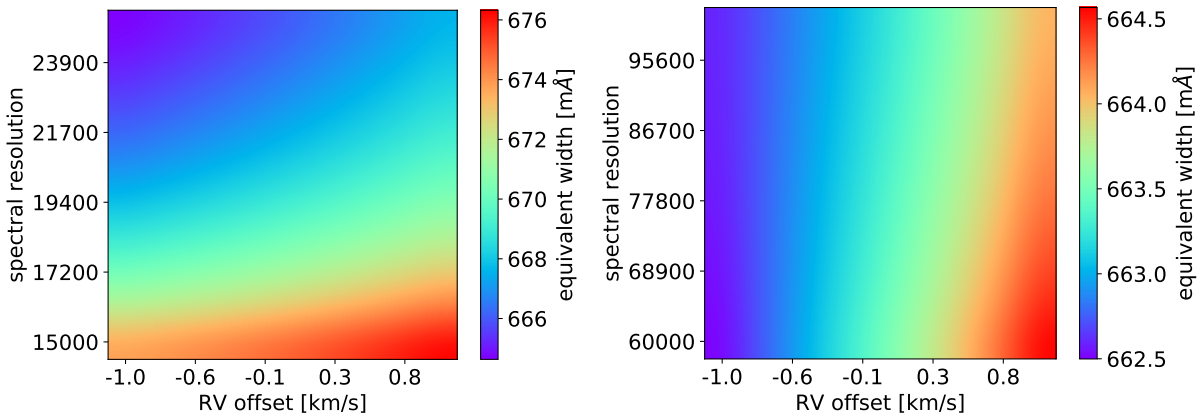

Figure 2.10: Equivalent width of Hα line within nominal integration band of 1Å as a function of RV drift and spectral resolution. While the left plot shows spectral resolutions around 20,000 the right plot shows resolutions around 80,000.

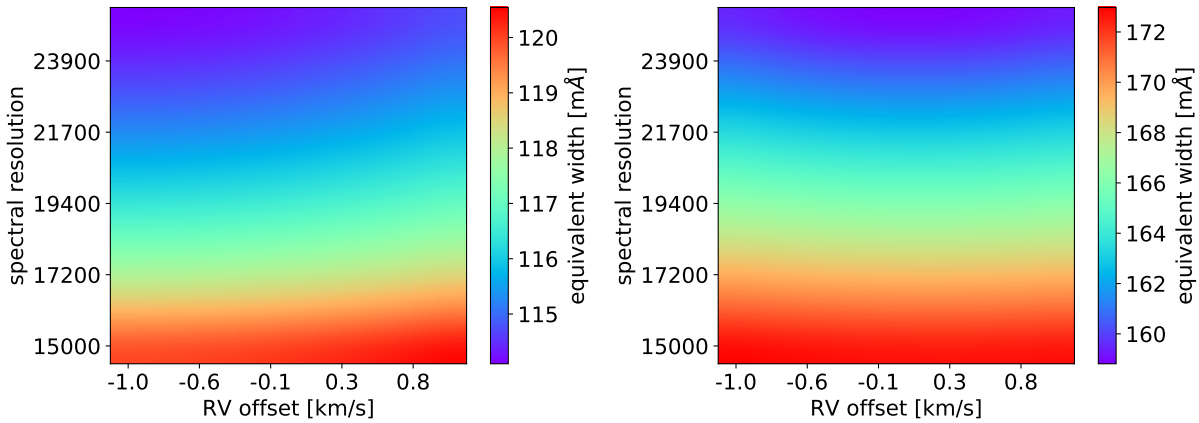

Figure 2.11: Left: Similar to figure 2.10 but the width of the integration band is now 0.2Å. Right: Similar to left figure but now the integration band is centered on a TiI line located at 6557.872Å (Kramida 2020).

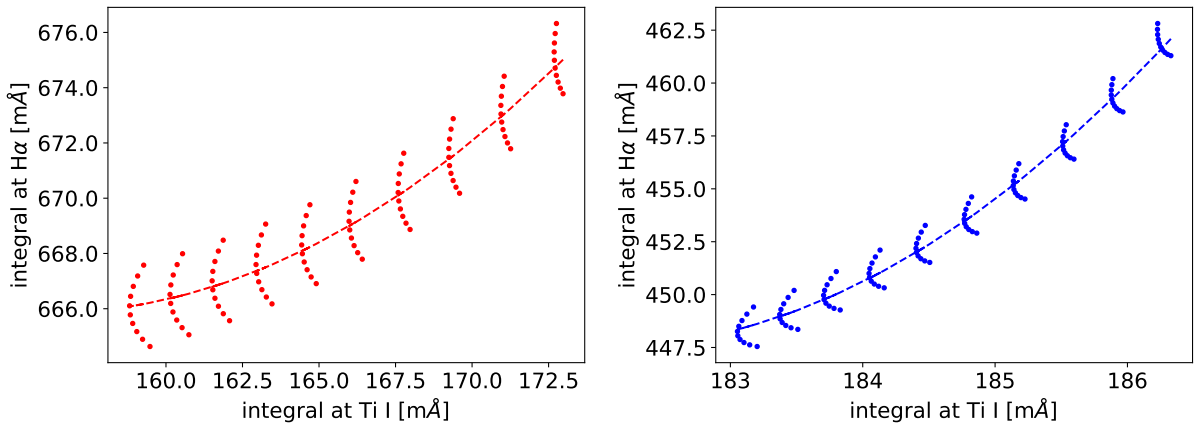

Figure 2.12: Left: Relation between $I_{H\alpha}$ and I_{TiI} for a star with T_{eff}=4700K. The dashed line denotes the best fit. Right: Same, but for star with T_{eff}=5700K.

absorption spectra of exoplanetary atmospheres. This leads to the undesirable conclusion that corrections can be applied when they are not necessary but are not possible when they are needed. Therefore, the gist of this investigation is that the magnitude of these deviations can easily be 10mÅ or more under conditions that are not pathologic.

2.7 Employed Spectrographs

This section summarizes the most important properties of the spectrographs that I used to obtain the data discussed in this thesis.

2.7.1 CARMENES

CARMENES is attached to the 3.5m telescope of the Calar Alto Observatory (southern Spain). It is located on the mountaintop of Calar Alto at an altitude of 2168m. CARMENES is a fiber-fed spectrograph with a resolution of 82,000. Its visual and near-infrared channel cover the wavelength range from 0.55 to 1.7µm. The wavelength region of the CaII H&K lines is missing. Its main mission is the discovery of extrasolar planets around M dwarfs by the radial velocity method. Since this requires a high RV accuracy great effort has been spent into it. A typical value for Luytens Star is 1.9m/s (Quirrenbach et al. 2018) for repeated observations during a single night. For this mission a minimum of 600 nights between 2015 and 2018 has been reserved. However, a small fraction of telescope time is open for other projects, for example the characterisation of planetary atmospheres of hot Jupiters. More details about the instrument can be found in Quirrenbach et al. 2014. A description of the data reduction is given in Caballero et al. 2016.

2.7.2 ESPERO

The ESPERO spectrograph is a fibre-fed echelle spectrograph connected to the 2m telescope of the Rozhen National Astronomical Observatory of Bulgaria. In contrast to CARMENES this instrument was not built for a specific scientific purpose but rather as a versatile instrument. While it is not built for high precision RV works its RV precision of $\approx$ 70m/s is still fully sufficient for the observations of pre-transit signals. The spectrograph's resolution can be adjusted between 30,000 and 45,000 by a slit. A narrower slit will lead to a higher spectral resolution at the expense of light losses. The pre-transit absorption signals are expected to be a small absorption feature caused by hydrogen. Because of the large width of the Hα line no information can be gained from high resolution observations. Therefore, I decided to use a broad slit. While its wavelength coverage nominally ranges from 3900 to 9000Å its sensitivity at short wavelengths is rather low. During data reduction it turned out that wavelength regions blueward of 4,200Å cannot be used. This is due to the fact that the S/N ratio is too low to extract scientifically useful data for targets with V=8.5 mag. An analysis of the CaII H&K activity indicators was therefore not possible and I had to switch to the CaII infrared triplet. A complete description of this instrument

is given in Bonev et al. 2017. Since there is no official data reduction pipeline for this instrument I had to do it by myself. For this task I used the `REDUCE` package described in Piskunov and Valenti 2002. This software performs the extraction of 1D spectra from 2D CCD frames and provides a wavelength solution.

2.7.3 HEROS

The HEROS spectrograph is connected to the 1.2m TIGRE telescope by an optical fiber. This telescope belongs to the La Luz observatory in central Mexico. The spectrograph consists of two channels: a blue channel ranging from 3,800Å to 5,740Å and a red channel covering 5,770Å to 8,800Å. Both channels offer a resolution of 20,000. Such a broad wavelength range is ideally suited both for the study of interstellar absorption features and for planetary transit observations. Among others the following lines are located in this range: CaII H&K, the calcium infrared triplet lines and the Balmer series from Hα to Hη. An in-depth description of the instrument and its performance can be found in Schmitt et al. 2014. The observations are reduced by a custom-written reduction pipeline which is based on the `REDUCE` package (Piskunov and Valenti 2002).

2.7.4 UVES

In contrast to the other instruments this one is located on the southern hemisphere. More precisely, it is attached to the UT2 telescope called Kueyen which is part of ESO's ensemble of 8m telescopes at Paranal observatory. Its spectral resolution is 80,000 in the blue arm and 110,000 in the red arm. The detector of the blue arm consists of a single CCD with 2048·4096 pixels while the red arm consists of two CCDs with identical format. Due to a small gap between the CCDs one spectral order is lost. Both arms can in priciple cover the wavelength region from 300 to 1100 nm. However, the exact spectral region depends on the instrument configuration (Sbordone and Ledoux 2020). Employed instrument configurations will be given in the relevant sections. UVES' RV accuracy is generally 50m/s. The extraction of 1D wavelength-calibrated spectra is done with an instrument-specific pipeline actively maintained as of January 2020 by ESO (Peron 2020).

Chapter 3

Diffuse Interstellar Bands

3.1 Importance and Origin of Interstellar Absorption

Even in the absence of all instrumental artifacts and the Earth's atmosphere spectra recorded from stellar sources are not purely of stellar origin. Instead, they contain additional features imprinted by interstellar matter. As pointed out in Redfield and Linsky 2008 the spatial distribution of interstellar matter is highly nonuniform. The interstellar medium consists of a variety of clouds. In total, Redfield and Linsky 2008 identified 15 clouds in a radius of 99pc, each with a different chemical composition and thus absorption properties. As more distant the stellar sources are as more complex the interstellar absorption pattern will become. The absorption spectra of some absorbers such as atomic Ca, Mg, Fe or Na have been studied in detail by laboratory spectroscopy. These species cause sharp absorption lines which can easily be identified in observed spectra. In addition to these sharp atomic lines many spectra of distant early-type stars show relatively broad absorption bands that cannot be found nearby counterparts. Because of their appearance in recorded spectra these features are named "Diffuse Interstellar Bands". For the majority of these absorption features the chemical composition is unknown. A notable exception are DIBs located at 9632.7 and 9577.5Å. Recently, these could be identified as a singly ionized fullerene (Campbell et al. 2015). In the wavelength range between 3900Å and 8700Å more than 400 DIBs have been identified and are listed in Hobbs et al. 2009. These were found in the spectrum of the blue supergiant HD 183143. This B7 supergiant is located at a distance of 2282^{+271}_{-221}pc (Bailer-Jones et al. 2018). Some of the bands partially overlap with stellar lines regarded later in this work. This is especially true for fast rotationg stars which therefore have highly broadened lines. Some examples are listed in table 3.1. Because DIBs generally have irregular and asymmetric profiles the determination of position, width and depth follows a special procedure given in Hobbs et al. 2009.

3.2 DIBs in the stellar Neighbourhood

Since the column density of the interstellar material generally rises with the distance of the background star it seems to be a reasonable expectation that the strengths of the diffuse interstellar bands are also higher for distant objects. In Farhang et al. 2015 the authors concluded that this is not necessarily the case. According to their results even the spectra of sources as close as 16pc are sigificantly affected by diffuse interstellar absorption. For instance, the authors found that τBoo's spectrum shows a DIB located at 5780Å. According to their analysis, it has an equivalent width of 137mÅ. For comparison, the

Table 3.1: DIBs in the vicinity of stellar lines. The first row gives the commonly used name of the nearby stellar line, the second row lists the central wavelength, the third row gives the Full-Width at Half-Maximum and the fourth row gives the equivalent width of the band. From McCall 2021.

stellar blend	CaII H	Hβ	Hβ	Hα	Hα
central wavelength[Å]	3983.60	4880.12	4881.06	6553.95	6573.04
FWHM[Å]	5.31	1.32	11.31	0.57	1.15
equivalent width[mÅ]	91.1	17.5	343.7	17.5	11.6

equivalent width of this DIB in the spectrum of the far more distant object HD 183143 is 779.3mÅ (Hobbs et al. 2009). This implies that the density of a certain component of the interstellar medium towards τBoo is by orders of magnitude higher than towards the direction of HD 183143. Such high interstellar absorption even over the distance of a dozen parsec could be problematic for the interpretation of exoplanet observations because many exoplanets are orbiting stars at distances higher than 16pc. According to the results of others, interstellar absorption can be neglected for stars closer than 200pc (Raimond et al. 2012). If the findings of Farhang et al. 2015 were true this would have consequences for spectroscopic transit observations of hot Jupiters. Possibly, abnormal strong interstellar clouds could be in the sightlines towards hot Jupiter hosts. These DIBs would introduce deformations into stellar lines, pretty much in the same way as telluric lines do and as discussed in section 2.1. While the positions of the stellar lines move due to the host star's orbital motion around its barycenter this is not true for the DIBs. Their position remain fixed. For this reason I investigated this problem early in the course of my PhD work. The results of this work are not repeated here. Instead I refer to Kohl et al. 2016. This work is part of this thesis and is reproduced in the first appendix after the bibliography. As I have shown in this work the value given in Farhang et al. 2015 seems to be compromised by the fact that the stellar spectrum is not correctly modelled. Additionally, for late-type stars the blends between stellar lines and DIBs are more pronounced than for early-type stars with few intrinsic lines. This severly complicates the analysis of spectra of cool stars. Therefore, it seems probable that also other high values of interstellar absorption in the catalogue of Farhang et al. 2015 are likewise affected. A later publication by the same group (Bailey et al. 2016) focused on the southern hemisphere. Unfortunately, this work does not discuss any concerns illustrated in Kohl et al. 2016. In this sample stars of spectral type F and later have simply been avoided. They focused on A9 to O9.5 stars.

Comparison to Stellar Models

It seems to be interesting if the above-mentioned issues could likewise have compromised their results. The procedure to create the synthetic stellar spectra has already been described in section 2.6. Here, only slight differences are applied. First, an spectral resolution of R=5500 is used. This corresponds to the instrument used by Bailey et al. 2016. Second, the spectra are interpolated to a wavelength grid of 0.55Å. All models assume an α-element enhancement $[\alpha/M] = 0.0$. For the production of the τBoo model shown in figure 3.2 I adopted the stellar parameters for this object. These are summarised in table 1 of Kohl et al. 2016. For its stellar parameters the closest `PHOENIX` model in the grid is the one with T_{eff} = 6500K, $\log(g) = 4.5$ and $[M/H] = 0.5$. For stars of spectral type F and later the depths of stellar lines are generally higher than for stars of earlier spectral types as figures 3.1 to 3.3 show. These examples show stars with effective temperatures between 4700K and 15000K. As we see in figure 3.2 the positions of both DIB coincide with the position of stellar lines in τBoo. For hotter stars the position of the DIB located at 5797Å is nearly free of stellar lines. In contrast, this is not true near 5780Å. At this position even hot stars containing few intrinsic lines show absorption, albeit it is significantly shallower. While the depth of this line is more than 10% in the spectrum of a star with T_{eff} = 4700K it decreases to less than 1% in the spectrum of a star with T_{eff} = 15000K. Because Bailey et al. 2016 give a signal-to-noise ratio of 2000 for their observations even such small features systematically limit the accuracy of their DIB measurement. The FWHM of the stellar line located near 5780Å is 0.8Å for a star with a projected rotation velocity of 20km/s. With its presumed depth of 0.8% this corresponds to an equivalent width of 6.4mÅ. The above considerations show that the problem is not limited to a few stars with peculiar spectral features but a considerable amount of the stellar sample used in Farhang et al. 2015 is in principle affected. Figures 3.2 and 3.3 show also the impact of projected stellar rotation velocity on the observed spectra. In the case of τBoo the value catalogued in Głębocki and Gnaciński 2005 of V_{rot} = 13km/s is assumed. For hotter stars the effect of rotational broadening is important. While the choice of V_{rot} = 20km/s is appropriate for cool stars this is not true for hot stars. Here, an assumption of V_{rot} = 100km/s is a reasonable value, as the catalogue of Głębocki and Gnaciński 2005 shows. For V_{rot} = 20km/s the stellar lines are significantly deeper than for V_{rot} = 100km/s. This in turn implies a pronounced rotational broadening and a flattening of stellar line cores. For deep and narrow DIBs this higher stellar rotation rate limits the systematic error introduced by stellar lines.

3.3 Impact of my Results on the Research Field

In the work of Monreal-Ibero and Lallement 2017 the authors provide the community with an improved stellar line list and stellar models in the region of DIBs located between 6100Å and 6400Å. In this region

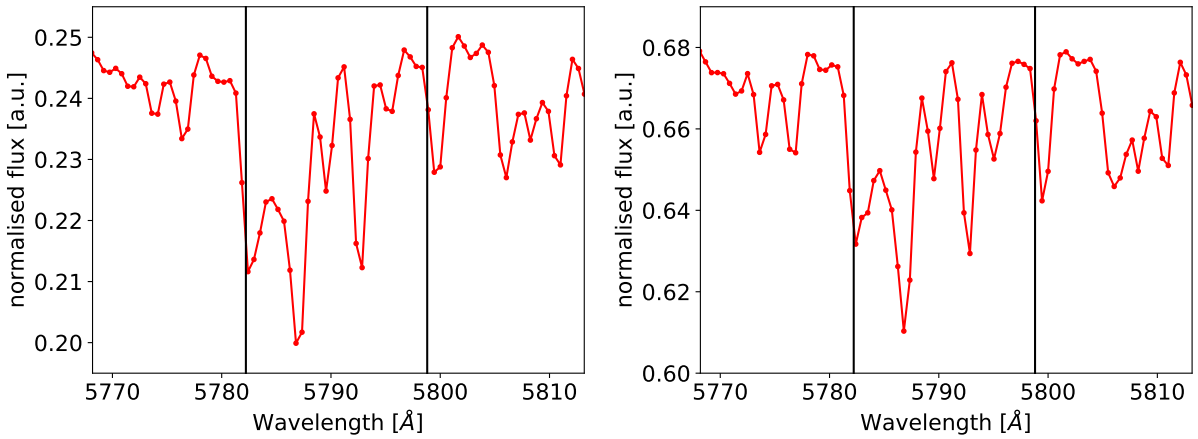

Figure 3.1: Left: stellar models for K4V(left) and G2V(right) stars with $\log(g) = 4.5$, metallicity of 0.0 and a projected rotation velocity of 20km/s. The black lines denote the positions of DIBs located at 5780.61Å and 5797.20Å.

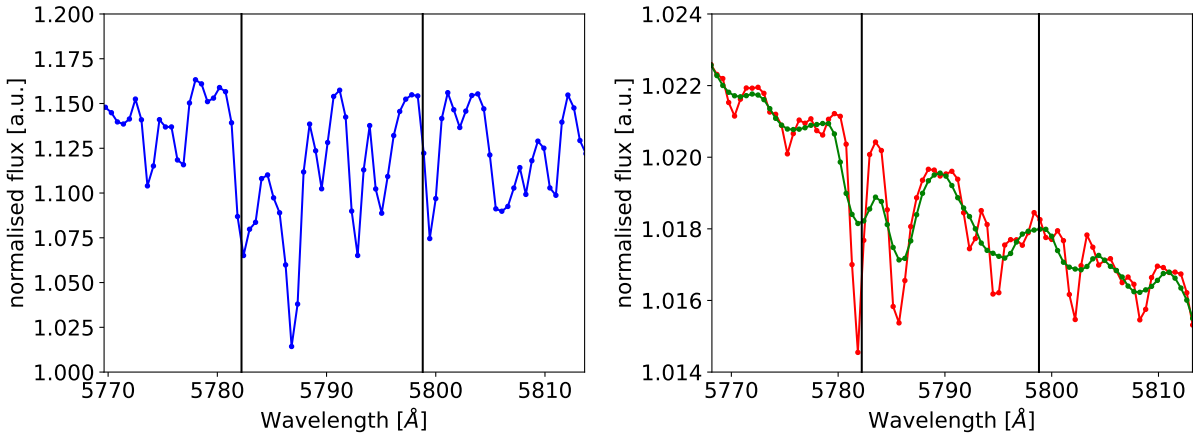

Figure 3.2: Left: stellar model for τBoo with $V_{rot} = 13$km/s. Right: stellar models for an A0V star with $\log(g) = 4.5$ and $[M/H] = 0.0$. The red line denotes the spectrum for $V_{rot} = 20$km/s while the green line stands for $V_{rot} = 100$km/s.

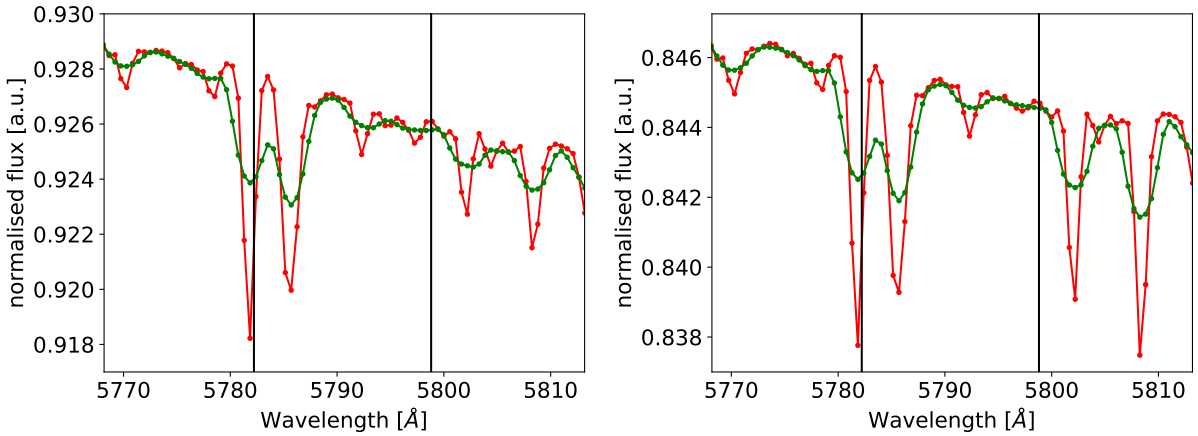

Figure 3.3: Same as figure 3.2 but for B8V(left) and B5V(right) stars with $\log(g) = 4.5$ and $[M/H] = 0.0$.

they extracted the equivalent width of four DIBs. The models discussed in this work are valid for stars with effective temperatures less than 6100K. In most cases they found that the published equivalent widths had to be revised downwards. This is a strong indication that improved stellar models can help to avoid overestimations of interstellar features. They explicitly referred to the conclusions drawn in Kohl et al. 2016.

Chapter 4

Planetary Bow Shocks

4.1 Theoretical Background

The field of explanetology has seen a radical change during the last years. Until a few years ago simply finding more and more extrasolar planets was a great sensation. It has been speculated since many centuries that our solar system is not the only planetary system in the universe. As obviously our solar system exists the universality of the laws of nature suggests that also other stars could harbour planets. Finally, in 1995 the first detection of an extrasolar planet around the main sequence star 51 Peg was confirmed by the radial velocity method (Mayor and Queloz 1995). This discovery was awarded by the Nobel Prize in Physics 2019 (Nevelius 2019). As Ciardi 2020 points out the radial velocity method dominated the first years of exoplanet detections. During this period mostly hot Jupiters have been discovered. These are planets with large diameters, high masses and small semi-major axes. The small semi-major axis implies a high planetary temperature because of intense stellar radiation impinging on the planetary surface. With the advent of space telescopes like COROT (Deleuil et al. 2018) and Kepler (Koch et al. 2010) the number of known exoplanets increased rapidly. More than a thousand exoplanets have been discovered by these space missions. In contrast to the early years, the space satellites employed the transit method. Due to the absence of atmospheric scintillation these missions could detect shallow transits implying small planetary radii and presumably smaller masses. Furthermore, the space telescopes are not interrupted by the diurnal cycle. This permits them to discover a significant fraction of planets with long orbital periods and correspondingly wide orbits. As pointed out in Fischer et al. 2016 also the RV accuracy has improved since 1995. This lowers both the mass detection limit and increases the semi-major axes that are accessible by RV surveys. Today, the orbital periods accessible by RV surveys and transit ovservations clearly overlap as shown in Ciardi 2020. However, for statistical analyses it has to be taken into account that large planets on close orbits are easier to detect than small planets on wide orbits. The list of known exoplanets can be split into different categories, depending on the size and mass of the planet as well as the semi-major axis. This work will focus on hot Jupiters.

Atmospheric Characterisation

While the census of extrasolar planets gives us an idea of the diversity of planetary systems the information about a single planet is rather limited. For this reason the current research moves away from pure determination of basic orbital and planetary parameters towards a detailed characterisation of planetary properties. In extrasolar planetary systems we find planets that are radically different from the ones in our solar system. For instance, many known exoplanets belong to the class of so-called hot Jupiters. These planets orbit their host stars at much closer orbits than even Mercury does. In contrast to the inner terrestrial planets, these have significantly larger radii and lower densities. In figure 4.1 we find such planets in the upper half of the plot. This figure shows planetary radius versus mass as listed in Henry 2020. It is conspicuous that there exist several exoplanets with masses larger than $0.5 M_{Jup}$ but radii smaller than $0.5 R_{Jup}$. A crossmatch of this subsample with Henry 2020 reveals that this density regime is probably non-existent. For example, Kepler-24 b and Kepler-28 b have no error bars given for their M_{Jup}. In some cases, e.g. Kepler-58 b, it is clearly stated that the value is an upper limit. In other cases the error bar is simply 0.0. This probably implies that also the mass value is not measured but based on theoretical considerations. To distinguish between hot and icy Jupiters, figure 4.1 gives the

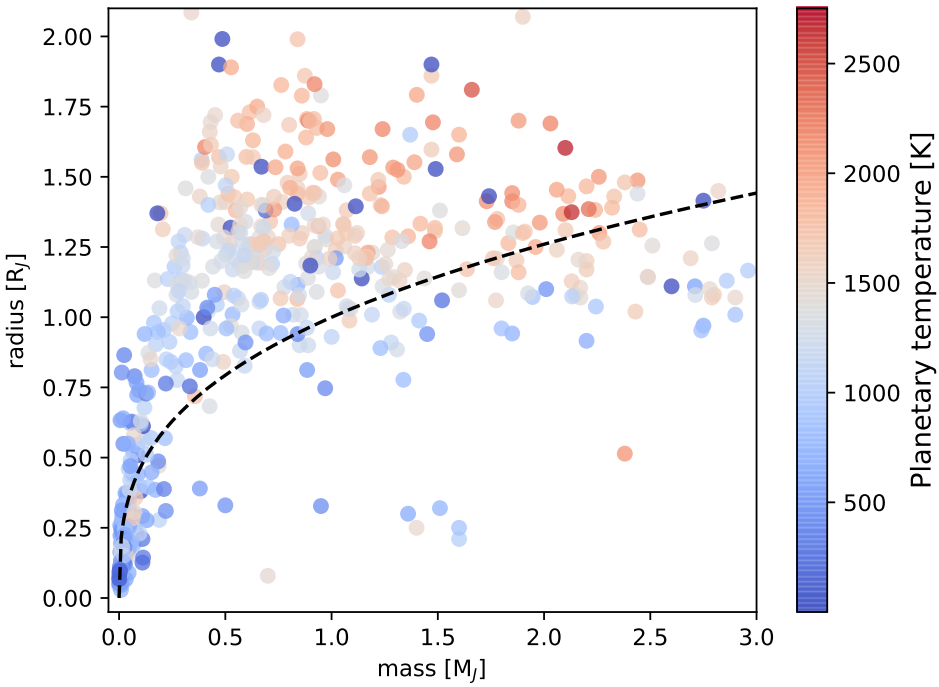

Figure 4.1: Planetary mass versus its radius. Only planets with M_{Jup} <3 are shown. The dashed line represents the density of Jupiter.

planetary temperature as a colour code. More precisely, this is the equilibrium temperature

$$T_{eq} = T_\star \sqrt{\frac{R_\star}{2a}} \sqrt[4]{1 - A_B} \tag{4.1}$$

with planetary Bond albedo $A_B = 0$. a denotes the semi-major axis. $R_\star$ and $T_\star$ refer to stellar radius and temperature. One key parameter is the presence and composition of a planet's atmosphere. Mendez 2020 lists planets as potentially habitable based on their mass, radius and equilibrium temperature. Although important to assess the habitability, information about their atmospheres is usually not available. This is not only important to speculate about life but the possible absence of an atmosphere has far-reaching implications for the effects of stellar winds on planetary atmospheres. As pointed out in Vidotto 2018 terrestrial planets in the habitable zone around M stars without magnetic fields will lose a significant fraction of their atmospheres. For such planets atmospheric observations are not yet feasible with current technology. This is because an earth-size planet covers only a tiny fraction of its host star during transit. Let d_p be the planet's diameter and d_s the host star's diameter. For late M dwarfs Mamajek 2020 gives $d_s \approx 0.1 R_\odot$. For the earth Klioner 2020 gives $d_p \approx 0.009 R_\odot$. This yields $d_p^2/d_s^2 \approx 0.008$. For hot Jupiters with $d_p \approx 0.1 R_\odot$ orbiting solar-like stars d_p^2/d_s^2 is identical but their atmospheres can be puffed up as shown in Yan and Henning 2018 for KELT-9 b. Sing et al. 2016 give an overview of detections of planetary atmospheres. The authors summarize that various atoms and molecules, e.g. Na, K and water have been detected in their atmospheres. Besides these species the detection of hydrogen by Lyα transit spectroscopy has been claimed in a number of exoplanets. One example is GJ 436 b (Ehrenreich et al. 2015). This planet is not only surrounded by an extended atmosphere but the transit is also followed by a comet-like cloud. Another example is HD 189733 b. This planet will discussed in section 4.2. In principle, the detection could also be performed in the Hα line but as will be shown in section 4.3.1 this observation can potentially be contaminated by stellar activity.

4.1.1 Interactions between Planets and Host Stars

Due to the close orbits of hot Jupiters strong interactions between host stars and planets can be expected. One possibility is that hot Jupiters with low surface gravity lose a significant fraction of their upper hydrogen atmosphere by evaporation due to the strong stellar irradiation (Kubyshkina et al. 2018). This

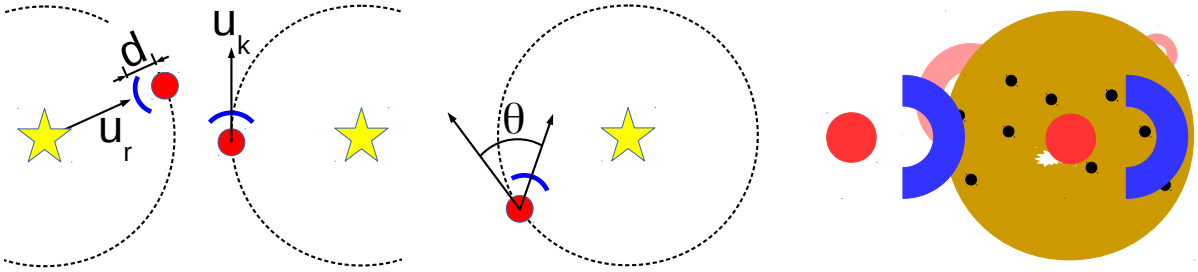

Figure 4.2: From left to right: Topview of the dayside-shock, the ahead-shock and the intermediate case. The red dot gives the location of the hot Jupiter on its orbit and the blue arc stands for the bow shock. Side view of the bow shock as seen by the observer. Black dots represent starspots, the serrate symbol a flare and the red arcs stellar prominences.

material is subsequently accreted by the host star. For optically thick accretion streams this process can be detected by absorption spectroscopy. In the case of high stellar irradiance, high surface gravity and large distance to the host star the irradiance leads to a bloated atmosphere. At small distances to the host star the size of the planetary atmosphere is larger than its Roche lobe and thus the planet will lose its atmosphere by overflow. This process could be detected by absorption spectroscopy, too.

Formation of Planetary Bow Shocks

A completely different scenario is the formation of pre-transit absorption features by supersonic interaction between the planetary magnetosphere and the stellar wind (Vidotto et al. 2010). At the interaction zone the speed of the material abruptly drops from supersonic to subsonic velocity, is heated up and compressed. This leads to the formation of a bow shock. If the heating process is sufficiently efficient the temperature will be high enough to excite a significant fraction of hydrogen into the N=2 state. Now, the hydrogen cloud can be observed both in the Lyman and in the Balmer series. The Balmer series is advantageous due to the fact that this series is not absorbed by cold interstellar hydrogen. Additionally, the Balmer lines can be observed with ground based telescopes.
The distance d between planet and shock nose depends on the balance between stellar wind pressure, gas pressure of the upper planetary atmosphere and magnetic pressure caused by stellar wind and planetary magnetic field. As will be discussed in chapter 6 this pressure balance allows to estimate the planetary magnetic field strength. Depending on the direction of the relative velocity between stellar wind and planet a dayside-shock, an ahead-shock or an intermediate shock is formed. Examples are shown in figure 4.2. The dayside-shock is produced when the radial component of the stellar wind velocity u_r is larger than the sound speed c_s. In this case the energetic particles coming from the star hit the upper layers of the planetary atmosphere. The ahead-shock is produced when the relative azimuthal velocity between the planetary orbital motion u_k and the stellar particles is supersonic. In reality, both effects will contribute to the shock formation. Therefore, θ, the angle between the direction of planetary motion and the location of the bow shock as seen from the planet's center, is given by

$$\theta = \arctan\left(\frac{u_r}{|u_k - u_\phi|}\right) \tag{4.2}$$

where u_ϕ is the azimuthal component of the stellar wind velocity. For a transit observer projection effects have to be taken into account. He cannot determine the true distance d between planet and bow shock as well as θ but merely $d\cos(\theta)$. The passage of the bow shock is illustrated by the side view also shown in figure 4.2. This figure also includes several examples of unpredictable stellar surface features that may compromise the analysis. Before the transit begins, neither planet nor bow shock are eclipsing the star. First, the bow shock alone eclipses the star. Later, both planet and bow shock eclipse the star. At the end of the transit the bow shock first leaves the stellar disk and the planet follows. An example light curve is shown in figure 4.3. This plot shows temporally resolved absorption depths of the first three Balmer lines. These data points are overplotted with a model that includes both the planetary transit and the bow shock. This model shows that the strongest absorption can be expected in Hα while the weakest absorption is seen in Hγ. For this reason I mainly focus on the Hα line. A slight drawback in the wavelength region around 6563Å is the presence of small telluric lines. These are not present at Hβ and any Balmer lines blueward of it. Because these telluric lines can be largely corrected I do not expect

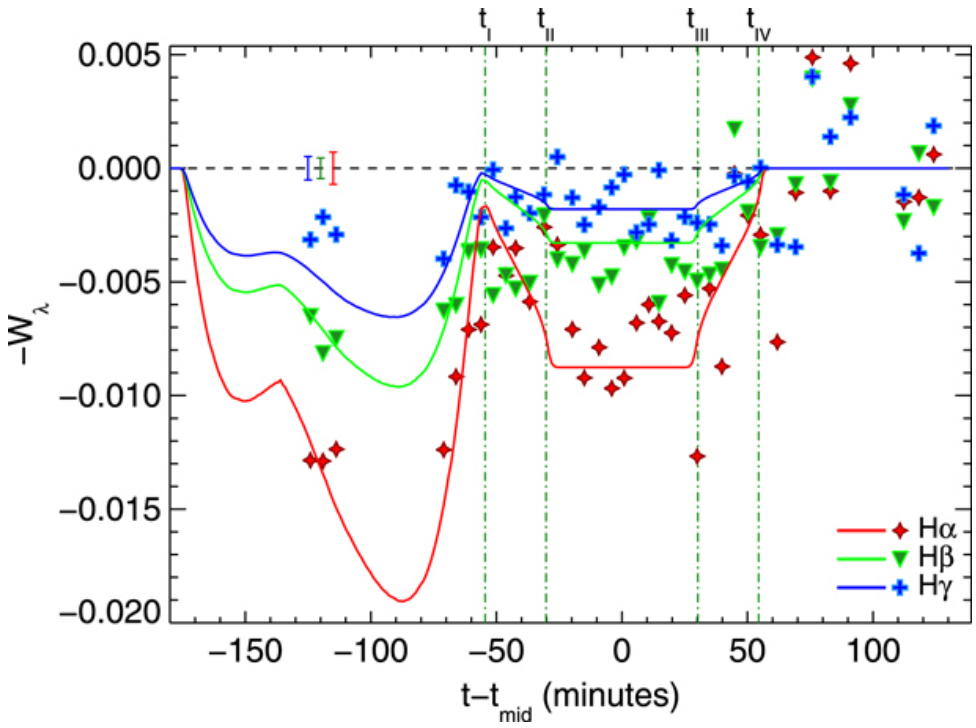

Figure 4.3: Transit of HD 189733 b observed on July 4th 2013 using HiRES on Keck I. The vertical green dash-dotted lines mark first through fourth contact. The solid lines denote the models for Hα, Hβ and Hγ absorption. From Cauley et al. 2015.

a major impact on scientific results.
In Cauley et al. 2015 the authors conclude that the projected distance between both components is $12.75R_P$. For this reason the transits of planet and bow shock are completely separated, that is the distance between them is larger than the host star's radius and we see two transit events.

4.2 Selection Criteria for the planetary sample

As of January 25th 2021 exoplanet.eu lists 4,404 extrasolar planets in total. However, the vast majority of planets is not suitable for atmospheric characterisation. The following paragraph lists the selection criteria for the planetary sample. As outlined in the preceding section the planetary absorption manifests only as a tiny variation in the equivalent width of the Hα line. For this reason a transiting planet is mandatory. Furthermore, high signal to noise spectra are required. To avoid phase smear of the pre-transit signal the exposure time should be limited to 15 minutes. Because both requirements contradict to some extent a high apparent brightness of the planet host star is required. This criterion drastically reduces the number of candidates. The vast majority of transiting planets listed in Henry 2020 is fainter than 12 in V band. Furthermore, the planetary mass must be high enough such that a hydrogen atmosphere will not boil-off during a few million years. As Fossati et al. 2017 point out this is in general only true for planets with masses greater than 10 $M_\oplus$. Last but not least the planetary density should be equal or smaller than Jupiter's density. Planets with higher density are presumably rocky. Since plantary densities cannot be directly measured I infer them from masses and radii. While the radius can easily be determined by transit depth mass values are often completely missing or are rather uncertain. The planetary temperature is also an important constraint for the choice of the target. Only for planets with high temperature I expect a considerable evaporation of the upper layers of the planetary atmosphere and therefore a sufficient feeding of the accretion stream. A self-evident assumption is that all planets with temperatures around 1000K or above are suitable targets. As pointed out by Salz et al. 2016a an important ingredient for atmospheric escape is the X-ray and extreme UV irradiance received by the planet. Monsch et al. 2019 give a list of X-ray luminosities of planet-hosting stars. Due to the fact that X-ray sources either have to be rather close to the solar system or have to be extremely bright the X-ray luminosity of only a fraction of planet hosts is known. This severely limits a reliable derivation of

planetary mass loss rates. With the advent of the eRosita mission this situation is expected to improve (Robrade 2016). Later, Kubyshkina et al. 2018 studied planetary mass loss without the assumption of energy-limited escape for planets around stars with effective temperatures below ≈8250K. Although the authors examined a variety of planets with a broad range of masses, radii, temperatures and extreme ultraviolet fluxes the mass losses were found to be between 10^9 and 10^{10}gs^{-1}. As shown by Salz et al. 2016b this mass loss rate will not evaporate the planet within the current age of the universe.[1] For planets around hotter stars García Muñoz and Schneider 2019 conclude that planets with masses below $\approx 1.5 M_{Jup}$ can be prone to atmospheric escape within 10 Gyr for very close (a <0.025 AU) orbits. A comparsion between between Kubyshkina et al. 2018, García Muñoz and Schneider 2019 and Salz et al. 2016a shows different values of the models but also points out that the orders of magnitude roughly agree. Additionally, for some planets Kubyshkina et al. 2018 compare these values to observations. Because of large observational error bars all models have to be regarded as correct. To pick the most promising cadidates out of the list of known exoplanets one strategy is to search for planets where Hα or Lyα absorption was already detected.

HD 189733 b

This object is one of the best studied extrasolar planets. Henry 2020 lists an enormous long list of publications that deal with this planet. For this object Kubyshkina et al. 2018 found that the expected mass loss rate is not exeptionally high but quite close to the median. Lecavelier des Etangs et al. 2012 compare in-transit and out of transit Lyα spectra for observations carried out in April 2010 and September 2011. During the former observing run the spectra before and during transit are equal within their respective error bars. In contrast, the latter observing runs showed that the absorption during transit is substantially stronger. The authors conclude that this difference is caused by the atmospheric hydrogen. Because an X-ray flare has been observed eight hours before the 2011 observation the authors conclude that interactions between the exoplanets atmosphere and stellar activity probably exist. This flare could have triggered the planetary atmospheric escape. Not only the Lyα observations favor the presence of an extended atmosphere but also X-ray observations do. In Poppenhaeger et al. 2013 the authors examined transit observations at X-ray wavelength. They concluded that the temporal variation of the light curves is caused by metals in the upper atmospheric layers, although alternative explanations cannot be fully ruled out. Also Jensen et al. 2012, Cauley et al. 2015 and Cauley et al. 2016 have claimed detections of planetary Hα absorption. Figure 4.3 shows the transit and the putative bow shock of HD 189733 b. It can be seen that both features are deepest and therefore most easily observable in the Hα line. While the data points are as deep as 13mÅ the model suggests that the bow shock is as deep as 19mÅ. This planetary interpretation is not undisputed (Barnes et al. 2016). If existent, such a deep bow shock can easily be observed even with a meter-class telescope. Therefore I include this object into my sample. From scientific point of view this object satisfies all criteria, but practical requirements compromise transit observations. The reason is that this target can be best observed from spring to fall. Unfortunately, at the TIGRE telescope site in Mexico this corresponds to the rainy season. Uninterruped observations of the bow shock plus a transit with a length of 114 minutes are unlike to be carried out during a single night. To make things worse the total number of observing windows that allow for these observations in 2017 was limited to 8. For this reason a different observing strategy was applied. Instead of a continous observation of a single transit 2-3 observations per night were carried out. These were randomly distributed over planetary phase. After the observing season the transit is assembled from the individual exposures.

WASP-69 b

This object has mainly been chosen because of its high X-ray brightness (Anderson et al. 2014) and the fact that transit observations with both high S/N and high spectral resolution were already available at the start of this project. The former promises a detectable mass loss. The latter reduces the uncertainities of not being awarded with observing time, bad weather or technical problems during observation.

WASP-131 b

In contrast to WASP-69 b this host star was not detected in X-rays. Therefore, the X-ray brightness is highly uncertain. Whatever the X-ray flux received by WASP-131 b is it can still host a detectable bow

[1] Tanabashi et al. 2018 give 13.80 ± 0.04 Gyr.

shock that is independent of the mass loss rate. As in the case of WASP-69 b the big advantage was again the availability of a transit observation.

KELT-7 b

Literature about this object is sparse (Henry 2020). Information is only available about planetary radius, its mass and semi-major axis. Due to the latter an estimate of the planetary temperature is feasible. In contrast, detailed spectroscopic observations neither in Lyα nor in Hα are available. Likewise, information about stellar activity or X-ray brightness are unavailable. I included this object mainly because of its high brightness and the fact that newly discovered planets offer ample possibilities to contribute to their understanding.

KELT-20 b

At the beginnig of this research project the same was also true for this object. Additionally, a CARMENES transit observation was already available. As of March 2021 the number of publications dealing with this object has considerably increased due to the fact that this is one of the brightest known exoplanet hosts.

4.2.1 Potential future candidates

The field of exoplanet research developes with high pace. For instance, as of June 9th 2020 Henry 2020 lists far more than 100 extrasolar planets that have been discovered in 2019. For this reason a definitive sample of targets could not be defined at the beginning of this research project and probably this will never be possible. One potential hot Jupiter for future observations is HD 1397b (Brahm et al. 2019). The visual brightness of its host star is 7.8. In contrast to the targets regarded in this work it orbits an evolved star. Due to its position in the southern sky and its brightness detailed follow-up observations can be expected e.g. from the 8m ESO telescopes.

4.3 Stellar Activity

4.3.1 Observational challenges

Observations in the Balmer lines are are not only sensitive to planetary absorption features but also an unintentional probe of stellar activity. In this section I summarize the most important activity features that are relevant for the interpretation of planetary transit observations. For instance, Livingston et al. 2007 demonstrate that the depth of the Hα line clearly follows the solar cycles. On its own, this would not affect transit observations lasting a few hours. Nevertheless, during epochs of high activity the sun's surface is rather inhomogeneous. This is shown in solar full disk images taken at Kanzelhöhe solar observatory (figure 4.4). This observatory is located in southern Austria near the town of Villach quite close to the Slovenian Austrian border. The main instrument comprises multiple refractors on a single parallactic mounting (Pötzi 2020a). Each telescope is equipped with a filter and a CCD camera. The filters are targeted to the CaII K line, the white light continuum and the Hα line. This setup permits simultaneous observations in all bands. In the CaII K line image the most prominent features are bright regions on the solar surface. Most of them are accompanied by small dark spots. These spots we find also in the white light image. In contrast, the bright regions of the Hα and CaII K images resemble each other. We find bright faculae and plages as well as elongated dark mottles. The original FITS file[2] also shows spicules at the solar limb and far-ranging coronal loops. These are hard to spot in the present printed reproduction. An additional problem is the line-of-sight velocity of ejected material of about 5km/s. This implies a blueshifted spectrum coming from a part of the solar disk. In contrast, the line-of-sight velocity of the quiet solar surface is close to zero. The spectrum of the active region together with the spectrum of the quiet sun forms the total spectrum. As figure 4.4 shows active regions are small compared to the total solar surface. Therefore, the contribution of the active regions's spectrum will be a pertubation. It manifests as a small distorsion and broadening of the Hα line and a jitter in radial velocity of the line centroid. Stellar activity not only affects the outer solar layers but also its photosphere. Particularly important are sunspots. Large spots can have a diameter of more than 10,000km and temperatures as low as 3,700K. An inspection of a stellar model spectrum from the Göttingen Spectral Library (Husser et al. 2013) reveals that the Hα absorption line is virtually gone at T=3,700K. Large spots will therefore

[2] ftp://ftp.kso.ac.at/Ha4M/2014/20140227/processed/kanz_halph_fi_20140227_102904.fts.gz

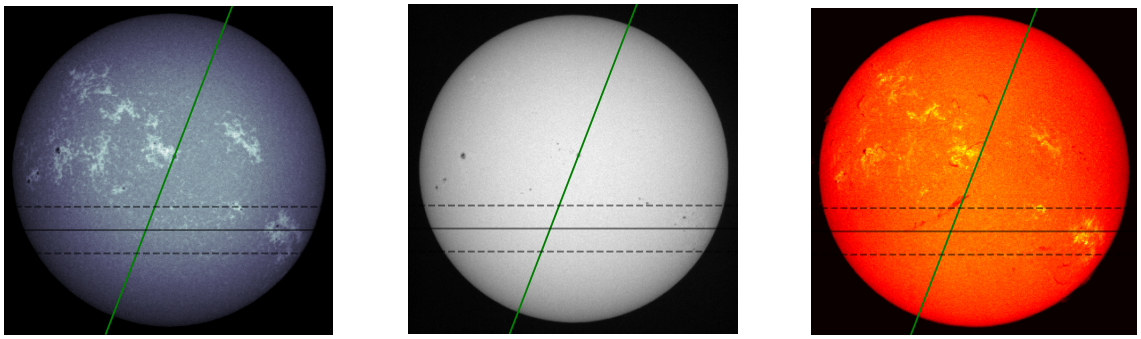

Figure 4.4: Full disk solar images observed February 27th 2014 around 10h29m UTC at Kanzelhöhe solar observatory. The solid black line denotes the path of the planetary center while the dashed lines show the planet's size and the green line denotes the projected solar rotation axis. In all images the solar North pole is up and West is to the right. Left: CaII K line. Central wavelength is 3933.70Å and FWHM is 2.4Å. Middle: White light. Right: Hα line. The filter is centered at 6563Å and its FWHM is 0.7Å (Otruba and Pötzi 2003).

cause a tiny decrease of the line depth. Like chromospheric features also the spots are affected by line-of-sight motions of stellar material by a few km/s. As outlined before, this will imprint an additional distortion on the Hα signal. The planet moves over the stellar disk during the course of the transit. Therefore, it will block different parts of the disk during the transit. This implies a temporal variability of the stellar spectrum and hence a systematic error for the determination of the equivalent width of stellar lines. Even the total absence of stellar activity and a completely homogeneous disk do not mean a constant equivalent width as will be discussed in section 4.4.
The images shown in figure 4.4 were taken during the maximum of the 24th solar cycle. Selecting images showing the sun during the maximum of an activity cycle seems to be an unreasonable choice but it should be kept in mind that the 24th cycle was relatively weak. For instance, the 19th cycle was much stronger (Clette 2020). Between 1957 and 1959 the yearly mean sunspot numbers were even higher than the international sunspot number on February 27th 2014. Therefore, activity patterns as observed on February 27th 2014 were presumably quite common during these years. Also other exoplanet hosts might show similar activity levels today. Because CCD observations were not possible during the late fifties I chose to take data from the 24th cycle. Photographic material is already available for this time. Unfortunately, the conversion from photographic density to irradiance is cumbersome or even impossible. It heavily depends on the details of the development process of the photographic material (Koch 1995). First of all, the photographic density D is not a linear function of the incident photons p. For low light levels D is constant. For intermediate exposure it is given by

$$\Delta D = \gamma \Delta \log(p) \tag{4.3}$$

where γ depends on the details of the development process. For instance, development time, temperature during the development process and the exact chemical composition of the developer can affect γ. For high illumination D saturates. Such details are often not available and thus systematic errors would be unavoidable. In contrast, CCD counts are proportional to the number of incident photons as long as the detector is not saturated (Howell 2006).

For stars other than the sun the active regions on the stellar surface cannot be spatially resolved. Instead, observed spectra and light curves are superpositions of contributions coming from different parts of the stellar disk. During transit the planet eclipses a tiny fraction of the surface. This problem has been adressed in the past by different working groups. For instance Cauley et al. 2017a and Cauley et al. 2018 take a CaII K solar image. First, they identify faculae as regions with normalised flux $\geqslant$1.2 and spots as regions with normalised flux $\leqslant$0.8. The total solar spectrum is now given by

$$S_{tot} = f_{faculae} S_{faculae} + f_{inactive} S_{inactive} + f_{spot} S_{spot} \tag{4.4}$$

where S_i is the spectrum of a certain component. f_i is the corresponding fraction of the solar disk excluding the planet's occultation. Rackham et al. 2019 used a similar approach. The advantage of this method is that models can be created not only for the sun but also for a variety of host stars.

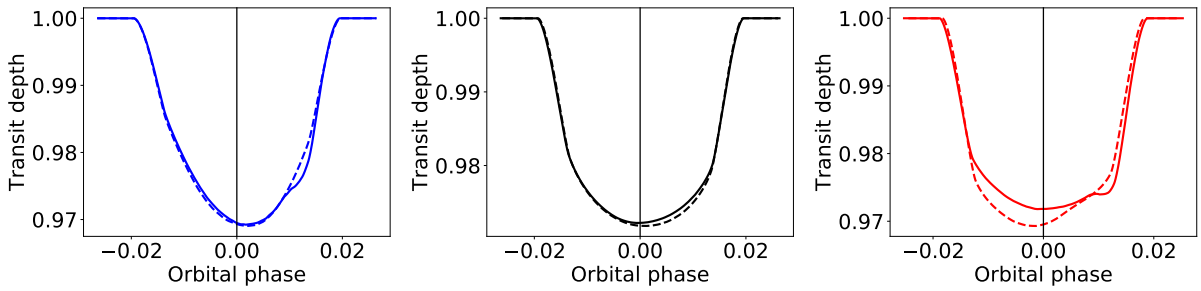

Figure 4.5: Synthetic transit light curves a distant observer would record if there was a close-in large planet in the solar system. Bandpasses are identical to figure 4.4. The solid lines are light curves during high stellar activity while dashed lines result from epochs of low activity.

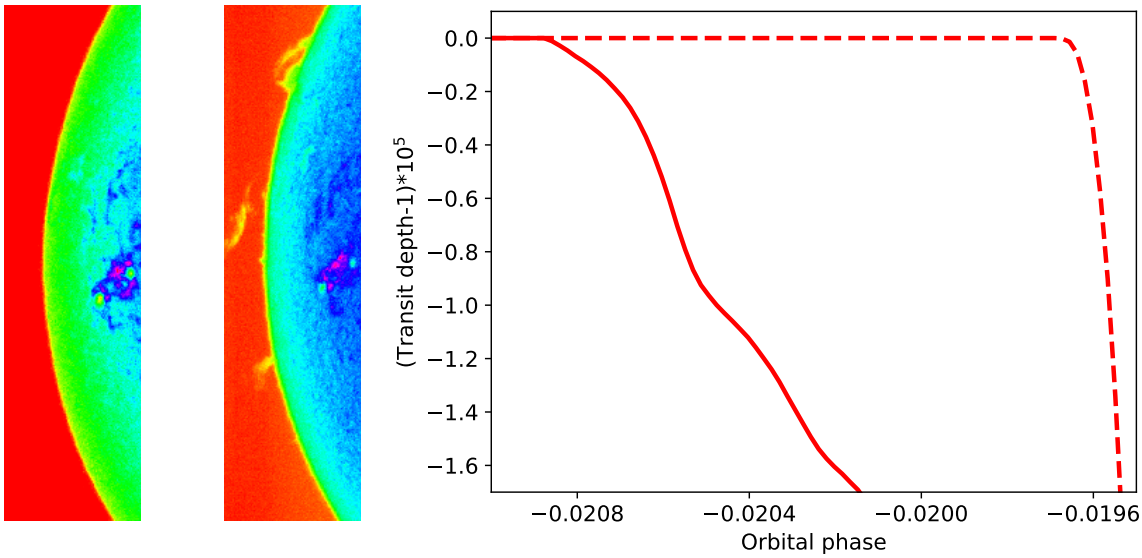

Figure 4.6: Left and middle: same CaII K and Hα images as shown in figure 4.4 but zoomed-in into the Western solar limb. False-color coding is used to enhance features located outside of the solar disk. Right: Hα transit light curve similar to figure 4.5 but for an inclination of 90° and zoomed-in into the pre-transit phase close to the instant of the first contact. Note the stretching of the y axis.

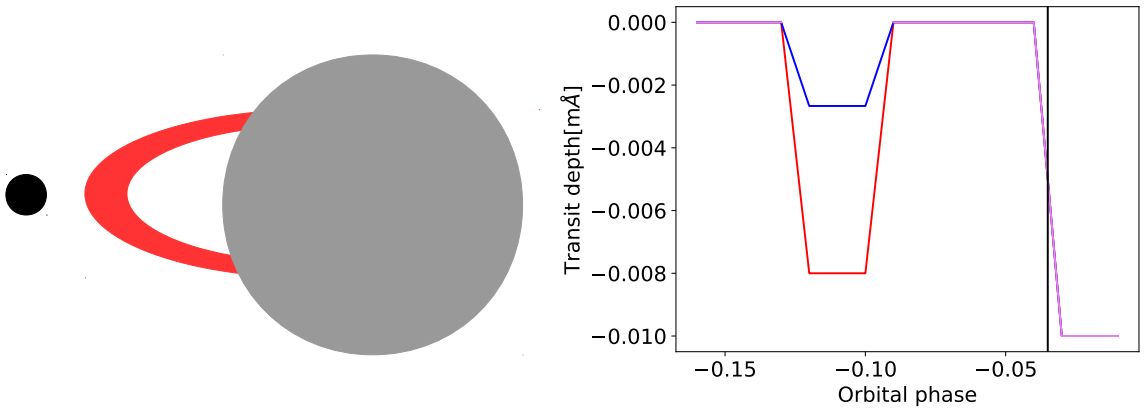

Figure 4.7: Left: star with a huge prominence on the western limb and a tansiting hot Jupiter. In this scenario the planet transits from the West to the East. Right: Transmission light curves in CaII K (blue) and Hα (red). Overlapping sections are marked by violet colour.

The drawback is that a bunch of assumptions contributes to these models. Among others these are temperature difference between active regions[3] and photosphere, active region covering fraction, size and position of active regions. All these quantifies are poorly known for stars other than the sun. In combination with the effects of a planetary atmosphere the derivation of a stellar surface model from transit observations is not trivial. Here I use a different approach that works as follows: to assess the relevance of stellar features on transit light curves I study numerical transits derived from solar images. The solar images are taken with narrowband filters centered on chromospherically active lines. Outside these lines the spectrum is almost unaffected by stellar activity. Therefore a comparison between chromospherically active line and adjacent continuum can be replaced by a brightness determination in a narrow spectral region if the image is sufficiently flat-fielded. A computationally efficient algorithm for the evaluation of synthetic transit light curves has been developed by my colleague Holger Müller (Müller 2015) and works as follows: let $S(x,y)$ and $P(x,y)$ be the two-dimensional brightness distribution of the stellar disk and the planet's opacity respectively. The transit t_x can now be described as a two-dimensional convolution:

$$t_x = S(x,y) * P(x,y) = \int_{-\infty}^{\infty}\int_{-\infty}^{\infty} S(x,y)\cdot P(x-\xi, y-\phi)\, d\xi d\phi \tag{4.5}$$

This equation cannot be evaluated computationally efficiently. A fast Fourier transform of P and S to $\tilde{P}$ and $\tilde{S}$ plus the convolution theorem now allows us to rewrite equation 4.5 as

$$\tilde{t_x} = \tilde{S}\cdot\tilde{P} \tag{4.6}$$

where $\tilde{t_x}$ is the fast Fourier transform of t_x. This decreases the computational demand from N^4 additions in equation 4.5 to $N^2 \log_2 N^2$ additions in equation 4.6. To obtain useful results with this algorithm the solar image must be complete. Additionally, the solar diameter must be larger than 750 pixels to obtain a photometric precision equal to the Kepler space telescope. Furthermore, the planet's orbit must be larger than $4R_\odot$, i.e. 0.02AU. This algorithm has two important advantages. First, the stellar surface brightness distribution can be any function. Second, the planet's shape and opacity can be arbitrary. For instance, the planet could have an atmosphere, rings or being ellipsoidal.

I study the transit of an imaginary spherical planet without an atmosphere in the solar system. In this scenario a fictitious planet as big as a hot Jupiter crosses the solar disk. Its orbital parameters and its transit depth are identical to HD 189733 b. To achieve an identical transit depth I scaled the planetary radius by $R_\odot/R_\star$. From these planetary parameters in combination with the solar images I derived the light curves shown in figure 4.5. For comparison, I made the same calculation also for a day with extremely low solar activity. I chose November 30th 2019 around 8h52m UTC. During this day the solar surface was virtually free of any blemishes. Also the contrast between brightest and darkest regions was much lower than in the 2014 images. Between November 14th 2019 and December 23rd 2019 the

[3] In this context the term active regions refers to spots and faculae.

international sunspot number was zero (Clette 2020). In this case the light curves show no small-scale variations even though asymmetries in the light curve are apparent. The asymmetries in the light curves are caused by insufficient flat field, guiding errors that lead to geometrical distorsions of the solar disk, large-scale inhomogeneities in the images introduced by variations of the sky transparency and stray-light. Although the Kanzelhöhe data archive also offers normalised images I decided not to use them. These images have also lost information about limb-darkening and brightness levels of large active regions. As figure 4.5 shows the the CaII K and the Hα light curves are significantly affected by active regions. A comparison between figures 4.4 and 4.5 reveals that bright features lead apparently to a deeper transit while dark features seem to reduce the transit depth. Also another aspect is highly interesting: both CaII K light curves are almost similar. The contributions of bright faculae and dark spots predominantly cancel each other. In comparison to the CaII K light curve the stellar activity is more pronounced in the Hα light curve. This is important because many authors conclude from a constant CaII K light curve or an S index time series that stellar activity is not responsible for variations in Hα but rather it must have been caused by the planetary atmosphere. Also we find that the 2014 transit seems to be shallower than the 2019 transit. This is caused by the fact that the bright active regions are predominantly outside of the transit path. Therefore the relative missing flux is smaller than R_P^2/R_S^2. If the transit path covered instead the active regions the Hα transit would seem to be deeper. Another complication to the transit light curves is introduced by prominences. Figure 4.6 compares the solar limb observations in the passbands of CaII K and Hα. While solar prominences can easily be observed in the Hα image this is not true for the CaII K observation. Here we cannot find any of the prominences. This leads to differences in transit light curves for these two passbands. The CaII K light curve is unaffected by the prominences within the measurement accuracy. This is not true for the Hα light curve.[4] As figure 4.6 demonstrates the shape of this light curve shows a transit signal prior to the planetary transit. Admittedly, this signal is by orders of magnitude smaller than claims of planetary pre-transit signals found in the literature (Cauley et al. 2015). Because the 24th solar cycle was not very strong it is possible that prominences during periods of higher activity are also more violent. During these periods huge prominences might be present as depicted in figure 4.7. In this scenario the stellar surface is completely free of activity features. The planet first occults the prominence and later the planet. While the spectrum of the stellar disk is dominated by a blackbody this is not true for the spectrum of the prominence. It is dominated by emission lines, in particular CaII H&K and the Balmer lines (Heasley and Milkey 1978). While the ratios between the intensities of the Balmer lines $I(H\alpha)/I(H\beta)$ and $I(H\alpha)/I(H\gamma)$ are constant this is not true for the $I(CaII_K)/I(H\alpha)$ and $I(CaII_H)/I(H\alpha)$ ratios. The ratio between $I(CaII_H)$ and $I(CaII_K)$ can approximately be described by a linear relation. It does not strongly deviate from unity. In contrast, this is not true for $I(CaII_K)/I(H\alpha)$. For low brightnesses $I(CaII_K)$ as a function of $I(H\alpha)$ is a rather steep function. In contrast, for high brightness values the curve flattens such that $I(CaII_K)/I(H\alpha) \ll 1$. In detail, this function depends on the pressure and temperature of the prominence. As lower the temperature is as lower also the $I(CaII_K)/I(H\alpha)$ ratio is. This implies that a huge, bright and comparatively cool ($T \approx 5000$K) prominence will be bright in the Hα line but faint in the CaII H&K lines. In extrasolar planetary systems such a prominence cannot be spatially resolved. Instead, all information about planetary atmospheres and their interactions with stellar wind have to rely on spectroscopic transit observations. During a prominence transit the emission line spectrum of the prominence will modify the depths of chromospheric lines while phospheric contributions to the observed spectrum will essentially be unaffected. Because the prominence is brighter in Hα than in CaII H&K the planetary disk will block a larger amount of Hα radiation than CaII emission and thus the transit is deeper in Hα than in CaII H&K. In contrast, during the transit of the stellar disk the flux of all chromospheric lines as well as the flux of the photospheric spectrum adjacent to the emission lines will be diminished by the same factor and thus the observed spectrum will be unaffected for a planet without atmosphere. Because of these complications discussed in this section, variations in transit depth cannot simply be ascribed to planetary atmospheres but rather a stellar origin is also a plausible explanation. As pointed out in Müller 2015 the effects of stellar active regions on X-ray light curves are even more extreme. In some wavelengths the light curves are such distorted that they are even not identifiable as transits. Another problem are stellar flares. As pointed out in Klocová et al. 2017 the active planet host HD 189733 clearly shows flares. An inspection of the light curves (their figure 7) reveals that in the middle of the transit an overlap of multiple flares exists. During the decline of the major flare two minor flares occur. Even more interesting is the fact that the flare's amplitude seems to be dependent on the

[4] For instance, Foukal 2013 notes that stellar prominences can also be observed among others in CaII K. This does not contradict the finding that they are not visible in the CaII K image. The reason is that these signals could be smaller than the noise of the CaII K image. This image only shows that the flux ratio between CaII K and Hα has an upper limit.

chromospheric line. While the amplitudes of both minor flares are roughly identical in the Hα line it differs both in the CaII H&K lines. In this case the first one was much stronger than the second one. If all flares during an observing run were like the second one we would obtain almost constant light curves in CaII H&K but the Hα light curve would significantly vary. Due to the orbital motion of the planet it blocks different parts of the stellar disk during the course of the transit. Additionally, the stellar rotation can bring surface features towards the observer or seemingly eliminate them. Therefore, it may happen that flare contributions are missing from time to time. This implies apparent temporal variations of chromospheric lines. These light curve excursions are obviously not caused by the planet. Because the occurrence rate of flares for stars other than the sun is poorly known I assume that solar flare statistics is also valid for them. In Winter et al. 2016 the authors conclude that the occurrence rate depends on the energy. As lower the energy is as higher the flare rate is. Because planetary transit observations require high S/N even small flares have to be taken into account. The aforementioned findings (surface features varying on longer timescales, prominences and flares) show that stellar activity severely compromises the interpretation of Hα light curves. In case of the white light observation we do not find any activity features in the light curves. Instead, the shapes of the light curves differ. A look into the FITS file headers reveals that the TELESCOP keyword for the 2014 observation is "KPT" while it is "KHPI" for the 2019 observation. Apparently, the white light telescope has been upgraded. For this reason, these differences are probably not related to intrinsic variations but are of instrumental origin. To minimise the impact of these instrumental artifacts I did not rotate the solar images. If systematic errors exist in the flat-field they will be identical in all images and lead to the same errors in the light curves. This implies that the planet's orbital plane is inclined with respect to the stellar equatorial plane.

Contrast of Stellar Active Regions

Such activity effects are especially important for stars with temperatures lower than the sun. For them the ratio of chromospheric to photospheric flux is higher. More quantitatively, Hall 1996 give conversions from $B-V$ color to continuum fluxes. Around the Hα line it is given by

$$\log \mathscr{F}_{c,H\alpha} = 7.538 - 1.081(B-V) \tag{4.7}$$

where $\mathscr{F}_{c,H\alpha}$ is given in erg/s/cm^2/Å. In Mamajek 2020 we find a relation between stellar temperatures and colors. The latter gives $B-V = 0.650$ for a G2 star and $B-V = 0.884$ for a K2 dwarf like HD 189733. Employing equation 4.7 yields $\mathscr{F}_{c,H\alpha,G2} = 6.8 \cdot 10^6$ and accordingly $\mathscr{F}_{c,H\alpha,K2} = 3.8 \cdot 10^6$. This implies that the contrast is higher by a factor of two if we assume identical chromospheric emission for both stars. Therefore, excursions as seen in figures 4.5 and 4.6 would be more prominent during a planetary transit orbiting an active K2 star. Additionally, the brightness ratio between a huge prominence and the stellar surface would also be higher. This value is highly speculative because the size and brightness of stellar prominences are unknown. Unfortunately, the long-term behaviour of chromospheric Hα emission is virtually unknown, even for the sun. Systematic studies of the depth of the solar Hα line started in the middle of the eighties (Livingston et al. 2007). Since then the measurements show the eleven year solar cycle. In contrast, activity variations have been monitored for decades in the CaII H&K lines, not only for the sun but for a variety of stars (Baliunas et al. 1995; Hall et al. 2007; Radick et al. 2018). In general, the chromospheric emission and its amplitude as determined by the Mount Wilson S index is as higher as lower the photospheric temperature is. To relate their findings to the temporal behaviour of the Hα line we need a relation between the depth of the Hα line and the chromospheric emission as measured in the emission cores of the CaII K&K lines. Such a relation is given in Martin et al. 2017. It should be noted that the relation averages over many individual observations. Regarding single measurements it stands out that there is a substantial scatter. This scatter might be related to the intrinsic properties of individual stars or to transient phenomena like flares. As discussed earlier no unique relation between Hα and CaII H&K exists for flares. For hot stars these effects are less pronounced. Due to the smaller activity variations in comparison to the photosphere hotter stars seem to be better targets. A major drawback is that transit observations suffer from the fact that $R_{planet}/R_\star$ is smaller for them.

4.4 Spectroscopic Phenomena Related to Planetary Transits

Rossiter-McLaughlin Effect

This effect induces an RV shift of stellar lines. It depends on the stellar rotation velocity. As faster the rotation is as more important this effect will become. For objects in prograde rotation a portion

of the stellar disk rotating towards us is blocked shortly after the first contact. Spectral observations discussed in this work have no spatial resolution of the stellar surface, i.e. spectra are disk-integrated minus the parts occulted by the planet. This implies that rotationally blueshifted light is missing in the disk-integrated stellar spectrum. Therefore, stellar lines will be skewed to longer wavelengths. When the planet is located exactly in the stellar disk's center from the observer's perspective, no RV shift is present. Shortly before the last contact a portion of the stellar disk rotating away from us is blocked. This leads to a skew towards shorter wavelengths. For retrograde orbiting planets the chronological order is inverse.

Center-to-Limb Variations

The term "center-to-limb variation" describes the finding that the observed spectrum depends on the limb angle. As presented in Czesla et al. 2015 the depth and with of an absorption line depends on the angle between the line of sight and the outward surface normal θ. At the stellar limb we mainly see the upper layers of the stellar atmosphere. In the center of the stellar disk we see deeper into the stellar atmosphere. In the course of a planetary transit first the stellar limb will be blocked by the planetary disk. In other words, the contribution by the limb spectrum will be reduced. During this phase the relative contribution by the disk center spectrum will be higher. Later, during mid-transit central regions of the stellar disk are blocked and thus the relative contributions shift. During egress, the contribution by the limb spectrum will be lower again. In summary, this leads to a symmetric light curve. Such a structure has been seen before by Czesla et al. 2015 in the CaII H&K and NaD transits of HD 189733 b.

Chapter 5

Planetary Transit Observations

In this chapter I present the results of bow shock observations of various planetary systems and introduce the observational methods. First, I start with the HD 189733 system because its observational method differs from the other observations presented in this work. From the observational results I also draw implications about the planetary magnetic fields of the planets (see chapter 6).

5.1 Nondetection of Planetary Bow Shocks in the HD 189733 system

At the start of this project the HD 189733 system was the only planetary system where a bow shock has been claimed (Cauley et al. 2015; Cauley et al. 2016). Later, the same authors have revised this statement and questioned the existence of a stable bow shock (Cauley et al. 2017a). They complied in total seven transit observations from 2006 to 2015 and found that the shapes of all transit light curves look different. In the case of a stable planetary bow shock it seems to be a reasonable assumption that all light curves are identical. In contrast, stellar activity leads to significant distorsions in the transit light curve as outlined in section 4.3.1. Due to the fact that the positions of active regions and prominences usually differ from one observation to the next also the light curves should reflect this variation. Interestingly, Cauley et al. 2017a found that the CaII H&K lines are not well correlated with the Hα equivalent width. As shown in section 4.3.1 a correlation between these chromospheric indicators is not necessarily given. In addition to slowly varying surface features also fast moving activity regions are certainly present. From solar observations the most well-known class are solar flares. According to Temmer et al. 2001 more than 700 subflares were recorded on the solar surface per month during the maximum of the 21st solar cycle. This corresponds to 0.94 flares per hour. Often, these flares are not equally distributed over a period of one month but occur during bursts (Pötzi 2020b). Due to the abrupt release of energy in one flare a chain reaction can be triggered. This leads to a burst of many flares during a short period of time as observed e.g. by Pötzi et al. 2015. This publication presents an example of more than one flare in a single Hα image taken on May 10th 2014. The individual flares are stochastically distributed. This implies that both the disk-integrated Hα and CaII H&K light curves will show a complex behaviour. Additionally, flare areas could enter the visible hemisphere or leave it due to stellar rotation in the course of a flare. Flares might also be accompanied by coronal mass ejections. While the active region itself is no longer on the visible hemisphere the ejected material might still be visible at a certain height over the disk. This further complicates the light curve. Especially strong flares are typically also long. In Temmer et al. 2001 the authors conclude that flares with importance classes[1] higher than one often last 57 minutes. On the sun such flares happen on average 5 times per month during solar activity maxima. Because HD 189733's activity is significantly higher it seems plausible that strong flares are much more frequent on this star. As pointed out in Winter et al. 2016 the X-ray flare rate is a strong function of the sunspot number. As higher the sunspots number is as higher also the flare rate is. Because all cool stars have coronae it is suggestive that these findings are also true for all cool stars. For instance Klocová et al. 2017 found one major and two minor flares during the course of almost five hours of observation. Unlike the sun HD 189733 is by far not observed continuously. Therefore, the total number of all flares divided by the observation hours is a highly uncertain proxy for the flare rate and thus the true flare rate is virtually unknown.

[1] The importance class gives the strength of a flare on a qualitative scale. As higher this value is as stronger the flare is.

To shed light on the pre-transit absorption signals of HD 189733 b the Hamburg Observatory started an observing campaign with the TIGRE telescope in 2017. In contrast to other transit observations we used a different observing strategy: if weather permits, HD 189733 was observed in every night. The observing program began in April and ended in November. Especially during the summer months the temporal coverage is low due to frequent bad weather. All data points are phase-folded and corrected for stellar activity. In this light curve I searched for planetary absorption features. In contrast to Cauley et al. 2015, Cauley et al. 2016 and Cauley et al. 2017a I could not find significant absorption signals related to the planet. The results and the data reduction are described in more detail in Kohl et al. 2018 which is also part of this thesis and reproduced in the second appendix after the bibliography.
Although the bow shock is not observable in this data set this does not imply its nonexsistence. It could be hidden in the activity-induced variations. Another possibility is that HD 189733 was not sufficiently active during the 2017 observing campaign. While it may not have been sufficiently active to form large prominences it may have been sufficiently active to produce rotational modulation by large starspots as seen in Kohl et al. 2018. In Bourrier et al. 2020 the authors analysed in total five transit observations in the course of three years. In only one observation they found an increased depth in the Lyα line. Although the total number of observations is low this shows that epochs of excess absorption seem to be rare. Of course, it's possible that the observations presented in Cauley et al. 2015 were taken exactly during such an epoch. Probably, also the observations presented in Jensen et al. 2012 were carried out during times of high stellar activity. Here, the authors present a clear detection of an Hα absorption feature. As shown in section 4.3.1 an Hα transit can also seem to be significantly deeper simply due to stellar activity. Because the transit depth depends in this case on the spatial distribution of active regions the same stellar activity level can lead to entirely different Hα transit depth. The inclination of HD 189733 b is 85.51 (Henry 2020) which corresponds to a planetary transit close the stellar equator. Long-term solar observations have shown over the last centuries that spots are located close to the equator at the end of a solar cycle and farther away during the maxima (Leussu et al. 2017). As pointed out in García and Ballot 2019 this is also true for stars other than the sun. If HD 189733 shows a similar behaviour the planet covers the bright active regions during the decline of an activity cycle. For this reason the transits are seemingly deeper during this period.

5.2 Search for Planetary Bow Shocks in Other Systems

To decide whether HD 189733 b is peculiar in regard to pre-transit absorption features I also analysed transit observations of other hot Jupiters. These were aquired at different observatories with a variety of telescopes and instruments. Therefore, the data set is rather inhomogeneous. Even transit observations taken with the same instrument differ significantly. This is due to the fact that instrument configurations varied from one observing run to the next. For instance, both WASP-69 and WASP-131 have been observed with the UVES spectrograph but the recorded wavelength ranges differ because of employed instrument configuration. In most points, the data reduction process is similar for all observing runs and works as described in Kohl et al. 2018. A major difference here is that I do not subtract an inactive template spectrum. This restriction is imposed by the fact that this work mainly uses archival observations. Observations of template spectra with identical instrumental configurations are usually not available. For this reason the absolute equivalent widths of stellar lines are unknown. In contrast, even small changes can be tracked during the course of a night. A minor drawback is that observations taken at different nights with different instruments cannot directly be compared. Likewise, the amplitude of stellar activity variations cannot be given on an absolute scale, but this is not necessary in the scope of this work. To assess the systematic errors caused by instrumental effects, telluric contamination and stellar activity I check the consistency between different activity indicators and adjacent photospheric lines. The latter never show any obvious excursions. Instead, these are constant within their error bars. The lines of interest in this work are Hα, Hβ, CaII H&K and the CaII infrared triplet. In most observing runs not all of the aforementioned lines are available. For this reason the details of the analysis differ from observation to observation.

5.3 WASP-69 b

Another target of interest is WASP-69 b. This planet has been discovered in 2014 by Anderson et al. 2014. Like HD189733 also this host star is a K dwarf, but there are also differences. First, WASP-69 b is less massive. Another significant difference between these host stars is their age: WASP-69 is probably

Table 5.1: Wavelength ranges used for telluric correction. The row "species" describes what molecule is primarily responsible for the absorption lines in this region according to Smette et al. 2015 and the row "object" describes where this wavelength range has been used for telluric correction. "W69" is WASP-69 and "W131" is WASP-131.

species	O_3	O_2	O_2	H_2O	O_2	H_2O	H_2O	O_2	H_2O
object	W69	W69	W69	W69	W69	W69	W69	W131	W131
lower wavelength[Å]	5880	6270	6854	7160	7594	8120	8969	6260	6460
upper wavelength[Å]	6000	6319	6940	7340	7701	8340	9450	6333	6520

younger than HD 189733. While the former is presumably 5.3±3.8 Gyr old the latter is ≈2 Gyr old. According to Anderson et al. 2014 strong emission cores can be found inside the CaII H&K lines. This is in line with the finding that WASP-69 is a strong X-Ray source (cf. table 5.4). According to SPHERE observations presented in Bohn et al. 2020 it is improbable that WASP-69 is actually a multiple system: at a distance of 0.2 arcseconds the authors rule out companions with masses above $74 M_{Jup}$. For this reason the aforementioned activity indicators must be produced by the host star itself. These facts imply that WASP-69 is in general an active host star, similar to HD 189733. Due to the similarities I assume that the interplanetary environment of the WASP-69 system is comparable to HD 189733's environment.

Details About the Observing Run

This target was observed by the UVES spectrograph on the night beginnig August 31st 2016 (program ID: 097.C-0863(A), PI: Michael Salz). During this observing run the blue arm was tuned to the wavelength region between 3,760Å and 4,980Å while the first CCD of the red arm covered the range from 5,700Å to 7,530Å and the second CCD covered 7,660Å to 9,460Å. In this wavelength range a variety of telluric bands are located. Their exact positions are given in table 5.1. These I used to fit the strength of the telluric absorption. In the case of the reddest H_2O band I could only use parts of it due to the incomplete wavelength coverage at the edge of the detector. Like in the case of HD 189733 a large number of stellar absorption lines inside these bands had to be masked.

Results

The light curves of the transit are shown in Figures 5.1 and 5.2. These figures show the Mount Wilson S index in its native unit and for all other lines the figures show the area under the normalised flux F_{norm} as given by

$$I = \int_{\lambda_{min}}^{\lambda_{max}} F_{norm}(\lambda)\, d\lambda \tag{5.1}$$

with the parameters λ_{min} and λ_{max} given in table 5.2. The most striking feature in all light curves is

Table 5.2: Integration limits as given in equation 5.1. All wavelengths are given in vacuum and are corrected for barycentric motion and stellar radial velocity. There is a small gap between the upper limit of Hα_b and lower limit of Hα_r due to the finite spacing of data points.

	Hα	Hα_b	Hα_r	Hβ	Hα	Hβ
object	W69	W69	W69	W69	W131	W131
λ_{min}[Å]	6563.82	6563.82	6564.70	4862.33	6563.42	4861.77
λ_{max}[Å]	6565.57	6564.68	6565.57	4863.06	6564.75	4862.90

a strong flare that occurred around 0.6188 HJDs. For the approximate determination of the point in time of the flare onset I used the temporal evolution of the Mount Wilson S index[2]. Left of the dashed vertical line the S index is more or less constant. Right of it we see a sharp increase. Because the temporal cadence of almost 6 minutes is rather coarse I assumed that the flare began exactly between the two data points. Although it is quite unlikely that both S_{MWO} and the Balmer lines are affected

[2]The derivation of the Mount Wilson S index from UVES spectra will be discussed later in section 6.2.

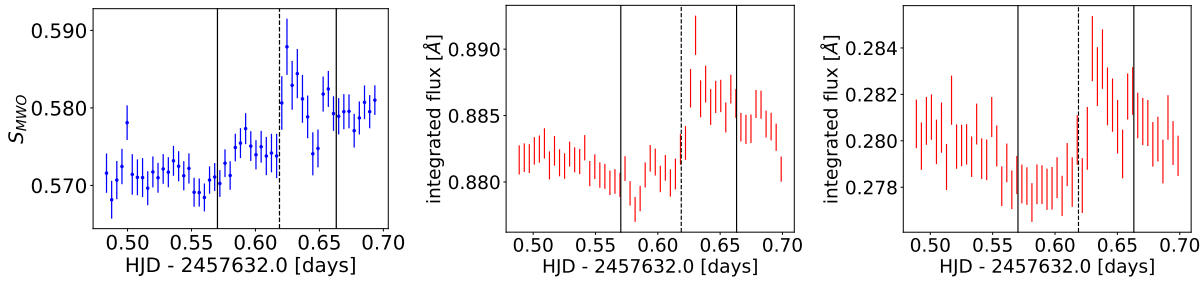

Figure 5.1: S_{MWO} (left) as well as Hα (middle) and Hβ (right) transit of WASP-69b observed on August 31st 2016 with UVES. The dashed vertical line denotes the flare onset at 0.6188 HJDs.

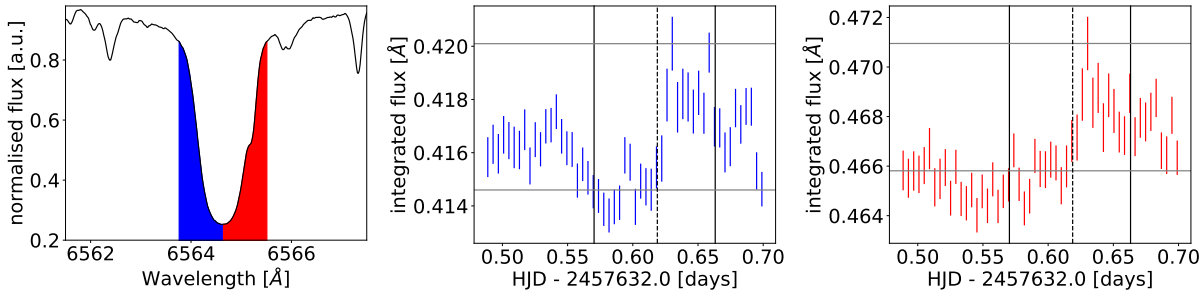

Figure 5.2: Left: Integration bands of the blue and red wing of the Hα line. The lower horizontal line is the average of all data points recorded after the ingress but before the flare onset. The upper one is the light curve's maximum. Middle: integrated flux in the blue wing of the Hα line. Right: ditto, but for the red wing.

by instrumental artifacts or physical processes of unknown nature I attempt to verify the nature of this event. For this purpose I divided the Hα line into a blue and a red wing as shown in figure 5.2. For both wings I evaluated I independently and found that the amplitude is 5.5mÅ in the case of the blue wing and 5.1mÅ in the case of the red wing, respectively. The excess in the blue wing implies that the material is moving towards the observer with a velocity of several hundred km/s. Typically, such high velocities and direction of motion have been regularly found in the framework of solar flare observations (Foukal 2013). At the end of the transit the last three data points in the S index time series could be interpreted as another minor flare. However, when we also inspect the hydrogen light curves we do not find consistent counterparts. Due to the presence of a flare this data set is by far not optimal to search for bow shocks. To my best knowledge this is the only data set completely covering a transit of WASP-69 with a spectral resolution of 110,000 and having a signal to noise ratio as high as 70 in the Hα region. For this reason I attempt to gain information about the bow shock from the data points unaffected by the flare, i.e. before the flare onset. These data points I divide into two samples: one before the first contact of the planet (called pre-transit sample) and one after it (called in-transit sample). Now I check if the pre-transit and in-transit samples differ from a statistical point of view. As pointed out in table 5.3 the averages of pre- and in-transit usually do not vary significantly. For Hα and Hα_r the variations are completely insignificant. Only for S_{MWO}, Hα_b and Hβ these are somewhat significant (1.5σ vs. 2.1σ vs. 2.3σ). Visual inspection of the Hα_b light curve reveals that the integrated flux decreases during planetary ingress, i.e. the blue wing is absorbed more strongly than the red wing. A natural explanation for this behaviour is the RossiterMcLaughlin effect as discussed in section 4.4. Planetary prograde rotation leads to an absorption excess in Hα_b. For comparison, Cauley et al. 2015 derive a depth of 9mÅ in Hβ and the signal in Hα should be even stronger! Therefore, I tend to interpret these signals as fluctuations and not as a planetary signal. In contrast to HD 189733 b's transit we do not find any evidence for a planetary bow shock. A bow shock as shallow as 1-2mÅ might still be present but I assume it will be difficult to reliably detect such small signals with current instrumentation. This indicates that strong planetary bow shocks are not ubiquitous for planets around cool stars.

Table 5.3: Variation of stellar activity and planetary absorption before the flare onset. For S_{MWO} it is reported in its native unit. In all other cases I is given in mÅ. Hα_b and Hα_r denote I of the blue and red wing of the Hα line, respectively.

	S_{MWO}	Hα	Hα_b	Hα_r	Hβ
pre-transit	0.571±0.002	881±1	416.1±0.7	465.3±0.7	279.8±1.0
in-transit	0.574±0.002	880±1	414.6±0.7	465.8±0.8	278.2±0.7

5.4 WASP-131 b

Another possible target is WASP-131b. In contrast to WASP-69 this host star is of spectral type G0. The host star could be regarded as an older and inactive sibling of the sun. This probably significantly reduces the contamination of the Hα light curve by stellar activity. The planet was discovered in 2017 by Hellier et al. 2017. At this time it was not yet known that WASP-131 is acutally a binary system. Later, Southworth et al. 2020 published SPHERE observations of this target. At an angular distance of 0.189 arcseconds they found a secondary component with a K band magnitude difference of 2.82. Because a physically unrelated background star is unlike they concluded that the system consists of a primary star with T_{eff}=5,950K and a companion with T_{eff}=4,109K and $M = 0.62M_{\odot}$. According to Mamajek 2020 this corresponds to a K7 dwarf. Due to its small distance it could in principle contaminate the observed spectrum, if the companion is in an active state. At the time of discovery the atmospheric composition was unknown and as of March 2021 Henry 2020 still does not list publications clarifying it. The planet's radius and mass imply an extremely low density (cf. table 5.5). This density is even lower than the bulk densities of the gas giants in the solar system. Even Saturn's density is higher: $0.52\rho_{Jup}$ (Park 2020). For this reason and because of the planet's equilibrium temperature, a large bloated atmosphere seems to be a plausible assumption. Furthermore, its bloated atmosphere is prone to mass loss which may also be detected by accretion. This fact in combination with the host star brightness of m_V=10.1 makes WASP-131 b an ideal target for pre-transit absorption studies.

Details About the Observing Run

This target was observed by UVES on May 3rd/4th 2017 (program ID: 099.C-0586(B), PI: Sara Khalafinejad). During this observing run the blue arm was tuned to the wavelength region between 3,400Å and 4,510Å while the first CCD of the red arm covered the range from 4,790Å to 5,750Å. The second CCD covered the redder part from 5,840Å to 6,800Å. This choice of wavelength ranges was made to fulfill the scientific requirements of the P.I.'s program. However, it severly limits the availability of strong telluric bands. While several strong bands can be found longward of 6800Å this is not true blueward of this limit. Here, only two bands can be found (see table 5.1). Unfortunately, both the O_2 and the H_2O band are rather weak. A small degradation of the scientific results caused by residuals of telluric contamination cannot be fully ruled out. It should be noted that the water lines are potentially important in the region of the Hα line. However, as will be discussed later a major impact of this issue seems to be unlike. For dry places located at high altitude the availability of strong telluric bands for atmospheric abundance fitting is not so critical.

Stellar activity of the host star

Fig. 5.3 shows the temporal evolution of stellar activity as measured by the Mount Wilson S index and the light curves of the Hβ and Hα lines. The integration bands are given in table 5.2. They slightly differ from WASP-69 b's bands because of different instrument configurations. To disentangle stellar activity and planetary absorption I first focus on the former. Because the wavelength range of the CaII H&K lines is free of telluric absorption lines I assess stellar activity based on this indicator. Originally, the UVES spectrograph has not been constructed to measure the Mount Wilson S index. Therefore the spectra of the UVES blue-arm have to be converted to the standard Mount Wilson S index activity indicator as described in section 6.2. The mean stellar activity found during the course of the observing run is 0.151. This value is even lower than the maximum of the 24th solar cycle but rather comparable to the last solar minimum as determined by Schröder et al. 2017. The S index is relatively constant during long periods of the observing run. In contrast, the beginnig and end show obvious temporal variations. It seems that the stellar activity declines during these phases. To determine if this is an instrumental artifact I analyse

Table 5.4: Properties of WASP-69 b and its host star. In the case of the age the authors note that this value is rather uncertain. Depending on the methodology the authors find discrepant results ranging between 0.5 and 3 Gyr.

Parameter	Value	Ref.
	WASP-69	
m_V	9.87	Wenger et al. 2000
$M_B - M_V$	1.06	Wenger et al. 2000
Spectral Type	*K5*	Anderson et al. 2014
T_{eff}[K]	4715 ± 50	Anderson et al. 2014
$\log(g)$	4.535 ± 0.023	Anderson et al. 2014
$[M/H]$	0.144 ± 0.077	Anderson et al. 2014
$v_{\rm rot}$[km/s]	1.78 ± 0.06	Anderson et al. 2014
Rotation period [d]	23.07 ± 0.16	Anderson et al. 2014
$v_{\rm rad}$[m/s]	−9,628.26 ± 0.23	Anderson et al. 2014
Distance [pc]	49.96±0.13	Bailer-Jones et al. 2018
$\log(R'_{HK})$	−4.54	Anderson et al. 2014
L_X/L_{bol}	−4.43	Anderson et al. 2014
age [Gyr]	≈2	Anderson et al. 2014
Mass [$M_\odot$]	0.826 ± 0.029	Anderson et al. 2014
Radius [$R_\odot$]	0.813 ± 0.028	Anderson et al. 2014
	WASP-69 b	
Planet mass [M_{Jup}]	0.260 ± 0.017	Anderson et al. 2014
Semi-major Axis [AU]	0.04525 ± 0.00053	Anderson et al. 2014
Eccentricity	< 0.11 at 1σ	Bonomo et al. 2017
Orbital period [d]	3.8681382 ± 0.0000017	Anderson et al. 2014
Planetary radius [R_{Jup}]	1.057 ± 0.047	Anderson et al. 2014
Duration of transit [h]	2.23 ± 0.03	Anderson et al. 2014
Transit depth [%]	1.786 ± 0.042	Anderson et al. 2014
Planetary density [ρ_{Jup}]	0.219 ± 0.031	Anderson et al. 2014
Equilibrium temperature[K]	963 ± 18	Anderson et al. 2014
Exposure Time[s]	300	This work.

the spectrograph's RV stability and FWHM. The former is given in fig. 5.4 and calculated as follows: first I chose in total 53 stellar lines located between 3918.10Å and 3992.95Å in the vicinity of the CaII H&K lines. For every stellar line in each spectrum I calcluated the line centroid, its width and error bars of these quantities under the assumption that the line profile can adequately be modeled by a Gaussian function. In the next step I calculate a temporal mean line position for all of the 53 stellar lines. Based on this mean position I determine the individual RV shift for every stellar line in each spectrum. In the last step I average over the individual RV shifts in each of the 92 observed spectra. By propagation of errors I also obtained error bars for the final values. The same procedure I also used to derive average FWHMs as shown in figure 5.5. Because some out of the 53 stellar lines are rather shallow the fitting procedure failed in rare cases, e.g. when the spectra were affected by low signal to noise. In total, $< 1\%$ out of 4876 individual line measurements failed or were excluded because they were obvious outliers. A comparison between figures 5.3 and 5.5 reveals that the width of stellar lines increases at the end of the transit. This behaviour is clearly correlated to the airmass during observations. At around 0.67 days the airmass is approximately 1.1 but increases to 2.8 at the end of the transit. At this time the stellar light has to traverse a larger air column in comparison to the observations carried out at 0.67 days. This in turn leads to a more pronounced seeing. As outlined in section 2.2 this higher seeing implies a higher FWHM of spectral lines and an effective decrease of spectral resolution. Visual inspection of the blue-arm spectra show that the CaII H&K lines are as broad as 20Å. In contrast, the integration bands centered on the line cores have a width of 1Å (Melo et al. 2006), i.e. the line is by far not completely covered by the integration band. Because the integration band is considerably narrower than the CaII lines the temporal variability of the linewidth implies a temporal variation of the flux inside of the integration band (see section 2.2). Another instrumental problem affecting the integrated flux are radial-velocity

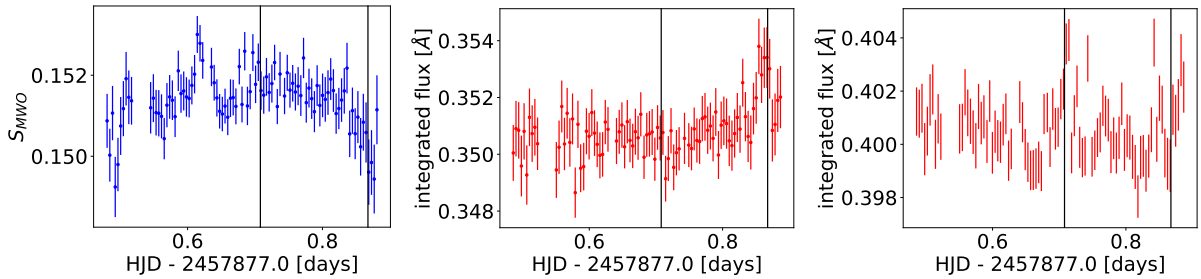

Figure 5.3: Temporal evolution of S_{MWO} (left), Hβ (middle) and Hα (right) during transit of WASP-131 b observed on May 4th 2017 with UVES. In the case of S_{MWO} one outlying data point with an abnormal large error bar has been removed.

instabilities. An inspection of figure 5.4 shows that the RV stability during this observing run leaves a lot to be desired. Especially the pre-transit phase and the beginnig of the transit show a pronounced RV anomaly. Interestingly, this anomaly is not apparent in the light cures as figure 5.3 shows. Around 0.6 days we find an excess whose temporal evolution resembles a solar flare. Interestingly, we do not see a comparable excess in the other time series. According to Johns-Krull et al. 1997, who studied a solar flare on March 6th 1993, the equivalent-width of the excess emission in the Hβ line is roughly comparable to the equivalent-width of the CaII K line. Additionally, it is about a factor of 2 higher in the Hα light curve. Such an excess we would be able to see as demonstrated by the WASP-69 data in section 5.3. This flare is readily visible in all chromospheric lines. Since WASP-131 is of spectral type G0 and its stellar activity is comparable to solar behaviour I assume that its flares can also be adequately described by employing solar models. Because the temporal evolution of the S index and the hydrogen light curves contradict the nature of this emission feature is unclear. The aforementioned manifestations for low stellar activity by an overall low and predominantly constant S index value are further supported by the absence of photometric stellar variability. According to Oelkers et al. 2018 the stellar light curve is constant within its error bars of 0.01 mag. To validate this finding I also search for temporal variations in the Hydrogen light curves. As we see in the same figure also the Balmer light curves are often constant within the error margins. In contrast, close to the end of the transit there seems to be some excess absorption in the Hβ light curve. A comparison to figure 5.5 shows that at the same moment also the FWHM shows an excursion. Therefore, I assume that this is an instrumental artifact and not an intrinsic variation.

Search for Pre-Transit Absorption

In Cauley et al. 2015 the authors conclude that the absorption by a bow shock is strongest in the Hα line. In contrast, apart form a few outliers figure 5.3 shows that the Hα light curve is free of temporal variability, especially during the pre-transit phase. A comparison with the Hβ light curve is in line with this finding. This implies that planetary absorption features must be smaller than the standard deviation of the data points of 1.1mÅ. These observations do not support the presence of a bow shock. They also rule out the presence of an accretion stream. It should be kept in mind that this value refers to today's absorption. In the past (several million years ago) the planetary absorption spectrum could have shown strong atmospheric absorption or an accretion stream. Today, the volatile components are probably gone due to atmospheric escape.

5.5 KELT-7 b

KELT-7 is substantially hotter than WASP-69 and WASP-131 discussed previously (cf. table 5.6). Also KELT-7 b is the second-hottest planet that is regarded in this work. Its close orbit has the important consequence that the stellar wind density is high, too. In turn, a strong interaction between planetary atmosphere and stellar wind can be expected. This interaction may lead to a strong and thus easily detectable bow shock as outlined in chapter 6.
As usual, data reduction steps were in accordance with Kohl et al. 2018. For the fitting of telluric absorption strength I use the bands given in table 5.7. The spectrum of an F star contains fewer lines than the spectra of cooler K or G stars. Therefore, the number of exclusion regions in the telluric bands

Table 5.5: Properties of WASP-131 b and its host star. In the case of the age the authors state that a value of 7.5 is most likely while the 95% confidence interval ranges between the limits given in the table.

Parameter	Value	Ref.
	WASP-131	
m_V	10.07	Wenger et al. 2000
$M_B - M_V$	0.55	Wenger et al. 2000
Spectral Type	*G0*	Hellier et al. 2017
T_{eff}[K]	5950 ± 100	Hellier et al. 2017
log (g)	3.9 ± 0.1	Hellier et al. 2017
$[M/H]$	−0.18 ± 0.08	Hellier et al. 2017
$v_{\rm rot}\sin(i)$[km/s]	3.0 ± 0.9	Hellier et al. 2017
$v_{\rm rad}$[km/s]	−19.39 ± 0.38	Gaia Collaboration 2018
Distance [pc]	200.1 ± 2.6	Bailer-Jones et al. 2018
age [Gyr]	between 4.5 and 10.1, most likely 7.5	Hellier et al. 2017
Mass [$M_\odot$]	1.06 ± 0.06	Hellier et al. 2017
Radius [$R_\odot$]	1.53 ± 0.05	Hellier et al. 2017
	WASP-131 b	
Planet mass [M_{Jup}]	0.27 ± 0.02	Hellier et al. 2017
Semi-major Axis [AU]	0.0607 ± 0.0009	Hellier et al. 2017
Eccentricity	< 0.10 at 2σ	Hellier et al. 2017
Orbital period [d]	5.322023 ± 0.000005	Hellier et al. 2017
Planetary radius [R_{Jup}]	1.22 ± 0.05	Hellier et al. 2017
Duration of transit [h]	3.83 ± 0.03	Hellier et al. 2017
Transit depth [%]	0.665 ± 0.012	Hellier et al. 2017
Planetary density [ρ_{Jup}]	0.15 ± 0.02	Hellier et al. 2017
Equilibrium temperature[K]	1460 ± 30	Hellier et al. 2017
Exposure Time[s]	300	This work.

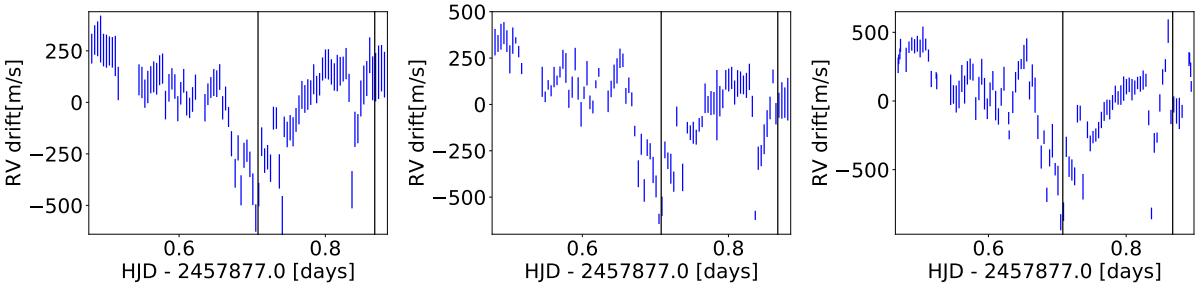

Figure 5.4: Temporal evolution of the average radial velocity of stellar lines in the vicinity of the CaII H&K (left), Hβ (middle) and Hα (right) lines.

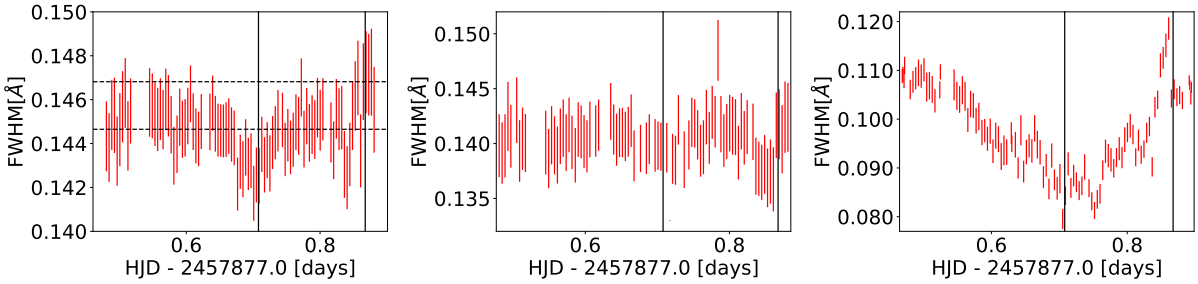

Figure 5.5: Same as figure 5.4 but for the average FWHM of the aforementioned lines. In the CaII H&K plot the lower dashed line denotes the median value of the whole observing run while the upper line denotes the median of all data recorded after HJD=0.846. These are located at 144.7mÅ and 146.8mÅ, respectively.

Table 5.6: Properties of KELT-7 b and its host star. In the case of the planetary density I took the value from Bieryla et al. 2015 and used Park 2020 to convert it to the value given in the table.

Parameter	Value	Ref.
	KELT-7	
m_V	8.54	Bieryla et al. 2015
$M_B - M_V$	0.43	Bieryla et al. 2015
Spectral Type	*F2*	Wenger et al. 2000
T_{eff}[K]	$6789\ ^{+50}_{-49}$	Bieryla et al. 2015
$\log(g)$	4.149 ± 0.019	Bieryla et al. 2015
$[M/H]$	$0.139\ ^{+0.075}_{-0.081}$	Bieryla et al. 2015
$v_{\rm rot}\sin(i)$[km/s]	$65.0\ ^{+6.0}_{-5.9}$	Bieryla et al. 2015
$v_{\rm rad}$[km/s]	40.75 ± 0.80	Wenger et al. 2000
Distance [pc]	136.7 ± 0.9	Bailer-Jones et al. 2018
age [Gyr]	1.3 ± 0.2	Bieryla et al. 2015
Mass [$M_\odot$]	$1.535\ ^{+0.066}_{-0.054}$	Bieryla et al. 2015
Radius [$R_\odot$]	$1.732\ ^{+0.043}_{-0.045}$	Bieryla et al. 2015
	KELT-7 b	
Planet mass [M_{Jup}]	1.28 ± 0.18	Bieryla et al. 2015
Semi-major Axis [AU]	$0.04415\ ^{+0.00062}_{-0.00052}$	Bieryla et al. 2015
Eccentricity	0.00	Stassun et al. 2017
Orbital period [d]	2.7347749 ± 0.0000039	Bieryla et al. 2015
Planetary radius [R_{Jup}]	$1.533\ ^{+0.046}_{-0.047}$	Bieryla et al. 2015
Duration of transit [h]	$3.5112\ ^{+0.02328}_{-0.02208}$	Bieryla et al. 2015
Transit depth [%]	0.828 ± 0.012	Bieryla et al. 2015
Planetary density [ρ_{Jup}]	$0.333\ ^{+0.055}_{-0.051}$	see caption
Equilibrium temperature[K]	2048 ± 27	Bieryla et al. 2015
Distance [pc]	136.68 ± 0.93	Bailer-Jones et al. 2018
Exposure Time[s]	900	This work.

is also lower. This in turn leads to a slight improvement in the quality of the telluric absorption model. Even more important is the fact that both the Hα and the Hβ line are isolated and predominantly free of other stellar lines overlapping them. This simplifies the data analysis.

Stellar Companion Searches

The instrumental point spread function of the spectrograph is 2 arcseconds. At KELT-7's distance this corresponds to 273.4 AU. A companion at this distance has a negligible impact on KELT-7 and its planet but it is still important from an observational point of view. While the observation targets KELT-7 any companions inside this range contaminates the observed spectrum. Despite various efforts to search for it such a companion has not yet been found. In the discovery paper the authors could limit companions fainter than 2.5 mag (effective wavelength 2.1654µm) at an angular separation of 0.1 arcseconds. Also Wöllert and Brandner 2015 and Coker et al. 2018 have been searching for companions of KELT-7 but report negative results. Wöllert and Brandner 2015 conclude that the second component must be within 0.25 arcseconds and fainter by 3.86 mag in SDSS z' band. Coker et al. 2018 limit the R band brightness difference to 3.58 mag and the I band brightness difference to 4.20 mag for companions within 0.2 arcseconds. These observations imply that a putative massive companion must be closer than $\approx$0.25 arcseconds. Another evidence of the absence of an active companion is the photometric stability of the KELT-7 broadband light curve. For these reasons I conclude that activity variations by a companion are improbable.

5.5.1 2016 Observation

A first transit observation was carried out during the night beginning November 19th 2016 at the ESPERO spectrograph. For a technical description of the instrument and its configuration I refer to chapter

Table 5.7: Wavelength ranges used for telluric correction. The row "species" describes what molecule is primarily responsible for the absorption lines in this region according to Smette et al. 2015. Because the reddest H_2O band was not covered by ESPERO it could only be used for the CARMENES observation of this target (see next subsection).

species	O_3	O_2	O_2	H_2O	O_2	H_2O	H_2O
lower wavelength[Å]	5899	6270	6860	7160	7590	8120	8900
upper wavelength[Å]	6000	6320	6940	7340	7700	8340	9200

2.7. In contrast to most other observations discussed in this work observing time has been explicitly awarded to this project. This allowed to tailor the observing run with regard to the specific requirements of pre-transit observation. For this reason the coverage of the pre-transit phase is very long. Since I was mainly interested in the bow shock and allocation of telescope time was restricted by other scientific projects I accepted also observing nights that did not allow coverage of the post-transit phase.

The Balmer Light Curves

Figure 5.6 shows the integration band around the Hα line as well as the Hα light curve. The magnitude of the error bars is approximately $\pm$5Å on average. This allows to exclude pre-transit features with an absorption depth on the order of 10mÅ with high confidence. During pre-transit phase the light curve is esentially flat. Beginning with the transit we find a sharp decline of the integrated flux, i.e. the absorption in Hα becomes substantially stronger. Its significance is 4.5 standard deviations (see table 5.8). This is a clear indication of planetary absorption by an extended hydrogen atmosphere.
At HJD = 2457711.64 days an outlier seems to be present. To resolve the issue I inspected the raw CCD frame of this observation. The relevant section of it is shown in figure 5.7. It demonstrates that the core of the Hα line is affected by a single bright pixel. An inspection of the neighbouring pixel shows two important facts. First, this feature mainly affects a single row. Second, it is smaller than the instrumental PSF. Therefore, I assume that this is not part of the stellar spectrum but a charge deposition by an energetic particle. As Groom 2002 points out these may be caused by cosmic particles or the decay of radioactive isotopes in the CCD material. As figure 5.7 clarifies not only the Hα line was affected but also an adjacent order. In this case the charge was even larger. When extracting the spectrum from such a CCD frame prominent artifacts can be generated as the right plot shows. These will then manifest as unrealistic high values as figure 5.6 demonstrates. To fix the spectrum I replaced the affected data points. Between the data points located at 6564.14 and 6564.48Å I calculated a straight line. Now I replaced all eight data points between them. With this fixed spectrum I repeated the calculation of the integrated flux. Now this data point is in line with its neighbours as figure 5.6 shows.

Because the Hα line shows strong indications of a planetary signal also the Hβ light curve should show a comparable signal. Inspection of figure 5.8 shows that this seems to be the case. An important difference between Hβ and Hα light curve is that the first two in-transit data points do not show excess absorption. Because of this discrepancy in the light curves I searched for deviations in single pixels as discussed previously in the case of the Hα spectrum observed at HJD = 2457711.64 days. These could have explained the outliers but I was unable to find such artifacts in relevant regions. Next, I checked if the continua of all spectra are identical. Normally, the division of two randomly selected spectra should be unity within the instrumental error bars. This is due to the fact that the stellar spectrum is virtually constant and variations induced by planetary absorption or stellar activity jitter are small. For most spectra I could verify that this is indeed the case. However, for some spectra I found that the division shows prominent ripples and a linear trend. This is exemplified in figure 5.9. It is quite remarkable that the positions of the echelle orders correspond with the jumps in $S_{6715}(\lambda)/S_{4311}(\lambda)$. The subscript denotes the fractional part of the HJD. I assume that these ripples are not of astrophysical origin but are instrumental artifacts. This problem leads to severe systematic errors in the normalisation procedure of the spectra. Of special importance is the fact that two echelle orders contribute to the merged spectrum in the Hβ region. This compromises the comparability of spectra recorded at different times and introduces systematic errors in the light curve. This issue is not restricted to the spectrum observed at HJD = 2457711.6715 but all spectra after this time are affected. For this reason I flagged problematic data points in figure 5.8. At first glimpse the light curve shown in figure 5.8 gives the visual impression of a planetary absorption also in the Hβ light curve. However, the credibility is severly limited

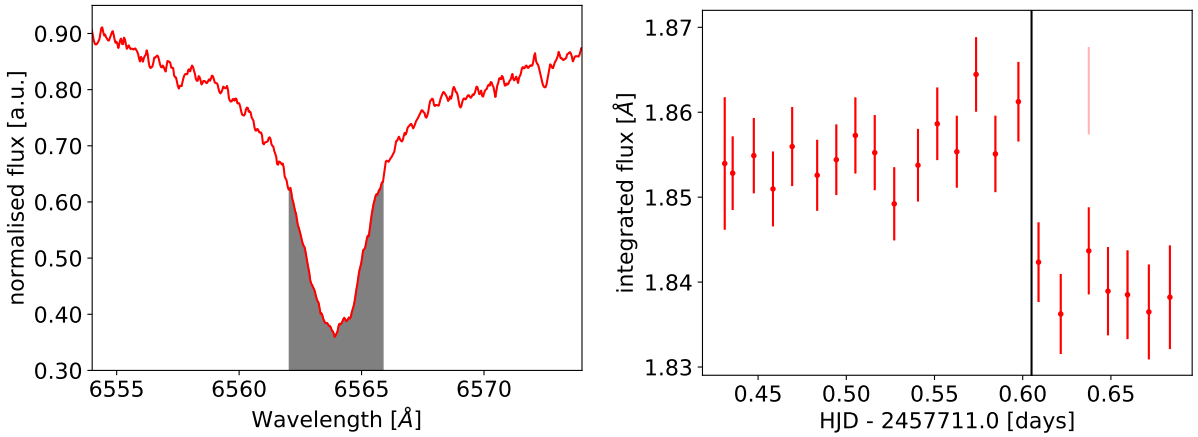

Figure 5.6: Left: Telluric corrected spectrum and integration band from 6562Å to 6566Å around the Hα line core. Right: Integral versus time. Transit of KELT-7b observed on November 19th 2016 with ESPERO. The solid line denotes the first contact. At HJD = 2457711.64 days a data point affected by a cosmic has been corrected. The original data point is drawn in pale red and the corrected one in bright red.

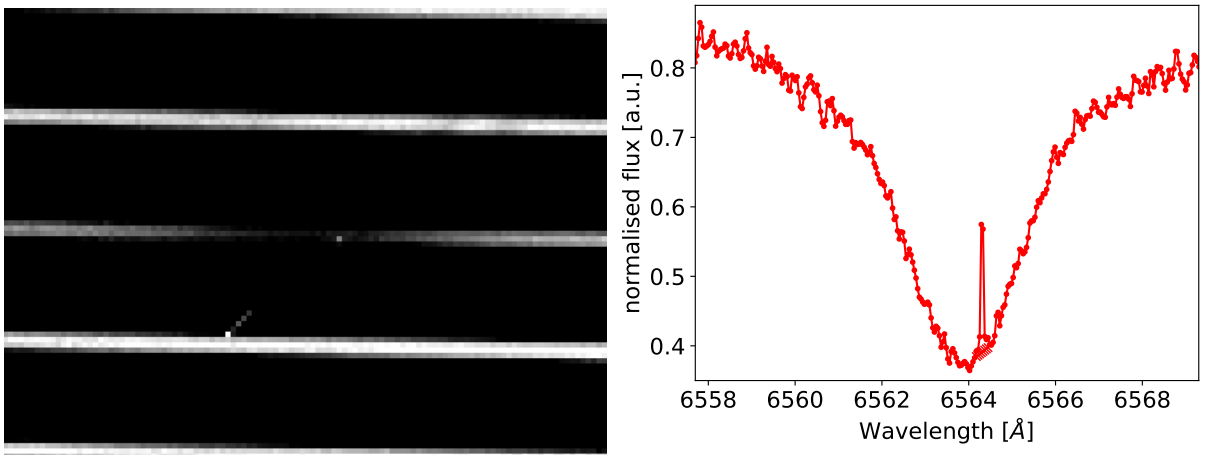

Figure 5.7: Left: Portion of the raw CCD frame recorded at HJD = 2457711.64 days. It shows part of the echelle order containing the Hα line. Right: corresponding spectrum in the region of the Hα line. A zoom into the relevant wavelength region is shown in figure 5.10.

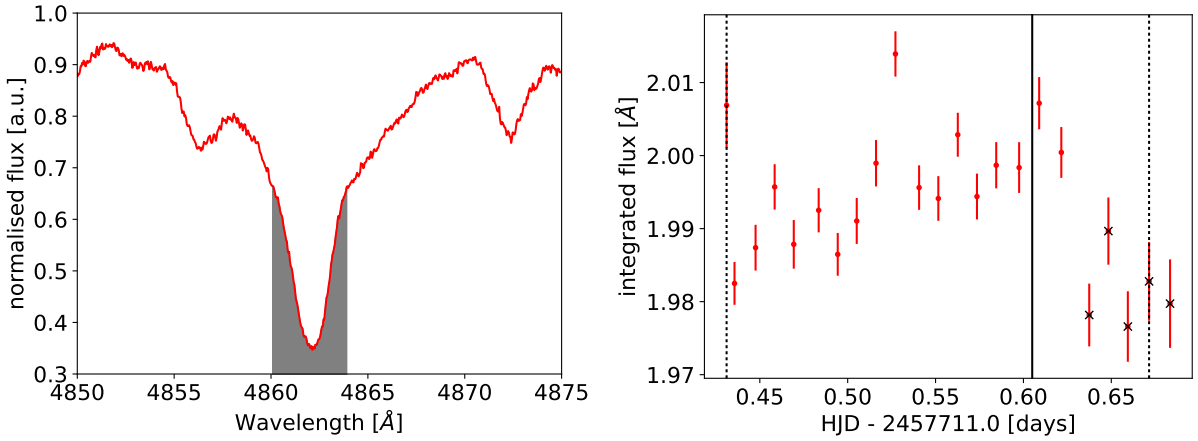

Figure 5.8: Left: integration band around the Hβ line ranging from 4860Å to 4864Å. Right: resulting light curve. Crossed out data points are affected by ripples in the region of the Hβ line. The spectra marked by the dotted lines are shown in figure 5.9.

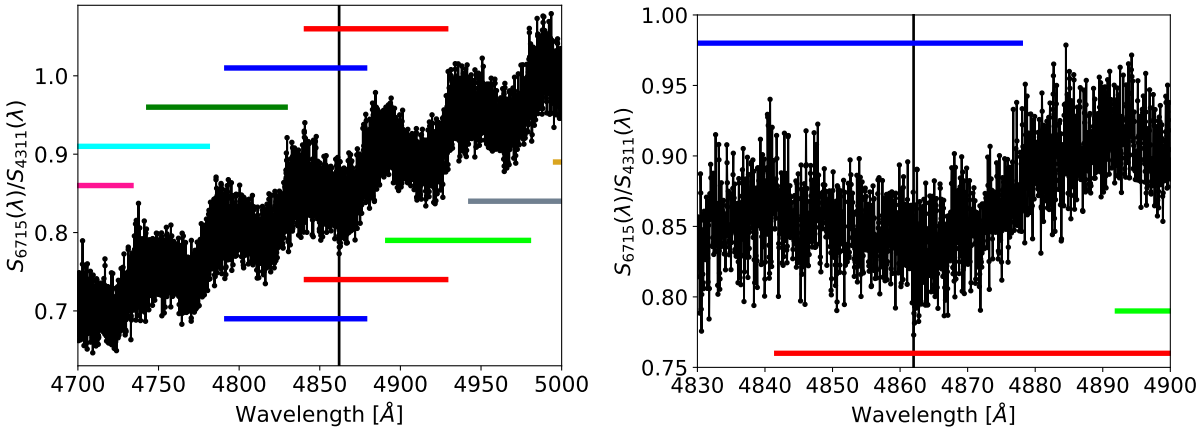

Figure 5.9: Left: Division of the spectrum observed at HJD = 2457711.6715 by the spectrum observed at HJD = 2457711.4311. The vertical line denotes the position of the Hβ line and the coloured lines give the wavelength ranges of the echelle orders. Right: the same but zoomed in into the region of the Hβ line.

for most of the in-transit data points. For this reason table 5.8 lists the average in-transit value both under inclusion and exclusion of the doubtful data points. In contrast, the Hα region is not affected by this problem.

Comparison to CaII IRT

To evaluate a stellar origin of the feature an analysis of the calcium infrared triplet was performed. In contrast to the procedure described in Kohl et al. 2018 only the first CaII IRT line could be used. The second IRT line partially falls into a gap between adjacent echelle orders and the signal to noise ratio of the third line is very low. As figure 5.10 points out also the signal to noise ratio of the first line is quite low. For comparison the figure shows the CARMENES spectrum, too. This observing run will be discussed in the following paragraph. It clearly shows that the S/N ratio of the CARMENES spectrograph is substantially higher in the relevant wavelength region. The result of this light curve is completely different. No indications of additional absorption during planetary transit or systematic patterns in the pre-transit data can be found as figure 5.10 and table 5.8 point out. Within the error bars both pre-transit and in-transit absorption are identical. Interestingly, the error bars are as larger as later the data was observed. This probably reflects the zenith distance of KELT-7 during the course of the observing run. At the end of the observing run the airmass increased to its maximal value of 1.72.

Table 5.8: Variation of stellar activity and planetary absorption before, during and after the planetary transit. The first row gives the observing run: E16 stands for the 2016 observing run and C18 denotes the 2018 observation. The integrated flux I is given in mÅ. In the case of Hβ the first value gives I if ALL in-transit data points are included. The second value gives I if the flagged data points are excluded.

observation	E16	E16	E16	C18	C18
band	Hα	Hβ	CaII IRT	Hα	CaII IRT
pre-transit	1855.4±3.6	1995.5±7.7	2417±24	1870.5±6.6	2395.6± 3.5
in-transit	1839.2±2.6	1988±11 resp. 2003.8±3.4	2441±25	1869.8±9.4	2394.9± 4.7
post-transit	N/A	N/A	N/A	1869.8±9.4	2389.7± 3.8

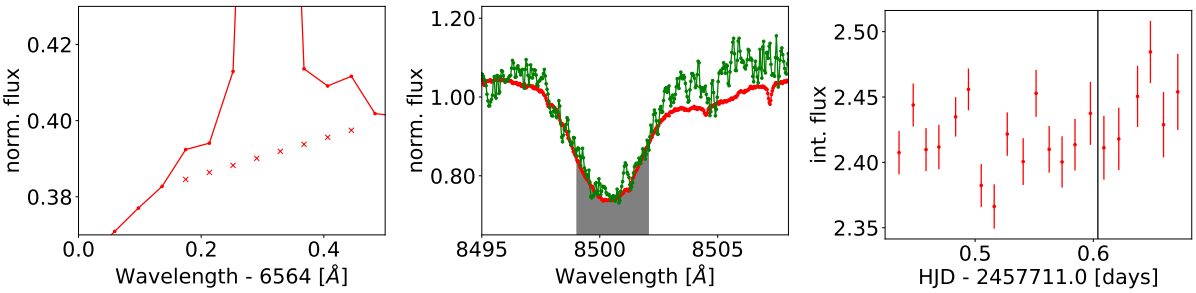

Figure 5.10: Left: the same spectrum as shown in figure 5.7 but zoomed in into the region of the cosmic. The crosses denote the replaced data points. Middle: Telluric corrected spectrum and integration band from 8499Å to 8502Å around the first CaII IRT line. The green line is the ESPERO spectrum and the red line shows the CARMENES data points. Right: Same as figure 5.6 but for the first CaII IRT line.

5.5.2 2018 Observation

Because of the doubtful situation discussed in the last section I recommended to revisit KELT-7 b with another instrument. On December 3rd 2018 another transit of KELT-7b was observed (P.I. Czesla). This time the observations were carried out at the CARMENES spectrograph. I employ the same integration bands as for the former observation. Also the telluric correction bands are almost identical. The only difference is an additional H_2O band located at 900nm (cf. table 5.8). This one is not covered by the ESPERO spectrograph. Fig. 5.11 shows the Hα and the CaII IRT light curves. The Hβ wavelength range is not covered by CARMENES. In contrast to the last observing run in 2016 no absorption seems to be present during the Hα transit. Within the statistical uncertainities the I values in all integration bands are temporally constant (see table 5.8). However, according to visual inspection the pre-transit data points are lower by about 5mÅ compared to the first half of the transit. After the first half, the data points go back to the level of the pre-transit values. Such an anomaly might be explained by stellar activity: during the first half of the transit the planet blocks part of the surface that is in active state. These regions are comparatively bright in Hα light. In contrast, the brightness of the adjacent continuum is roughly equal over the whole stellar disk. For this reason the brightness of the adjacent continuum decreases by R_{Planet}/R_{Star}. This is not true in the Hα light. Here, the brightness decreases by a larger factor. This implies that the line depth decreases and thus I increases. In contrast, the CaII IRT I value does not show this behaviour so prominently. In this light curve, the first half of the in-transit data points shows higher values, too. In contrast, all data points are overlaid by a decrease not present in the Hα light curve. Therefore, a reliable distinction between activity-induced variations and general trend is impossible.

5.5.3 Comparison of both Observing Runs

A comparison between this observing run and the 2016 data reveals that the CaII IRT I value of the latter is lower by 2.2%, i.e. the IRT line is slightly filled up in the 2018 data set. As discussed e.g. in Martin et al. 2017 a plausible explanation is a higher stellar activity during the 2018 visit. However, it is questionable if this small difference is indeed an intrinsic stellar variability or if it is merely an instrumental effect. Bringing together observations from different instruments is all but trivial. For every

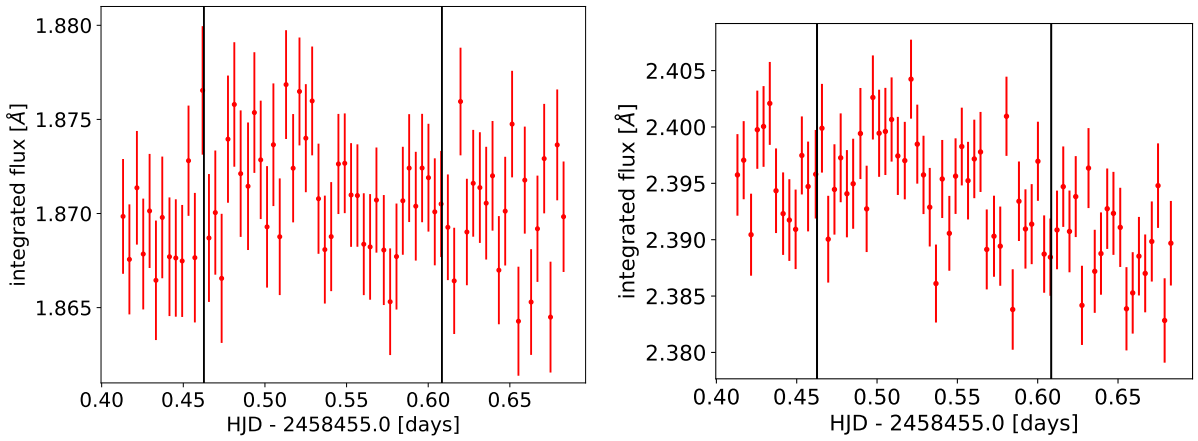

Figure 5.11: Integral versus time for the Hα line (left) and the first CaII IRT line (right). Transit observed on December 3rd 2018 with CARMENES. The solid lines denote the first and forth contact.

instrument an individual data reduction pipeline has to be used. When dealing with small variations a large number of instrumental effects is involved. These are often treated inhomogeneously by different software packages. Similar problems might also limit the comparability of the KELT-7 observations. For this reason I advocate not to overinterpret the CaII IRT differences between 2016 and 2018. In the case of the Hα observations the differences in I during pre-transit are on a comparable level, probably for the same reasons. Transit observations do not require knowledge of I on an absolute level but rather over the course of a night. Therefore, I do not discuss these offsets between the data sets. For the in-transit data points the situation is completely different. Here, the Hα data of the 2016 and 2018 observations strongly disagree. While the 2016 data clearly shows the transit in Hα this is not true for the 2018 data. Here, the light curve is more or less constant. As outlined before, KELT-7 is most likely not part of a multiple system. Therefore, this discrepancy cannot be caused by a stellar companion. Another explanation is that the stellar surface was extremely inhomogeneous during the 2016 observation. While the transit path was extremely bright due to faculae the remaining disk was significantly darker. Because the transiting planet occults these parts the Hα transit seems to be extremely deep. On the other hand, in 2018 the stellar disk was much more homogeneous. Probably, KELT-7 was in an activity minimum during this observation and thus the number and size of blemishes on the stellar surface was significantly lower. This implies that the relative dimming in Hα and in the adjacent continuum were identical and thus the Hα light curve is unaffected by the transit. A similar phenomenon has also been observed for transit light curves of HD 189733 b (Bourrier et al. 2020). While no Lyα transit was detected in a 2010 visit subsequent visits between 2011 and 2013 did show a Lyα transit. In (Bourrier et al. 2020) the authors speculate that this phenomenon is related to stellar activity. The same seems to be plausible also in this case. Also instrumental problems of unknown nature have to be considered. To shed light on this issue it would have been insightful to study the post-transit part of the 2016 light curve. This part could not be covered due to sunrise shortly after the last data point was taken. Therefore, the difference between these light cures remains enigmatic.

5.6 KELT-20 b

As discussed in the previous sections stellar activity can in principle hinder a clear identification of planetary absorption features. The best way to circumvent this nuisance is to avoid stars with chromospheric activity. For stars with effective temperatures above ≈8250K the convection zone thins out and finally vanishes (Fossati et al. 2018). This implies that hot stars are lacking chromospheres and coronae and consequently the stellar spectrum is free of chromospheric contamination. If the KELT-20 system does not have a stellar companion, it is easier to detect planetary signatures inside the stellar absorption lines. Especially the Hα line will give a clearer signal due the the absence of stellar activity jitter.
It's quite likely that this object has no companions: Mason et al. 2001 do not list any information about this target as of March 2021. Because of its brightness it is reasonable to assume that searches have been made. However, these have probably not been published due to a lack of companions. The assumption of an undisturbed planetary system is further strengthened by the fact that Oelkers et al. 2018 reports

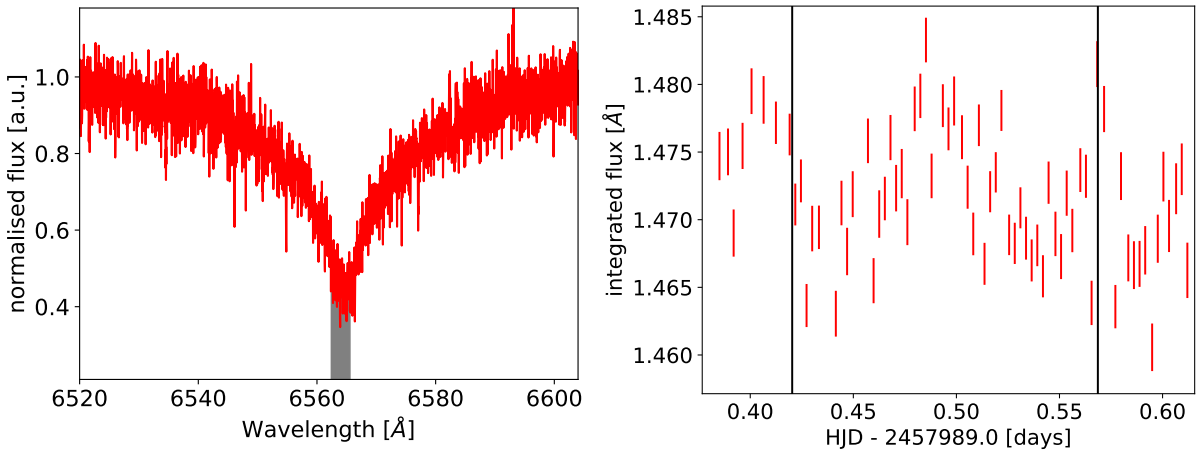

Figure 5.12: Left: Integration band around the Hα line from 6563.02Å to 6566.16Å. Due to the high stellar rotation velocity the stellar Hα line is extremely broad. Right: CARMENES Hα light curve of a KELT-20 b transit. During pre-transit 5 data points that suffer from a low signal-to-noise ratio have been excluded.

a variability below a detection threshold of 0.011 mag.
For these reasons a transit of the early-type main sequence host KELT-20 is included. In addition to the probable absence of activity also its brightness is advantageous. It allows observations with high S/N ratio and high spectral resolution in parallel. While its exact temperature is in dispute (cf. table 5.9) it is certainly by far the hottest host star considered in this work. Not only the star has a high equilibrium temperature but also the planet has. Due to its proximity to its host star the stellar wind density will be high at the planet's orbital distance. This planet has been announced twice. First by Talens et al. 2018 and shortly afterwards by Lund et al. 2017. While the publications give slightly different values for stellar and planetary parameters they usually agree within their error bars. Observations of this target have been carried out by CARMENES on August 23rd 2017. Because spectral resolution and wavelength coverage a fixed for this instrument I employ the same wavelength regions for telluric absorption correction that I also chose for the correction of the 2018 observation of KELT-7 b.

The Hα light curve

Fig. 5.12 shows the Hα light curve. The most notable feature is the W-shaped structure that is not present in any other light curve discussed previously. It is most likely caused by center-to-limb variation as discussed in section 4.4. Its shape strongly resembles both the CAII H&K and the NaD light curves discussed in Czesla et al. 2015. This implies that the width of the Hα line is narrow for the limb spectrum and broad for the central spectrum. The transit itself is not discussed in this work because this has been done earlier by Casasayas-Barris et al. 2019. In contrast to the transit itself, no strong absorption features related to the pre-transit can be found. Visual inspection shows that the first four data points are lower than the remaining four points. For the first four data points we find 1.474±0.003mÅ and for the latter the value is 1.478±0.001mÅ. While the integrated flux in the Hα line is 1.476±0.003Å during pre-transit it is 1.469±0.004Å during post-transit. This difference is considerably lower than the value of 13mÅ given in Cauley et al. 2015 which implies that KELT-20 b's bow shock must be significantly shallower, if existent. A major source for doubt is that the temporal evolution before HJD=2457989.38 is unknown. If the I values were higher before this instant, this would be a hint for a bow shock.

5.7 Summary & Comparison to Literature

As detailed in the preceding sections no indications of planetary pre-transit absorption features could be identified. Temporal variations in light curves could always be explained by instrumental artifacts, stellar activity variations or spectroscopic phenomena related to the passage of the planetary disk in front of its host star. This is in line with the results of other authors. For instance Cauley et al. 2017b obtained Hα time series for transit observations of KELT-3 b and GJ 436 b. None of these observations showed any evidence for pre-transit absorption features. The same is also true for KELT-9 b. This object

Table 5.9: Properties of KELT-20 b and its host star. For T_{eff} the literature gives different values. While the former is from Lund et al. 2017 the latter comes from Talens et al. 2018. In the case of the planetary density I took the value from Lund et al. 2017 and used Park 2020 to convert it to the value given in the table.

Parameter	Value	Ref.
	KELT-20	
m_V	7.58	Wenger et al. 2000
$M_B - M_V$	0.09	Wenger et al. 2000
Spectral Type	*A2*	Talens et al. 2018
T_{eff}[K]	8720 resp. 8980^{+90}_{-130}	see caption
$\log(g)$	4.31 ± 0.02	Talens et al. 2018
$[M/H]$	-0.02 ± 0.07	Talens et al. 2018
$v_{\rm rot}\sin(i)$[km/s]	117 ± 3	Talens et al. 2018
$v_{\rm rad}$[km/s]	-21.07 ± 0.03	Talens et al. 2018
Distance [pc]	136.4 ± 0.8	Bailer-Jones et al. 2018
age [Myr]	200^{+100}_{-50}	Talens et al. 2018
Mass [$M_\odot$]	$1.89^{+0.06}_{-0.05}$	Talens et al. 2018
Radius [$R_\odot$]	1.60 ± 0.06	Talens et al. 2018
	KELT-20 b	
Planet mass [M_{Jup}]	< 3.382	Lund et al. 2017
Semi-major Axis [AU]	0.057 ± 0.006	Talens et al. 2018
Eccentricity	0	Talens et al. 2018
Orbital period [d]	$3.474119^{+0.000005}_{-0.000006}$	Talens et al. 2018
Planetary radius [R_{Jup}]	1.83 ± 0.07	Talens et al. 2018
Duration of transit [h]	3.55 ± 0.03	Talens et al. 2018
Transit depth [%]	1.32 ± 0.02	Talens et al. 2018
Planetary density [ρ_{Jup}]	< 0.608	see caption
Equilibrium temperature[K]	2260 ± 50	Talens et al. 2018
Exposure Time[s]	192	This work.

has been announced in June 2017 (Yan and Henning 2018). An interesting aspect is the outstanding high planetary temperature of ≈4600K[3] and high density of its stellar wind due to its extremely close orbit of 0.03462AU. Another advantage of this object is its host star of spectral type between B9.5 and A0. This implies that stellar activity cannot contaminate observations. In Yan and Henning 2018 the authors analysed spectroscopic follow-up transit observations. These were carried out on August 6th and September 21st 2017 with the CARMENES spectrograph. Because of the apparent V band brightness of 7.5 mag the authors could impose strict limits on pre-transit absorption. This observation rules out pre-transit absorption depths higher than ≈3mÅ but clearly shows an in-transit absorption as deep as ≈15mÅ.

In contrast to the aforementioned results, Jensen et al. 2018 present a light curve that shows strong pre- and post-transit Hα absorption in the WASP-12 system. Interestingly, the Hβ light curve does not show compatible absorption features. Therefore, an astrophysical interpretation is challenging.

[3] According to Ciardi 2020 KELT-9b is still the planet with the highest equilibrium temperature (as of January 2021).

Chapter 6

Implications for Planetary Magnetic Fields

The results of the last chapter have shown that no convincing pre-transit hydrogen absorption signals could be found. This is in contrast with the expectations of Llama et al. 2013 and Cauley et al. 2015. They expect that the planet interacts with the stellar wind which results in the formation of a bow shock. This interaction produces excited hydrogen in the upper planetary atmosphere. These excited atoms then act as absorbers in the Balmer lines. To explain the absence of this absorption a viable assumption is the lack of a planetary atmosphere. In this scenario the planet has already lost its atmosphere due to Jeans escape or due to energy-limited escape. In this scenario no interaction between planetary atmosphere and stellar wind is possible. As Salz et al. 2016b point out the escape rate for the former is quite small and thus the latter dominates. Even the energy-limited escape does not predict an evaporation of the planetary atmosphere within a few gigayears. For a wide variety of extrasolar planets Salz et al. 2016b never found mass loss rates higher than $10^{12}\mathrm{g/s}^{-1}$. For instance, they find a mass loss rate of $4.1{\cdot}10^{9}\mathrm{g/s}^{-1}$ for HD 189733 b. This corresponds to a total fractional mass loss of 0.1 per mille per gigayear and thus the mass loss since planetary formation is negligible. An important point is that radiative cooling of the planetary atmosphere dissipates the thermal energy and thereby inhibits the evaporation process. This is in line with the results derived by Kubyshkina et al. 2018 and references mentioned therein. Interestingly, they find that even planets like HD 149026 b do not have an excessive high mass loss rate. For this object they find a mass loss rate of $\approx 3 \cdot 10^{10}\mathrm{g/s}^{-1}$. This object has a mass of $0.36 M_{Jup}$ and an effective temperature of 1634K (Ciardi 2020). Both its mass and its equilibrium temperature are higher than the values of WASP-69 b. For this reason I regard HD 149026 b as a worst-case estimate for planetary mass loss of WASP-69 b.
It is probable that all planets regarded in this work still have a hydrogen atmosphere and thus that an interaction between stellar wind and planetary atmosphere takes place. One important consequence is that the distance of the planetary bow shock from the planet's center depends on the strength of its magnetic field. Neither the interplanetary environment of extrasolar planetary systems nor the topology of exoplanet's $\vec{B}$ fields are known. For these reasons I make the following simplyfing assumptions that will be justified in the following paragraphs:

- the planet's $\vec{B}$ field is purely dipolar
- the stellar wind is completely isotropic and radial
- The planet's orbit is a circle and therefore the orbital velocity u_k is constant.

Magnetic Field Topology

Connerney et al. 2018 show that Jupiter's magnetic field is approximately dipolar, albeit measurements by the Juno spacecraft revealed slight deviations. Such data are not available for extrasolar planets. For this reason I assume that their magnetic fields are purely dipolar. Under this assuption, the polar magnetic field can be estimated by equation 4 as given in Cauley et al. 2015:

$$B_P = 2 \left(\frac{r_m}{R_P} \right)^3 \sqrt{2\mu_0 \left(\rho_W \left(r \right) \Delta u_W^2 + P_W \right) + \vec{B_\star}^{\,2}} \tag{6.1}$$

with the following ingredients:

- r_M: standoff distance between planet and bow shock
- R_P: planetary radius
- μ_0: vacuum magnetic permeability
- ρ_W: density of the stellar wind
- Δu_W: relative velocity between stellar wind and planetary motion
- P_W: thermal pressure of the wind
- $\vec{B_\star}$: stellar magnetic field strength at the planet's position

Finally, B_P is related to the equatorial magnetic field by $B_{eq}=\frac{1}{2}B_P$. As outlined in Cauley et al. 2015 and Llama et al. 2013 this equation describes a pressure balance between the stellar wind and its magnetic field. More precisely, equation 6.1 neglects contributions by the thermal pressure of the planet as well as pressure terms induced by the planetary atmosphere and its wind.
Before this equation can be used to derive planetary magnetic fields the stellar wind parameters have to be estimated. In the case of the sun this is rather trivial because they can be measured in-situ. In contrast, this is not possible for distant stars. They have to be derived by stellar wind models. Different models have to be used depending on the stellar temperature. In the course of this chapter I first discuss the stellar wind models for cool stars and its ingredients in sections 6.1 to 6.2.2. The model for hot stars follows in section 6.3. In section 6.4 I discuss the estimation of the stellar magnetic field strength.
To assess if the planetary magnetic fields obtained by this method are plausible I compare them to the magnetic field that would be produced by a slowed-down version of Jupiter in section 6.5. Bow shocks can only be formed if the relative speed between stellar wind and planet is supersonic. This I discuss in section 6.6. The last ingredient is the standoff distance between planet and bow shock. An estimate for it can be found in section 6.7. Finally, I put all ingredients together in section 6.8 and derive an estimate of the planetary magnetic field.

6.1 Stellar Wind Model for Cool Stars

As pointed out in Foukal 2013 the direction of the solar wind is predominantly radial, i.e. $u_r \gg u_\phi$. Therefore, I assume that u_ϕ as defined in equation 4.2 equals zero.
While a direct measurement of the properties of stellar wind parameters is virtually impossible I assume that the model given in Johnstone et al. 2015 is an appropriate description of the interplanetary environment around low-mass main-sequence stars. For hot stars such as KELT-20 this model cannot be employed. Therefore, its wind will be described later in section 6.3. Below I summarise the steps to estimate stellar wind parameters from quantities that can be measured for distant stars. These parameters are needed to calculate the planetary $\vec{B}$ field in equation 6.1. The following text summarizes the most important steps to derive stellar wind parameters. A more detailed explanation of the steps and a derivation of the stellar wind model can be found in Johnstone et al. 2015. First we derive the coronal temperature:

$$T_{cor} \approx 0.11 F_X^{0.26} \tag{6.2}$$

The derivation of the stellar X-ray flux F_X will be discussed in section 6.2. The wind temperature is now $T_0 = 0.75 T_{cor}$ for the slow wind and $T_0 = 1.58 T_{cor}$ for the fast wind. In-situ measurements by spaceprobes clearly showed that the slow wind dominates the interplanetary medium at low ecliptic latitudes (Foukal 2013). Here, the proton density of the slow wind is on average three times higher than that of the fast wind. I assume that these findings are true for all cool stars regarded in this work. Therefore, I only consider the slow wind.
For slowly rotating stars the stellar wind speed at distance r is approximately given by

$$v(r) = v_{1AU} + (r - r_{1AU}) \frac{dv}{dr} \tag{6.3}$$

where

$$v_{1AU} = 73.39 + 224.14 T_0 - 11.28 T_0^2 + 0.28 T_0^3 \tag{6.4}$$

and

$$\frac{dv}{dr} = 0.19 + 0.066 T_0 - 0.0035 T_0^2 + 9.97 \cdot 10^{-5} T_0^3 \tag{6.5}$$

According to Johnstone et al. 2015 the transition between "slow" and "fast" depends on the stellar mass. For solar-mass stars the transition is at ≈15 times the solar rotation rate $\Omega_\odot$. This value increases with decreasing stellar mass. At $0.4M_\odot$ is raises to $\approx 110\Omega_\odot$. In the case of rapidly rotating stars equation 6.3 cannot be used. Instead, the Michel velocity must be used:

$$v(r) = \sqrt[3]{\frac{r^4 B(r)_\star^2 \Omega_\star^2}{\dot{M}_\star}} \tag{6.6}$$

where $B(r)_\star^2$ is the stellar $\vec{B}$ field at radius r, $\Omega_\star$ is the stellar rotation rate and $\dot{M}_\star$ is the stellar mass loss rate. It can be calculated from

$$\dot{M}_\star = \dot{M}_\odot R_\star^2 \Omega_\star^{1.33} M_\star^{-3.36} \tag{6.7}$$

where $\dot{M}_\odot$ is the solar mass loss rate, $R_\star$ is the stellar radius and $M_\star$ is the stellar mass. Now we can use mass loss rate and wind speed to calculate its density:

$$\rho(r) = \frac{\dot{M}_\star}{4\pi r^2 v(r)} \tag{6.8}$$

Additionally, we need the wind temperature at a distance of 1AU

$$T_{1AU} \approx 0.054 T_0 - 0.01 \tag{6.9}$$

to estimate its value at distance r:

$$T(r) = T_{1AU} \left(\frac{\rho(r)}{\rho_{1AU}} \right)^{0.51} \tag{6.10}$$

To convert $\rho(r)$ and $T(r)$ to the wind pressure $P_W(r)$ I assume that the stellar wind is an ideal gas:

$$P_W(r) = \rho(r) \frac{\mathcal{R}}{\mathcal{M}} T(r) \tag{6.11}$$

where $\mathcal{R}$ and $\mathcal{M}$ are the ideal gas constant resp. the molar mass of a proton gas.

Relative Wind Velocity

For circular orbits, the planetary velocity is simply

$$v_{Kep} = \sqrt{\frac{GM_\odot \cdot M_\star}{r}} \tag{6.12}$$

Both the planet itself and the stellar wind are moving. When we investigate the collision between both components we have to determine the relative motion between them. Because the direction of the stellar wind is approximately perpendicular to the direction of the planetary motion in this model the relative velocity Δu_W is given by

$$\Delta u_W = \sqrt{v_{Kep}^2 + v(r)^2} \tag{6.13}$$

6.2 X-ray luminosity of planet hosts

The majority of planet hosts is such far away that their X-ray fluxes have not yet been detected. Certainly, this situation will improve during the next years when the results of the eRosita mission will become available and public (Robrade 2016). However, this is not very helpful when such data is needed now and not in the coming years. To circument this situation I extract the chromospheric emission from the CaII H&K lines and calculate the Mount Wilson S index S_{MWO}.

From instrumental values to the S index

A conversion procedure for UVES observations is given in Melo et al. 2006. Here I only summarize the most important steps. First, a chromospheric flux indicator S_{US} is defined:

$$S_{US} := (F_H + F_K)/(C_H + C_K). \tag{6.14}$$

F_H resp. F_K are the fluxes in 1Å boxes centered on the CaII H&K line cores. C_H resp. C_K denote the fluxes in nearby 20Å continuum bands. To link S_{US} to S_{MWO} a sample of stars observed with both instruments is needed. From this sample the authors derive

$$S_{MWO} = (S_{US} + 0.00341)\,/0.06111. \tag{6.15}$$

A similar conversion procedure also exists for the TIGRE spectrograph. In Mittag et al. 2016 the authors find that the instrumental S_{TIGRE} index can be converted to S_{MWO} with the linear relation

$$S_{MWO} = (20.02 \pm 0.42)\, S_{TIGRE} + (0.0360 \pm 0.0029)\,. \tag{6.16}$$

According to these procedures I convert the fluxes inside the CaII H&K lines to S_{MWO}.

From S index to X-ray luminosity

S_{MWO} can now be converted to stellar X-rax fluxes as outlined in Hempelmann et al. 1996. First, we have to transform the median of S_{MWO} during an observation campaign to stellar surface flux density F_{CaII}. The advantage of the median in comparison to the mean is that especially the flare during the transit of WASP-69b is naturally rejected. The conversion is given in Rutten 1984:

$$F_{CaII} = 1.29 \cdot 10^{-8} \cdot S_{MWO} C_{cf} T_{eff}^4 \tag{6.17}$$

with stellar effective temperature T_{eff} and

$$\log(C_{cf}) = 0.25(B-V)^3 - 1.33(B-V)^2 + 0.43(B-V) + 0.24 \tag{6.18}$$

for main-sequence stars with $0.3 \leqslant B-V \leqslant 1.6$. Now we have to estimate the excess flux $\Delta F_{CaII} = F_{CaII} - F_{min}$. In Hempelmann et al. 1996 we find that F_{min} is given by

$$\log F_{min} = \begin{cases} 8.07 - 3.11(B-V) & 0.40 < (B-V) < 0.51 \\ 6.48 & 0.51 \leqslant (B-V) \leqslant 0.59 \\ 6.95 + 0.36(B-V) - 1.95(B-V)^2 & (B-V) > 0.59 \end{cases} \tag{6.19}$$

where $B-V$ denotes the color. Finally, the X-ray flux is given by

$$\log(F_X) = a + b \cdot \log(\Delta F_{CaII}) \tag{6.20}$$

where $a_1 = -1.7$ and $b_1 = 1.2$ for $\log(\Delta F_{CaII}) \lesssim 6.25$ resp. $a_2 = -19$ and $b_2 = 4$ above this limit.

6.2.1 Conversion of CaII IRT to CaII H&K flux

As outlined in the previous section the chromospheric CaII H&K emission can be converted to X-ray flux. Unfortunately, measurements in this spectral region are not available for all targets. In the case of the 2016 observations of KELT-7 this is due to the fact that the ESPERO spectrograph is optimised for the red wavelength range and thus not sensitive enough in the violet part of the spectrum. In the case of the 2018 observations this wavelength region is not available because the CARMENES spectrograph does not cover it. To overcome this situation, I used the Calcium infrared triplet lines. Analogous to the CaII H&K lines also these lines are a well suited indicator for chromospheric activity. In contrast to the CaII H&K lines stellar activity will not lead to emission cores inside the CaII H&K lines but activity will fill up the lines so that high stellar activity implies shallow CaII IRT lines. A straightforward conversion between stellar line depth and chromospheric activity is not possible because the depth of a stellar line not only depends on its activity but also on stellar parameters. Therefore, a simple ratio comparing the flux inside a line core to a continuum band cannot be used as an activity indicator. Instead, it is necessary to subtract a stellar template spectrum from the observation in question. To keep only chromospheric emission but remove virtually all photospheric contribution the template should

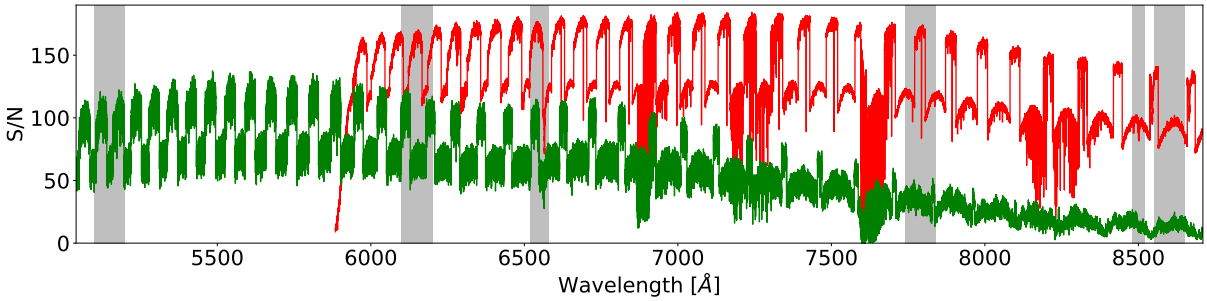

Figure 6.1: S/N for typical CARMENES(red) and ESPERO(green) spectra. The gray bands denote the regions where the fit is performed in.

have similar stellar parameters but being in a state of low stellar activity. Because of spectral differences between the sun and other stars it is quite hard to judge when a star is at its lowest possible activity state. To circument this problem a promising alternative are synthetic stellar spectra. These are produced by computer programs and contain by construction only the spectrum of the stellar photsphere. In other words, these spectra are completely free from stellar activity. However, the numerical results might not be free from systematic deviations between observed inactive and synthetic stellar spectra. For instance, a discrepancy in the depth of the modeled CaII IRT line leads to a systematic error in the determination of the chromospheric activity level. Another source of error is the accuracy of stellar parameters. If these are given incorrectly also the CaII IRT line depth is inevitably affected. I do not need an overwhelmingly precise value of the chromospheric flux but rather a reasonable estimate of F_X and in the end an approximation of the stellar wind parameters. Therefore, I do not investigate the above-mentioned issues in detail but assume that the synthetic models are correct for this purpose.
After subtraction of the quiescent spectrum the remaining flux inside a 1 Å band centered on the CaII IRT line in question is integrated. This equivalent-width has to be converted to a physical flux value on the stellar surface in erg/s/cm^2. A conversion from the normalised continuum to stellar surface flux is given in Hall 1996. The continuum flux in the region around the CaII IRT lines $\mathscr{F}_{c,\lambda 8520}$ in erg/s/cm^2/Å is given by

$$\log \mathscr{F}_{c,\lambda 8520} = \alpha + \beta(B-V) \tag{6.21}$$

with coefficients α and β given in their table 4. With this result we can now convert the relative flux excess $F_{Exc,IRT}$ into absolute physical units. According to Martin et al. 2017 the chromospheric excess flux in CaII IRT is proportional to the excess in CaII H&K. For F, G and K main-sequence stars with $0.4 \lesssim B-V \lesssim 1.0$ the conversions are given by

$$\Delta F_{CaII} = 10^{1.095-0.587(B-V)} F_{Exc,IRT\lambda 8498} \tag{6.22}$$

$$\Delta F_{CaII} = 10^{1.036-0.631(B-V)} F_{Exc,IRT\lambda 8542} \tag{6.23}$$

$$\Delta F_{CaII} = 10^{1.137-0.663(B-V)} F_{Exc,IRT\lambda 8662} \tag{6.24}$$

where the number in subscript denotes the respective wavelength of the line in Å and the fluxes are in erg/s/cm^2. In Martin et al. 2017 ΔF_{CaII} is denoted $F_{Exc,HK}$. Now I use equation 6.20 to obtain $\log(F_X)$.

.. for KELT-7

As discussed in section 5.5.3 the temporal variability of KELT-7's spectrum is rather low. This implies that also the stellar activity can be regarded as constant between 2016 and 2018. Therefore, I first produce a master spectrum with high S/N ratio from all individual observations. To do this I calculated a weighted average spectrum. The weight is given by the S/N ratio. As figure 6.1 shows the S/N ratio of the CARMENES spectra is superior for wavelengths above 6000Å. For the master spectrum I used only ESPERO data for wavelengths below 6000Å and solely CARMENES data above this limit. For lower wavelength no choice can be made and for higher wavelength the contribution of the CARMENES spectra is more important. This procedure avoids artifacts that could be introduced by adding up spectra from different instruments. This master spectrum I compare to `PHOENIX` model spectra to derive the stellar parameters. More precisely, I do not perform the comparison by hand but use the software that

Table 6.1: KELT-7's stellar parameters: comparison between literature values and values derived by fitting procedure. In the case of T_{eff} the literature offers in total three values of which the minimum and maximum are given here.
References. B15: Bieryla et al. 2015; S10: Soubiran et al. 2010.

Quantity	T_{eff}[K]	$\log(g)$	$[M/H]$	$v \sin(i)$[km/s]
Literature	6761±74 S10(min.) 6789^{+50}_{-49} B15(max.)	4.149±0.019 B15	$0.139^{+0.075}_{-0.081}$ B15	$65.0^{+6.0}_{-5.9}$ B15
Fitted	6771	4.039	0.034	73.6

was written by my former colleague Johannes Martin. It is described in detail in Martin 2018. Here I only summarise the most important points. To begin with the software needs the stellar spectrum, a grid of `PHOENIX` model atmospheres and initial values for the stellar parameters. The grid comes with the software package. Because KELT-7 is not an overwhelmingly bright target the information about its stellar parameters is sparse. As presented in table 6.1 only a single value is available for most parameters. From the stellar parameters and the grid the software calculates an initial model spectrum for certain wavelength ranges. As pointed out in Martin 2018 it is not reasonable to use the whole stellar spectrum. Instead, selected regions should be used. These are given in table 6.1 of Martin 2018 and marked by gray bands in figure 6.1. In some of these wavelength ranges small parts have to be excluded to avoid contaminations by chromospheric lines. Examples are the Hα line and the CaII IRT lines.

The next step is the actual fitting process. The code now uses the Markov Chain Monte Carlo method to find the "best" stellar parameters, i.e. the model for which the χ^2 value is minimal. The results of this procedure are also given in table 6.1. Interestingly, the effective temperature is between the literature estimates and well below the reported error bars. Because I cannot identify an obvious reason for this behaviour I regard this as a coincidence. In contrast, the other quantities are not so close to their literature values. While metallicity and rotational velocity are slightly off $\log(g)$ shows a rather large discrepancy. The dependence of stellar spectra on $\log(g)$ is rather weak. Changes in this parameter will only mildly influence the χ^2 value. Therefore, the minimisation algorithm could have been trapped by small deviations caused by inaccuracies of the stellar model.

With this "best" model it is now possible to obtain the chromospheric component. After subtraction of the model from the observed master spectrum and integration of the flux in the first CaII IRT line located at 8489Å we find an equivalent width of 70.0mÅ. This value has to be converted to stellar surface flux. From equation 6.21 we obtain $6.1 \cdot 10^6 \mathrm{erg/s/cm^2/Å}$ with $\alpha = 7.083$ and $\beta = -0.685$. With the excess equivalent-width this gives $F_{Exc,IRT\lambda 8498} = 4.3 \cdot 10^5 \mathrm{erg/cm^2/s}$.

6.2.2 X-ray luminosity values

In the case of WASP-69b and WASP-131b the derivation of the X-ray flux F_X is straightforward: both transits have been observed with the UVES spectrograph which was used in a configuration so that the CaII H&K wavelength region was covered. Therefore, I first derived S_{US}, converted it to S_{MWO}, took its median $\tilde{S}_{MWO}$ and finally derived F_X. In the case of HD 189733 the derivation of F_X is also straightforward and in principle identical. Instead of equation 6.15 equation 6.16 has to be employed. Theoretically, it could also have been derived from the $F_{Exc,IRT\lambda 8498}$ value. As shown in figure 1 of Kohl et al. 2018 the equivalent width of CaII H&K ranges between 197Å and 398Å. Correspondingly, also S_{MWO} varies between 0.46 and 0.62 with a median of 0.55. Although S_{MWO} fluctuates considerably the consequences for the stellar wind are far less critical as equation 6.2 points out. Because of this I do not expect that a derivation from $F_{Exc,IRT\lambda 8498}$ would have given an F_X value of superior quality justifying the effort of a more complex conversion procedure. In contrast, I think that this approach would give a result of slightly inferior quality. It requires an additional step, namely the conversion from CaII IRT to CaII H&K. Martin et al. 2017 and Martin 2018 show that their conversion relations are pretty tight. Nevertheless, the conversion introduces small systematic errors. This procedure could also have been applied to the WASP-69 observation but for the aforesaid reasons I waived this.

In contrast, for KELT-7 no simultaneous CaII H&K observations exist. For this reason I had to use the CaII IRT emission to derive ΔF_{CaII} and eventually the X-ray luminosity.

Table 6.2 lists the chromospheric activity as derived from the observations and the X-ray luminosity that I obtained by application of the aforementioned equations. As outlined in section 6.3 no X-ray

luminosity is required to obtain the stellar wind of KELT-20. It therefore has not been calculated.

Table 6.2: Chromospheric emission and derived X-ray fluxes of planet hosts. N/A denotes that the quantity could not be derived because the relevant spectral range is not covered by the instrument's configuration. For HD 189733 median values are given.

Planet	$F_{Exc,IRT\lambda 8498}$[erg/cm^2/s]	$\tilde{S}_{MWO}$	ΔF_{CaII}[erg/cm^2/s]	F_X[erg/cm^2/s]
WASP-131b	N/A	0.151	$1.7 \cdot 10^5$	$3.7 \cdot 10^4$
WASP-69b	See text.	0.571	$1.0 \cdot 10^6$	$3.2 \cdot 10^5$
KELT-7b	$4.3 \cdot 10^5$	N/A	$3.0 \cdot 10^6$	$8.1 \cdot 10^6$
HD 189733 b	See text.	0.55	$1.9 \cdot 10^6$	$1.2 \cdot 10^6$

6.3 Stellar wind around KELT-20

In comparison to the other planet hosts KELT-20 is substantially hotter and more massive. Therefore, the model given in Johnstone et al. 2015 will not be appropriate for this star. As can be seen from table 6.3 KELT-20 and Sirius A have approximately similar stellar parameters. For this reason, I assume that

Table 6.3: Comparison of stellar parameters between KELT-20, Sirius A and Vega. Parameters of Sirius A are taken from Boyajian et al. 2013 and parameters of Vega are taken according to the last column.

Parameter	KELT-20	Sirius A	Vega	Ref.
T_{eff}	$8980\ ^{+90}_{-130}$	9711 ± 23	9550 ± 125	Royer et al. 2014
Mass [$M_\odot$]	$1.89\ ^{+0.06}_{-0.05}$	2.282 ± 0.001	2.3 ± 0.2	Aufdenberg et al. 2006
Radius [$R_\odot$]	1.60 ± 0.06	1.7074 ± 0.0124	2.78 ± 0.02	Aufdenberg et al. 2006
Luminosity [$L_\odot$]	$12.7\ ^{+2.2}_{-1.9}$	23.3533 ± 0.1946	37 ± 3	Aufdenberg et al. 2006

the stellar wind is similar to the one around Sirius A as given in Bertin et al. 1995. In this work the authors conclude that the stellar wind velocity at infinite distance from the star is 1,300km/s. I use their equation 1 to convert it to the velocity found at the orbital distance of KELT-20b:

$$v\left(r\right) = v_\infty \left(1 - \frac{R_\star}{r}\right)^\beta \tag{6.25}$$

and equation 6.8 to obtain $\rho\left(r\right)$ with the mass loss rate of $\dot{M}_\star = 1.5 \cdot 10^{-12}$ (Bertin et al. 1995). Furthermore, the authors conclude that the stellar wind temperature is 7,000K.

6.4 Stellar Magnetic Fields

The last ingredient we need to calculate the planetary magnetic field B_P is the stellar magnetic field strength. In the case of HD 189733 the surface field configuration has been determined by Llama et al. 2013 and calculated at the orbital distance of HD 189733. Due to the fact that stellar $\vec{B}$ fields are both temporally variable and not axially symmetric the value given in Llama et al. 2013 can only be a crude estimate for the field at the location of the planet. For most other stars the detailed magnetic field configuration is unknown. Only a mean value averaged over the whole surface is known. A detailed reconstruction of the magnetic field topology by Zeeman-Doppler imaging requires polarimetric observations (Vidotto et al. 2014). These are not available for the stars of interest. To overcome this situation, I took magnetic field measurements performed for stars of similar spectral type. For instance, Petit et al. 2010 gives the field of Vega. This star I use as a surrogate for KELT-20. For the remaining targets I adopt the values listed in Vidotto et al. 2014. The authors present a list of stellar magnetic field observations for a variety of targets. For some stars observations at different epochs are available. To take into account varying levels of stellar activity I selected the highest value for a given spectral type. In this case equation 6.1 will yield a higher and thus more conservative estimate for B_P. Additionally,

I assume that the stellar field is purely dipolar. In this case the field strength at a distance r from the host star is $B(r) \approx B_0/r^3$ where B_0 denotes the mean field on the stellar surface. The values that I adopted are given in table 6.7.

6.5 Planetary Rotation Period

In general, the rotation periods of extrasolar planets are unknown. An exception is HD 189733 b. For this object Brogi et al. 2016 find a rotation period of $1.7^{+2.9}_{-0.4}$ days which is consistent with the assumption of tidal locking. Especially for the other hot Jupiters concerned in this work the rotation period is unknown. Therefore, I determine if the tidal locking timescales are sufficient so that the planets considered in this work are already tidally locked. The time required can be estimated by equation 9 given in Gladman et al. 1996:

$$\tau_{despin} \approx \frac{\omega r^6 C Q}{3 G m_{host}^2 k_2 R_s^5} \tag{6.26}$$

with the following quantities:

- τ_{despin} tidal locking time.
- ω initial spin rate I assume that all hot Jupiters were initially rotationg as fast as Jupiter: 9h 55 min. (Seidelmann et al. 2007). Even the assumption of a spin rate ten times as fast as Jupiter will lead to a tidal locking within 100 years.
- r distance of the planet from its host star
- C moment of inertia. I assume that the planet is a homogenious sphere. Therefore $C = 0.4 m_p R_s^2$ (Demtröder 2018) where m_p is the planetary mass and R_s its radius.
- Q specific dissipation function of the planet. Gladman et al. 1996 suggest a value of 100 for a conservative estimate which I adopt, too.
- G gravitational constant from Mohr et al. 2016.
- m_{host} mass of the host star
- k_2 tidal Love number of the planet. I adopt a value of 0.530 as given in Ni 2018 and measured by the Juno spacecraft for Jupiter.[1]
- R_s mean radius of the planet.

Table 6.4 lists the tidal locking timescale as derived from equation 6.26: from these numbers it is obvious

Table 6.4: Tidal locking timescales for all hot Jupiters regarded in this work and for Jupiter in the solar system.

Planet name	τ_{despin} [yr]
HD 189733 b	1.5
KELT-7 b	1.5
KELT-20 b	5.4
WASP-69 b	3.8
WASP-131 b	9.2
Jupiter	$27 \cdot 10^{12}$

that we can assume that all hot Jupiters considered in this work are already tidally locked. Even if the planets migrated inwards during the late stages of formation the assuption of tidal locking is still valid. The only exeption is Jupiter in our solar system. In this case the derived tidal locking timescale is higher by orders of magnitude. In accordance with observational findings equation 6.26 shows that τ_{despin} is longer than the age of the solar system.
For a planet whose core is composed of a conductive material rotation rate and planetary magnetic field

[1] In agreement with the value determined for the hot Jupiter WASP-18Ab by Csizmadia et al. 2019: $k_2 = 0.62^{+0.55}_{-0.19}$

depend on each other. As faster the planet rotates as higher its magnetic field is. More quantitatively, equation 7.6 given in Schrijver 2010 must be fulfilled:

$$\Lambda = \frac{\sigma B^2}{2\rho\Omega} \approx 1 \tag{6.27}$$

with conductivity σ, density ρ and rotation rate Ω. According to Schrijver 2010 both theoretical considerations and magnetic field observations of Jupiter and the geodynamo validate this relation. For $\Lambda \ll 1$ magnetic field growth intensifies convection and thereby amplifying the dynamo. This in turn increases the magnetic field. If instead $\Lambda \gg 1$, the convection is weakened and the dynamo is damped. Both restrictions together favour $\Lambda \approx 1$. In this situation the magnetic field is stable. Rewriting equation 6.27 and assuming $\Lambda \approx 1$ yields

$$B = \sqrt{\frac{2\rho}{\sigma}\Omega} \tag{6.28}$$

Under the assumption of identical core compositions for Jupiter and extrasolar giant planets, also their densities and conductivities are. In this case the planetary magnetic field obeys the following scaling relation:

$$B = B_{Jup} \cdot \sqrt{\frac{P_{Jup}}{P_P}} \tag{6.29}$$

with Jupiter's rotation period P_{Jup} and planetary orbital period P_P.

6.6 Sound Speed of the Interplanetary Medium

Bow shocks can only occur in the case of supersonic motion. Therefore, it is essential that the relative velocity between upper planetary atmosphere and stellar wind is higher than the sound speed. From equation 6.8 I derive the stellar wind density ρ_W and give it in table 6.5. The sound speed can only be defined if the type of the gas is known. The most simple assumption is that of an ideal gas. It has to be taken into account that the stellar wind consists mainly of electrically charged particles. Therefore it is questionable if the stellar wind can adequately be described by the equation of state of an ideal gas. To obtain a conservative estimate of the importance of Coulomb interaction and as a simplification I assume that the stellar wind is completely charged and that it is solely composed of protons and electrons. Because $m_p \gg m_e$ I additionally assume that the electrons move faster in the ambient electric fields than the protons and group together around them. This implies that the electrons attenuate the electric charge of the protons. In this scenario the Coulomb interaction between the protons has to be included into the equation of state of the ideal gas as follows (Cap 1994):

$$p = n_p k T_p \left(1 - \frac{\sqrt{2}}{24\pi n_p \lambda_D^3}\right) \tag{6.30}$$

where p is the pressure, n_p is the number density of the protons, k is the Boltzmann constant, T_p is the temperature of the protons and λ_D is the Debye length. This length describes the effective screening of the electrostatic potential of the protons by the electrons. At a distance of λ_D the potential decreases by 1/e. This length is given by

$$\lambda_D = \sqrt{\frac{\epsilon_0 k T_p}{e^2 n_p (Z+1)}} \tag{6.31}$$

with vacuum electric permittivity ϵ_0, elementary charge e and Z=1 for singly ionized species. As table 6.5 shows the magnitude of the Coulomb correction is much lower than unity which implies that the assumption of an ideal gas is valid.
In the case of an ideal gas in a nonmagnetised environment the sound speed is given by Tipler 2015

$$c = \sqrt{\frac{\gamma k T}{m}} \tag{6.32}$$

where γ=5/3 is the adiabatic index, $T \approx T_p$ is the absolute temperature of the gas. For cool stars it is given by equation 6.10 and for hot stars I adopt a temperature of 7,000K. m is the mass of a single molecule, i.e. the mass of a hydrogen atom. In table 6.5 I present the sound speed and derive the Mach number $M = \Delta u_W / c$ with Δu_W as defined by equation 6.13. For comparison, these values are also

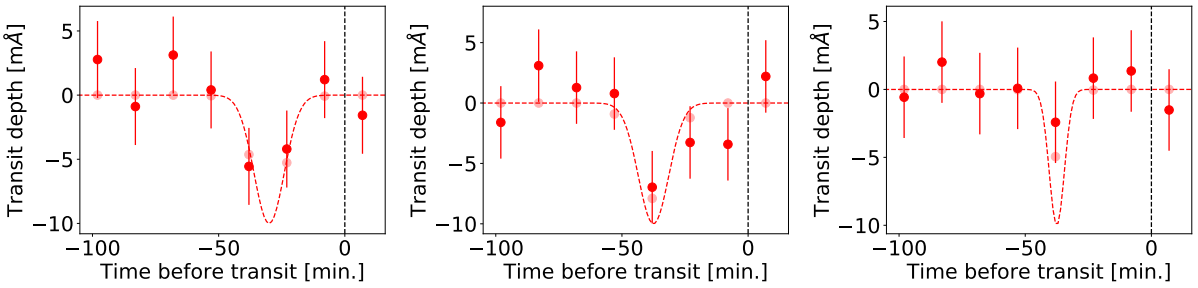

Figure 6.2: Comparison between transit light curve observed with infinite temporal resolution (dashed) to the same light curve observed with a temporal cadence of 15 minutes (data points). Semi-transparent points represent observations without any measurement error while the solid points include noise. The noise comes from the `numpy` random number generator that outputs normally distributed samples (Harris et al. 2020). The error bars represent a measurement error of ±3mÅ. In all plots the depth of the bow shock is 10mÅ. Left: The maximum is located at 30 minutes before transit and the width, i.e. the FWHM, of the bow shock is 14 minutes. Middle: Here the minimum is located at −37.5 minutes. Right: Minimum located at the same position but the FWHM is 7 minutes.

given at the position of Jupiter's orbit. In contrast to exoplanetary systems in-situ measurements from different spaceprobes are available. For example, Ebert et al. 2014 give a comprehensive list of solar wind parameters that were measured during the 23rd solar cycle by Ulysses. From their data it it obvious that the parameters vary considerably during the course of a few years. Often, the relative standard deviation is larger than 10%. Such variations can certainly also be found for stars other than the sun. According to Demtröder 2018 Mach numbers higher than 1 imply that shock phenomena can in priciple

Table 6.5: Stellar wind parameters, screening, Coulomb correction, sound speed and Mach number for planetary systems.

Planet	ρ_W[m^{-3}]	T[MK]	λ_D[m]	Coulomb corr.	c[km/s]	Δu_w[km/s]	M
HD 189733 b	$1.2 \cdot 10^{10}$	5.9	1.1	$1.2 \cdot 10^{-12}$	285	620	2.2
WASP-69b	$2.0 \cdot 10^{9}$	2.8	1.8	$1.6 \cdot 10^{-12}$	195	475	2.4
WASP-131b	$3.7 \cdot 10^{9}$	1.1	$8.5 \cdot 10^{-1}$	$8.3 \cdot 10^{-12}$	124	312	2.5
KELT-7b	$2.8 \cdot 10^{10}$	6.8	$7.7 \cdot 10^{-1}$	$1.5 \cdot 10^{-12}$	306	895	2.9
KELT-20b	$5.7 \cdot 10^{10}$	$7 \cdot 10^{-3}$	$1.7 \cdot 10^{-2}$	$6.6 \cdot 10^{-8}$	9.81	1222	124
Jupiter	$2.9 \cdot 10^{5}$	0.5	67	$2.2 \cdot 10^{-13}$	86.4	391	4.5

be observed. As can be seen from table 6.5 the motion of the planets through the interplanetary medium is clearly supersonic, especially for KELT-20b. This implies that all planets could potentially have bow shocks as outlined in Vidotto et al. 2010.
If strong mangetic fields are present equation 6.32 has to be replaced by

$$c_A = \frac{\vec{B_\star}}{\sqrt{\mu_0 \widetilde{\rho_W}}} \tag{6.33}$$

with stellar magnetic field $\vec{B_\star}$, vacuum magnetic permeability μ_0 and stellar wind density $\widetilde{\rho_W}$[kg/m^3]. A major drawback of this equation is that the value of $\vec{B_\star}$ is unknown. Ebert et al. 2014 point out that this value varies by more than a factor of ten during the course of the 23rd solar cycle. This in turn implies that the Alfvénic velocity c_A is uncertain by the same factor. Fortunately, the value of c is larger than c_A unless extremely high values for $\vec{B_\star}$ are assumed. This shows that the assumption of supersonic motion can be supported.

6.7 Estimation of the Bow Shock Standoff Distance

Because of the finite observing cadence and the intrinsic measurement error of each data point only a bow shock with sufficient duration and depth can be reliably detected. Figure 6.2 presents three possible

scenarios how observing cadence and insufficient absorption-depth can hinder the detection of bow shock absorption features. In these scenarios the bow shock consists of a Gaussian absorption feature. If observations could be carried out with an infinite temporal resolution and without any measurement error the presence of the bow shock could easily be detected. When taking into account a finite observing cadence and limited measurement accuracy the identification of a bow shock is not so obvious any more. For instance, let us assume a bow shock with a duration of the sampling frequency. More precisely let the FWHM of the Gaussian profile correspond to the observing cadence. Such scenarios are shown in figure 6.2. Depending on the position of the absorption maximum either one or two data points could show an absorption feature. It should be kept in mind that the identification is only possible if the noise level is sufficiently low. If we instead assume a FWHM of 7 minutes of the absorption feature the observed transit depth will be reduced, although the true absorption depth remains unchanged. In this scenario the identification of the feature will be more vulnerable to noise. Apart from that real observations are also affected by systematic errors or trends. As discussed in chapter 5 none of the transit light curves show any convincing evidence for planetary pre-transit absorption. An interpretation of this finding is that the depth of the absorption maximum is lower than the detection threshold. In this case, the bow shock could be located everywhere. This interpretation seems to be unlike because Cauley et al. 2015 has shown that the bow shock in Hα is as deep as 10mÅ. Such a deep feature would have been detectable in all observing runs. This assuption would therefore require a physical explanation why the depth bow shocks decreased in the observations discussed previously.

Bow Shock Was Missed

Another interpretation is that the bow shock is present but has not been recorded because it occurred before observations began. In this scenario the observations allow to estimate a lower limit of the time that elapses between the passage of the bow shock and the planetary transit Δt. This duration can be converted to a projected distance between planet and bow shock:

$$r_{M,proj} = \frac{\Delta t}{P_{Planet}} 2\pi a \tag{6.34}$$

where $r_{M,proj}$ is the projected distance between them, P_{Planet} is the planetary orbital period and a is the semi-major axis. In the case of HD 189733 b I adopt that Δt infinitely high. As shown in Kohl et al. 2018 all orbital phases have been sampled and thus the bow shock cannot be hidden at any orbital phase. Of course, this conclusion is only valid if the bow shock is not intermittent.

Bow Shock Occurs Directly Before First Contact

The bow shock may not only be hidden because it was missed before observations began. It could also have been missed because it occured extremely shortly before the first contact. The temporal distance between bow shock and planet could have been shorter than the finite observing cadence. In this case the the drop caused by the bow shock in the Hα light curve is not apparent.

6.7.1 Observational Projection Effects

As of February 2021 none of the planets regarded in this work are known to be on an elliptic orbit. In all cases the literature values for the upper limit of the eccentricity is less than or equal 0.11[2]. Additionally, it's in the nature of transiting exoplanets that their inclination is close to 90°. This implies that the direction of the orbital motion during transit is nearly perpendicular to the line of sight. In contrast, the purely radial stellar wind is streaming towards us. As outlined in section 4.1 we cannot observe the true distance between bow shock and planet but only the projected one. To derive r_M we need equation 6.12 to calculate the Keplerian velocity, equation 6.3 to calculate the stellar wind velocity and finally equation 4.2 to calculate the angle θ between them. Then, $r_{M,proj} = r_M \cos(\theta)$. According to equation 6.1 r_m depends on the strength of the magnetic field. As closer r_m is as weaker the derived magnetic field B_P is. Because $B_P \propto r_m^3$ a long separation between bow shock and planet would easily give unrealistically high values for B_P, particularly it would become orders of magnitude higher than Jupiter's B_P value. Table 6.6 summarizes the bow shock standoff distances as well as selected quantities required to obtain them. To distinguish the scenario of the missed bow shock from the observing cadence limited scenario the quntities belonging to the latter are labelled by the subscript "OC".

[2]For HD 189733 b Bonomo et al. 2017 give an upper limit of 0.0039 at 1σ confidence.

Notes. For HD 189733 b I assume an observing cadence of 7.4 minutes. This value I obtain from the dataset that forms the basis of figure 8 in Kohl et al. 2018. For KELT-7 b the Δt value originates from the ESPERO obsering run and the Δt_{OC} value originates from the CARMENES obsering run. This is motivated by the fact that the observed pre-transit phase is longer in the ESPERO observation but the obsering cadence is higher in the CARMENES observation.

Table 6.6: Compilation of r_M values and auxiliary quantities to derive it. For Jupiter, I adopt again the parameters given in Ebert et al. 2014.

Planet	Δt[min]	Δt_{OC}[min]	v_{Kep}[km/s]	$v\,(r)$[km/s]	θ[deg]	$r_M[R_{Jup}]$	$r_{M,OC}[R_{Jup}]$
HD 189733 b	∞	7.4	150	601	76.0	∞	1.9
WASP-69b	117	5.8	139	454	73.0	21.5	1.1
WASP-131b	337	5.8	124	286	66.5	44.1	0.8
KELT-7b	250	5.6	188	875	77.9	87.9	2.0
KELT-20b	51	3.9	170	1210	82.0	26.0	2.0
Jupiter	N/A	N/A	13	391	88.0	N/A	N/A

6.8 Putting all Ingredients Together

Now we have all ingredients at hand that are required to obtain B_P and eventually B_{eq} by employing equation 6.1. In table 6.7 I compare the observational upper limit derived from equation 6.1 to the estimation as given in equation 6.29. It is intriguing to see that the magnetic field as expected from the rotational velocity is predominantly higher than the observational upper limit. This result is in remarkable disagreement with the value of $\mathrm{B}_{eq} = 28$G derived by Cauley et al. 2015 and also with the observed field of Jupiter (≈ 4G). The authors conclude that this could be explained by adjusting the internal heat flux in hot Jupiters. The results given in table 6.7 also demonstrate that the planetary magnetic field of hot Jupiters does not follow the scaling relation given by equation 6.29. As Reiners and Christensen 2010 point out the magnetic field strength of a hot Jupiter critically depends on their rotation velocity. If it is too low, the magnetic field breaks down. Because the exact breakdown rotation velocity is uncertain also the magnetic field prediction is.

Table 6.7: Stellar wind pressure, its magnetic field, reference for this value and limits of the planetary magnetic field. For Jupiter, all values come from Ebert et al. 2014.
References. E14: Ebert et al. 2014; L13: Llama et al. 2013; P10: Petit et al. 2010; V14: Vidotto et al. 2014.

Planet	P_W[nPa]	$\vec{B_\star}$[G]	Ref.	$\mathrm{B}_{Jup,eq}$[G]	B_{eq}[G]	$\mathrm{B}_{eq,OC}$[G]
HD 189733 b	982	$1.6 \cdot 10^{-2}$	L13	1.7	∞	0.2
WASP-69b	76	$1.6 \cdot 10^{-2}$	V14	1.3	155	$1.9 \cdot 10^{-2}$
WASP-131b	57	$2.7 \cdot 10^{-3}$	V14	1.1	618	$3.2 \cdot 10^{-3}$
KELT-7b	2,604	$1.7 \cdot 10^{-3}$	V14	1.5	18,826	0.2
KELT-20b	5	$2.3 \cdot 10^{-4}$	P10	1.4	631	0.3
Jupiter	0.081	$7.2 \cdot 10^{-6}$	E14	4	N/A	N/A

Chapter 7

Summary of Main Results and Outlook

This work has shown that planetary pre-transit absorption features are not ubiquitous phenomena in extrasolar planetary systems containing hot Jupiters. If their existence is presumed, the absorption depths caused by these phenomena must be shallower than a few milli-Ångströms. Otherwise they could not have escaped detection. Especially for the transits observed with UVES the margin is low. Alternatively, they must have occurred outside of the observing windows. This assumption is unlike. It would require slowly rotating planets with magnetic fields in excess of 100G. Such a value is orders of magnitude higher than Jupiter's field. This is in strong contrast with typcial fields of extrasolar planets well below this threshold (Reiners and Christensen 2010). An exception from their finding would therefore be remarkable. A more realistic explanation for pre-transit absorption features as found in the spectra of HD 189733 b is stellar activity. Especially huge prominences with high brightness in Hα but low brightness in CaII H&K are important in this context.
These results have a rather large scope of application ranging from stars of spectral K to A, planetary masses between 0.26 and $3.5 M_{Jup}$ and planetary radii between 1.1 and $1.8 R_{Jup}$. Of course, not every known hot Jupiter has been regarded in this work. Furthermore, the sample discussed in this work by far does not encompass the variety of hot Jupiters. It rather is limited to a few exemplary combinations of planetary, orbital and stellar parameters. Due to the fact that new planets continue to be discovered a complete sample cannot be defined in the foreseeable future.
A contamination of nearby stellar spectra by interstellar absorption features could be ruled out. Potential differences between synthetic spectra and observations in the visible wavelength range are rarely caused by an unknown interstellar absorber. A better explanation is an inaccurate choice of the stellar model. I might be fruitful to revise the stellar template.
In addition to these astrophysical sources stellar spectra are also contaminated both by telluric absorption lines and instrumental artifacts. In combination, both processes can easily mimic astrophysical signals on the order of several milli-Ångströms. Because the former depend on local meteorological conditions and the latter is instrument specific these aspects should be checked before postulating astrophysical processes.
A major limitation for the study of planetary bow shocks is that the majority of planets require large telescopes to achieve high S/N and high temporal cadence simultaneously. This requirement of large telescope size could vanish in the future with the advent of a more complete sample of planets around bright stars. For instance, Henry 2020 lists several newly discovered planets around stars brighter than 7th magnitude. An example is HD 158259 b (Hara et al. 2020). This planet was discovered by TESS (Latham 2021). In contrast to other space telescopes this one has an extremely large field of view 2160 square degrees. It observes the same region of the sky for 27.4 days. Large parts of the sky have already been covered but the coverage is still incomplete. In addition, data processing is still ongoing. Certainly, even more planets will have been discovered by this space telescope after the results will have been finalised. Presumably, some of the yet to be discovered planets will be hot Jupiters and will orbit hot stars without stellar activity contamination.

Chapter 8

Acknowledgements

First, let's come to the official part: this research has made use of the SIMBAD database, operated at CDS, Strasbourg, France, and the VizieR catalog access tool, operated at CDS, the Exoplanet Orbit Database and the Exoplanet Data Explorer at exoplanets.org, the NASA Exoplanet Archive, which is operated by the California Institute of Technology, under contract with the National Aeronautics and Space Administration under the Exoplanet Exploration Program, of the Washington Double Star Catalog maintained at the US Naval Observatory, of PyAstronomy, of numpy, of Scipy, of matplotlib, of NASAs Astrophysics Data System, of SILSO data, Royal Observatory of Belgium, Brussels and of the NIST Atomic Spectra Database, maintained at the National Institute of Standards and Technology, Gaithersburg, MD. Solar Hα data, CaII H&K data and white light data were provided by the Kanzelhöhe Observatory, University of Graz, Austria.
Based on observations collected at the European Organisation for Astronomical Research in the Southern Hemisphere under ESO programmes 097.C-0863(A) and 099.C-0586(B), at the Calar Alto Observatory, at the Rozhen National Astronomical Observatory Bulgaria and at the TIGRE Telescope.
I am also grateful that Astronomy & Astrophysics kindly permits the reproduction of my papers in this work.

And last but not least I also would like to use this page to thank all people who supported me during the time of my PhD thesis. Without your help I would not have been able to finish this work! Thank you so much!
I gratefully thank my supervisor Prof. Jürgen Schmitt for the opportunity to work in his group, for his feedback, his ideas and many good advices throughout the course of this work. These have been invaluable for me.
Also I am thankful to Stefan and Michael who directed my attention to the subject of this thesis and for intersting feedback and discussions about these topics.
I would like to thank Holger for his kind help with the conversion of solar images to light curves and for providing his code.
I thank Johannes for his help with stellar template subtraction and for providing his code for this purpose.
I also would like to thank Dominik, Evangelos and Jan for the productive, friendly and relaxing atmosphere in our office.
I am also grateful to all people who haven't yet been named and who provided interesting scientific or sometimes not so scientific insights and fruitful discussions. Be it during heavily extended coffee/lunch breaks, because people just dropped in to ask for sticky tape/a book/a tea bag and left two hours later or in passing.
Finally, I also would like to thank my friends and my family for the incredible support during the not always easy time of my PhD thesis.

Chapter 9

Ergänzungen

9.1 Eidesstattliche Versicherung / Declaration on oath

Hiermit versichere ich an Eides statt, die vorliegende Dissertationsschrift selbst verfasst und keine anderen als die angegebenen Hilfsmittel und Quellen benutzt zu haben.

Die eingereichte schriftliche Fassung entspricht der auf dem elektronischen Speichermedium.

Die Dissertation wurde in der vorgelegten oder einer ähnlichen Form nicht schon einmal in einem früheren Promotionsverfahren angenommen oder als ungenügend beurteilt.

Hamburg, den 03.04.2021

Unterschrift der Doktorandin / des Doktoranden

9.2 Aus dieser Dissertation hervorgegangene Vorveröffentlichungen

Teile dieser Dissertation wurden bereits in folgenden Publikationen vorab veröffentlicht:

Kohl, S. et al. (2016). On the nature of absorption features toward nearby stars. In: *Astronomy & Astrophysics* 591, A20, A20.

Kohl, S. et al. (2018). HD 189733 b: bow shock or no shock? In: *Astronomy & Astrophysics* 619, A96, A96.

Bibliography

Anderson, D. R. et al. (2014). "Three newly discovered sub-Jupiter-mass planets: WASP-69b and WASP-84b transit active K dwarfs and WASP-70Ab transits the evolved primary of a G4+K3 binary". In: *Monthly Notices of the Royal Astronomical Society* 445.2, pp. 1114–1129. DOI: 10.1093/mnras/stu1737. arXiv: 1310.5654 [astro-ph.EP].

Appenzeller, I. (2013). *Introduction to astronomical spectroscopy*. Cambridge observing handbooks for research astronomers 9. Cambridge Univ. Press. URL: http://www.gbv.de/dms/bowker/toc/9781107015791.pdf.

Aufdenberg, J. P. et al. (2006). "First Results from the CHARA Array. VII. Long-Baseline Interferometric Measurements of Vega Consistent with a Pole-On, Rapidly Rotating Star". In: *The Astrophysical Journal* 645.1, pp. 664–675. DOI: 10.1086/504149. arXiv: astro-ph/0603327 [astro-ph].

Bailer-Jones, C. A. L. et al. (2018). "Estimating Distance from Parallaxes. IV. Distances to 1.33 Billion Stars in Gaia Data Release 2". In: *The Astronomical Journal* 156.2, 58, p. 58. DOI: 10.3847/1538-3881/aacb21. arXiv: 1804.10121 [astro-ph.SR].

Bailey, Mandy et al. (2016). "Probing the Local Bubble with diffuse interstellar bands. I. Project overview and southern hemisphere survey". In: *Astronomy & Astrophysics* 585, A12, A12. DOI: 10.1051/0004-6361/201526656. arXiv: 1509.08025 [astro-ph.GA].

Baliunas, S. L. et al. (1995). "Chromospheric Variations in Main-Sequence Stars. II." In: *The Astrophysical Journal* 438, p. 269. DOI: 10.1086/175072.

Barnes, J. R. et al. (2016). "The origin of the excess transit absorption in the HD 189733 system: planet or star?" In: *Monthly Notices of the Royal Astronomical Society* 462.1, pp. 1012–1028. DOI: 10.1093/mnras/stw1713. arXiv: 1607.03684 [astro-ph.EP].

Bertin, P. et al. (1995). "HST-GHRS observations of Sirius A. III. Detection of a stellar wind from Sirius A". In: *Astronomy & Astrophysics* 302, p. 899.

Bieryla, Allyson et al. (2015). "KELT-7b: A Hot Jupiter Transiting a Bright V = 8.54 Rapidly Rotating F-star". In: *The Astronomical Journal* 150.1, 12, p. 12. DOI: 10.1088/0004-6256/150/1/12. arXiv: 1501.05565 [astro-ph.EP].

Bohn, A. J. et al. (2020). "A multiplicity study of transiting exoplanet host stars. I. High-contrast imaging with VLT/SPHERE". In: *Astronomy & Astrophysics* 635, A73, A73. DOI: 10.1051/0004-6361/201937127. arXiv: 2001.08224 [astro-ph.EP].

Bonev, Tanyu et al. (2017). "ESpeRo: Echelle Spectrograph Rozhen". In: *Bulgarian Astronomical Journal* 26, p. 67. arXiv: 1612.07226 [astro-ph.IM].

Bonomo, A. S. et al. (2017). "The GAPS Programme with HARPS-N at TNG . XIV. Investigating giant planet migration history via improved eccentricity and mass determination for 231 transiting planets". In: *Astronomy & Astrophysics* 602, A107, A107. DOI: 10.1051/0004-6361/201629882. arXiv: 1704.00373 [astro-ph.EP].

Bourrier, V. et al. (2020). "MOVES III. Simultaneous X-ray and ultraviolet observations unveiling the variable environment of the hot Jupiter HD 189733b". In: *Monthly Notices of the Royal Astronomical Society* 493.1, pp. 559–579. DOI: 10.1093/mnras/staa256. arXiv: 2001.11048 [astro-ph.EP].

Boyajian, Tabetha S. et al. (2013). "Stellar Diameters and Temperatures. III. Main-sequence A, F, G, and K Stars: Additional High-precision Measurements and Empirical Relations". In: *The Astrophysical Journal* 771.1, 40, p. 40. DOI: 10.1088/0004-637X/771/1/40. arXiv: 1306.2974 [astro-ph.SR].

Brahm, Rafael et al. (2019). "HD 1397b: A Transiting Warm Giant Planet Orbiting A V = 7.8 mag Subgiant Star Discovered by TESS". In: *The Astronomical Journal* 158.1, 45, p. 45. DOI: 10.3847/1538-3881/ab279a. arXiv: 1811.02156 [astro-ph.EP].

Brogi, M. et al. (2016). "Rotation and Winds of Exoplanet HD 189733 b Measured with High-dispersion Transmission Spectroscopy". In: *The Astrophysical Journal* 817.2, 106, p. 106. DOI: 10.3847/0004-637X/817/2/106. arXiv: 1512.05175 [astro-ph.EP].

Caballero, J. A. et al. (2016). "CARMENES: data flow". In: *Observatory Operations: Strategies, Processes, and Systems VI*. Ed. by Alison B. Peck et al. Vol. 9910. Society of Photo-Optical Instrumentation Engineers (SPIE) Conference Series, 99100E. DOI: 10.1117/12.2233574.

Campbell, E. K. et al. (2015). "Laboratory confirmation of C_{60}^+ as the carrier of two diffuse interstellar bands". In: *Nature* 523.7560, pp. 322–323. DOI: 10.1038/nature14566.

Cap, F. (1994). *Lehrbuch der Plasmaphysik und Magnetohydrodynamik*. Springer Vienna. URL: http://dx.doi.org/10.1007/978-3-7091-6622-2.

Casasayas-Barris, N. et al. (2019). "Atmospheric characterization of the ultra-hot Jupiter MASCARA-2b/KELT-20b. Detection of CaII, FeII, NaI, and the Balmer series of H (Hα, Hβ, and Hγ) with high-dispersion transit spectroscopy". In: *Astronomy & Astrophysics* 628, A9, A9. DOI: 10.1051/0004-6361/201935623. arXiv: 1905.12491 [astro-ph.EP].

Cauley, P. Wilson et al. (2015). "Optical Hydrogen Absorption Consistent with a Thin Bow Shock Leading the Hot Jupiter HD 189733b". In: *The Astrophysical Journal* 810.1, 13, p. 13. DOI: 10.1088/0004-637X/810/1/13. arXiv: 1507.05916 [astro-ph.EP].

Cauley, P. Wilson et al. (2016). "Variation in the Pre-transit Balmer Line Signal Around the Hot Jupiter HD 189733b". In: *The Astronomical Journal* 152.1, 20, p. 20. DOI: 10.3847/0004-6256/152/1/20. arXiv: 1605.01955 [astro-ph.EP].

Cauley, P. Wilson et al. (2017a). "A Decade of Hα Transits for HD 189733 b: Stellar Activity versus Absorption in the Extended Atmosphere". In: *The Astronomical Journal* 153.5, 217, p. 217. DOI: 10.3847/1538-3881/aa6a15. arXiv: 1703.09543 [astro-ph.EP].

— (2017b). "A Search for Hα Absorption around KELT-3 b and GJ 436 b". In: *The Astronomical Journal* 153.2, 81, p. 81. DOI: 10.3847/1538-3881/153/2/81. arXiv: 1612.05945 [astro-ph.EP].

Cauley, P. Wilson et al. (2018). "The Effects of Stellar Activity on Optical High-resolution Exoplanet Transmission Spectra". In: *The Astronomical Journal* 156.5, 189, p. 189. DOI: 10.3847/1538-3881/aaddf9. arXiv: 1808.09558 [astro-ph.EP].

Chiozzi, Gianluca et al. (2016). "The ESO astronomical site monitor upgrade". In: *Software and Cyberinfrastructure for Astronomy IV*. Ed. by Gianluca Chiozzi and Juan C. Guzman. Vol. 9913. Society of Photo-Optical Instrumentation Engineers (SPIE) Conference Series, p. 991314. DOI: 10.1117/12.2232302.

Ciardi, D. (2020). *NASA Exoplanet Archive*. URL: https://exoplanetarchive.ipac.caltech.edu/ (visited on 03/05/2021).

Claret, A. (2019). "Tables of Limb-darkening and Gravity-darkening Coefficients for the Space Mission Gaia". In: *Research Notes of the American Astronomical Society* 3.1, 17, p. 17. DOI: 10.3847/2515-5172/aaffdf.

Clette, F. (2020). *World Data Center for the production, preservation and dissemination of the international sunspot number*. URL: http://www.sidc.be/silso/home (visited on 03/05/2021).

Coker, Carl T. et al. (2018). "A Search for Binary Star Companions to the KELT Planet Hosts and a Comparison Sample. I. Results of DSSI Observations". In: *The Astronomical Journal* 155.1, 27, p. 27. DOI: 10.3847/1538-3881/aa9f0e.

Connerney, J. E. P. et al. (2018). "A New Model of Jupiter's Magnetic Field From Juno's First Nine Orbits". In: *Geophysical Research Letters* 45.6, pp. 2590–2596. DOI: 10.1002/2018GL077312.

Csizmadia, Sz. et al. (2019). "An estimate of the k_2 Love number of WASP-18Ab from its radial velocity measurements". In: *Astronomy & Astrophysics* 623, A45, A45. DOI: 10.1051/0004-6361/201834376. arXiv: 1812.04463 [astro-ph.EP].

Czesla, S. et al. (2015). "The center-to-limb variation across the Fraunhofer lines of HD 189733. Sampling the stellar spectrum using a transiting planet". In: *Astronomy & Astrophysics* 582, A51, A51. DOI: 10.1051/0004-6361/201526386. arXiv: 1509.05657 [astro-ph.SR].

Czesla, Stefan et al. (2019). *PyA: Python astronomy-related packages*. ascl: 1906.010.

Dekker, Hans et al. (2000). "Design, construction, and performance of UVES, the echelle spectrograph for the UT2 Kueyen Telescope at the ESO Paranal Observatory". In: *Optical and IR Telescope Instrumentation and Detectors*. Ed. by Masanori Iye and Alan F. Moorwood. Vol. 4008. Society of Photo-Optical Instrumentation Engineers (SPIE) Conference Series, pp. 534–545. DOI: 10.1117/12.395512.

Deleuil, M. et al. (2018). "Planets, candidates, and binaries from the CoRoT/Exoplanet programme. The CoRoT transit catalogue". In: *Astronomy & Astrophysics* 619, A97, A97. DOI: 10.1051/0004-6361/201731068. arXiv: 1805.07164 [astro-ph.EP].

Demtröder, Wolfgang (2018). *Experimentalphysik 1 Mechanik und Wärme*. 8. Auflage. Lehrbuch: Springer eBook Collection: Springer-Lehrbuch: SpringerLink: Bücher. Springer Spektrum. URL: https://doi.org/10.1007/978-3-662-54847-9.

Ebert, Robert et al. (2014). "A survey of solar wind conditions at 5 AU: A tool for interpreting solar wind-magnetosphere interactions at Jupiter". In: *Frontiers in Astronomy and Space Sciences* 1, 4, p. 4. DOI: 10.3389/fspas.2014.00004.

Ehrenreich, David et al. (2015). "A giant comet-like cloud of hydrogen escaping the warm Neptune-mass exoplanet GJ 436b". In: *Nature* 522.7557, pp. 459–461. DOI: 10.1038/nature14501. arXiv: 1506.07541 [astro-ph.EP].

Farhang, Amin et al. (2015). "Probing the Local Bubble with Diffuse Interstellar Bands. II. The DIB Properties in the Northern Hemisphere". In: *The Astrophysical Journal* 800.1, 64, p. 64. DOI: 10.1088/0004-637X/800/1/64. arXiv: 1412.0044 [astro-ph.GA].

Fischer, Debra A. et al. (2016). "State of the Field: Extreme Precision Radial Velocities". In: *Publications of the Astronomical Society of the Pacific* 128.964, p. 066001. DOI: 10.1088/1538-3873/128/964/066001. arXiv: 1602.07939 [astro-ph.IM].

Fossati, L. et al. (2017). "Aeronomical constraints to the minimum mass and maximum radius of hot low-mass planets". In: *Astronomy & Astrophysics* 598, A90, A90. DOI: 10.1051/0004-6361/201629716. arXiv: 1612.05624 [astro-ph.EP].

Fossati, L. et al. (2018). "Extreme-ultraviolet Radiation from A-stars: Implications for Ultra-hot Jupiters". In: *The Astrophysical Journal Letters* 868.2, L30, p. L30. DOI: 10.3847/2041-8213/aaf0a5. arXiv: 1811.05460 [astro-ph.EP].

Foukal, P. (2013). *Solar astrophysics*. 3., rev. ed. Physics textbook. Wiley-VCH. URL: http://d-nb.info/1026137306/04.

Gaia Collaboration (2018). "VizieR Online Data Catalog: Gaia DR2 (Gaia Collaboration, 2018)". In: *VizieR Online Data Catalog*, I/345, pp. I/345.

García, Rafael A. and Jérôme Ballot (2019). "Asteroseismology of solar-type stars". In: *Living Reviews in Solar Physics* 16.1, 4, p. 4. DOI: 10.1007/s41116-019-0020-1. arXiv: 1906.12262 [astro-ph.SR].

García Muñoz, A. and P. C. Schneider (2019). "Rapid Escape of Ultra-hot Exoplanet Atmospheres Driven by Hydrogen Balmer Absorption". In: *The Astrophysical Journal Letters* 884.2, L43, p. L43. DOI: 10.3847/2041-8213/ab498d. arXiv: 1910.00267 [astro-ph.EP].

Gladman, Brett et al. (1996). "Synchronous Locking of Tidally Evolving Satellites". In: *Icarus* 122.1, pp. 166–192. DOI: 10.1006/icar.1996.0117.

Głębocki, R. and P. Gnaciński (2005). "Systematic errors in the determination of stellar rotational velocities". In: *13th Cambridge Workshop on Cool Stars, Stellar Systems and the Sun*. Ed. by F. Favata et al. Vol. 560. ESA Special Publication, p. 571.

Gray, David F. (2005). *The observation and analysis of stellar photospheres*. Third edition. Cambridge University Press, p. 533. URL: http://dx.doi.org/10.1017/CBO9781316036570.

Groom, Don (2002). "Cosmic rays and other nonsense in astronomical CCD imagers". In: *Experimental Astronomy* 14.1, pp. 45–55. DOI: 10.1023/A:1026196806990.

Hall, Jeffrey C. (1996). "On the Determination of Empirical Stellar Flux Scales". In: *Publications of the Astronomical Society of the Pacific* 108, p. 313. DOI: 10.1086/133724.

Hall, Jeffrey C. et al. (2007). "The Activity and Variability of the Sun and Sun-like Stars. I. Synoptic Ca II H and K Observations". In: *The Astronomical Journal* 133.3, pp. 862–881. DOI: 10.1086/510356.

Hamuy, Mario et al. (1992). "Southern Spectrophotometric Standards. I." In: *Publications of the Astronomical Society of the Pacific* 104, p. 533. DOI: 10.1086/133028.

Hara, N. C. et al. (2020). "The SOPHIE search for northern extrasolar planets. XVI. HD 158259: A compact planetary system in a near-3:2 mean motion resonance chain". In: *Astronomy & Astrophysics* 636, L6, p. L6. DOI: 10.1051/0004-6361/201937254. arXiv: 1911.13296 [astro-ph.EP].

Harris, Charles R. et al. (2020). "Array programming with NumPy". In: *Nature* 585.7825, pp. 357–362. DOI: 10.1038/s41586-020-2649-2. URL: https://doi.org/10.1038/s41586-020-2649-2.

Heasley, J. N. and R. W. Milkey (1978). "Structure and spectrum of quiescent prominences. III. Application of theoretical models in helium abundance determinations." In: *The Astrophysical Journal* 221, pp. 677–688. DOI: 10.1086/156072.

Hellier, C. et al. (2017). "WASP-South transiting exoplanets: WASP-130b, WASP-131b, WASP-132b, WASP-139b, WASP-140b, WASP-141b and WASP-142b". In: *Monthly Notices of the Royal Astronomical Society* 465.3, pp. 3693–3707. DOI: 10.1093/mnras/stw3005. arXiv: 1604.04195 [astro-ph.EP].

Hempelmann, A. et al. (1996). "Coronal X-ray emission of cool stars in relation to chromospheric activity and magnetic cycles." In: *Astronomy & Astrophysics* 305, p. 284.

Henry, F. (2020). *The Extrasolar Planets Encyclopaedia*. URL: http://exoplanet.eu (visited on 03/05/2021).

Hobbs, L. M. et al. (2009). "Studies of the Diffuse Interstellar Bands. III. HD 183143". In: *The Astrophysical Journal* 705.1, pp. 32–45. DOI: 10.1088/0004-637X/705/1/32. arXiv: 0910.2983 [astro-ph.GA].

Howell, Steve B. (2006). *Handbook of CCD astronomy*. 2. ed. Cambridge observing handbooks for research astronomers 5. Cambridge University Press. URL: http://www.gbv.de/dms/goettingen/504624237.pdf.

Husser, T. O. et al. (2013). "A new extensive library of PHOENIX stellar atmospheres and synthetic spectra". In: *Astronomy & Astrophysics* 553, A6, A6. DOI: 10.1051/0004-6361/201219058. arXiv: 1303.5632 [astro-ph.SR].

Jensen, Adam G. et al. (2012). "A Detection of Hα in an Exoplanetary Exosphere". In: *The Astrophysical Journal* 751.2, 86, p. 86. DOI: 10.1088/0004-637X/751/2/86. arXiv: 1203.4484 [astro-ph.EP].

Jensen, Adam G. et al. (2018). "Hydrogen and Sodium Absorption in the Optical Transmission Spectrum of WASP-12b". In: *The Astronomical Journal* 156.4, 154, p. 154. DOI: 10.3847/1538-3881/aadca7. arXiv: 1808.07010 [astro-ph.EP].

Johns-Krull, Christopher M. et al. (1997). "Hamilton Echelle Spectroscopy of the 1993 March 6 Solar Flare". In: *The Astrophysical Journal Supplement Series* 112.1, pp. 221–243. DOI: 10.1086/313030.

Johnstone, C. P. et al. (2015). "Stellar winds on the main-sequence. I. Wind model". In: *Astronomy & Astrophysics* 577, A27, A27. DOI: 10.1051/0004-6361/201425300. arXiv: 1503.06669 [astro-ph.SR].

Jordi, C. et al. (2010). "Gaia broad band photometry". In: *Astronomy & Astrophysics* 523, A48, A48. DOI: 10.1051/0004-6361/201015441. arXiv: 1008.0815 [astro-ph.IM].

Klioner, S. (2020). *IAU resolutions*. URL: https://www.iau.org/static/resolutions/IAU2015_English.pdf (visited on 03/05/2021).

Klocová, T. et al. (2017). "Time-resolved UVES observations of a stellar flare on the planet host HD 189733 during primary transit". In: *Astronomy & Astrophysics* 607, A66, A66. DOI: 10.1051/0004-6361/201630068. arXiv: 1707.09831 [astro-ph.SR].

Koch, Bernd, ed. (1995). *Handbuch der Astrofotografie*. Springer. URL: http://www.gbv.de/dms/goettingen/171751027.pdf.

Koch, David G. et al. (2010). "Kepler Mission Design, Realized Photometric Performance, and Early Science". In: *The Astrophysical Journal Letters* 713.2, pp. L79–L86. DOI: 10.1088/2041-8205/713/2/L79. arXiv: 1001.0268 [astro-ph.EP].

Kohl, S. et al. (2016). "On the nature of absorption features toward nearby stars". In: *Astronomy & Astrophysics* 591, A20, A20. DOI: 10.1051/0004-6361/201628482.

Kohl, S. et al. (2018). "HD 189733 b: bow shock or no shock?" In: *Astronomy & Astrophysics* 619, A96, A96. DOI: 10.1051/0004-6361/201833567.

Kramida, A. (2020). *NIST Atomic Spectra Database Lines Form*. URL: https://physics.nist.gov/PhysRefData/ASD/lines_form.html (visited on 03/05/2021).

Kubyshkina, D. et al. (2018). "Overcoming the Limitations of the Energy-limited Approximation for Planet Atmospheric Escape". In: *The Astrophysical Journal Letters* 866.2, L18, p. L18. DOI: 10.3847/2041-8213/aae586. arXiv: 1810.06920 [astro-ph.EP].

Latham, D. (2021). *TESS Homepage*. URL: https://tess.mit.edu (visited on 03/05/2021).

Lecavelier des Etangs, A. et al. (2012). "Temporal variations in the evaporating atmosphere of the exoplanet HD 189733b". In: *Astronomy & Astrophysics* 543, L4, p. L4. DOI: 10.1051/0004-6361/201219363. arXiv: 1206.6274 [astro-ph.EP].

Leussu, R. et al. (2017). "Wings of the butterfly: Sunspot groups for 1826-2015". In: *Astronomy & Astrophysics* 599, A131, A131. DOI: 10.1051/0004-6361/201629533.

Livingston, W. et al. (2007). "Sun-as-a-Star Spectrum Variations 1974-2006". In: *The Astrophysical Journal* 657.2, pp. 1137–1149. DOI: 10.1086/511127. arXiv: astro-ph/0612554 [astro-ph].

Llama, J. et al. (2013). "Exoplanet transit variability: bow shocks and winds around HD 189733b". In: *Monthly Notices of the Royal Astronomical Society* 436.3, pp. 2179–2187. DOI: 10.1093/mnras/stt1725. arXiv: 1309.2938 [astro-ph.EP].

Lo Curto, G. et al. (2015). "HARPS Gets New Fibres After 12 Years of Operations". In: *The Messenger* 162, pp. 9–15.

Lund, Michael B. et al. (2017). "KELT-20b: A Giant Planet with a Period of P ˜ 3.5 days Transiting the V ˜ 7.6 Early A Star HD 185603". In: *The Astronomical Journal* 154.5, 194, p. 194. DOI: 10.3847/1538-3881/aa8f95. arXiv: 1707.01518 [astro-ph.EP].

Mamajek, E. (2020). *A Modern Mean Dwarf Stellar Color and Effective Temperature Sequence*. URL: http://www.pas.rochester.edu/~emamajek/EEM_dwarf_UBVIJHK_colors_Teff.txt (visited on 03/05/2021).

Martin, J. et al. (2017). "The Ca II infrared triplet's performance as an activity indicator compared to Ca II H and K. Empirical relations to convert Ca II infrared triplet measurements to common activity indices". In: *Astronomy & Astrophysics* 605, A113, A113. DOI: 10.1051/0004-6361/201630298.

Martin, Johannes (2018). "The Calcium Infrared Triplet as an Indicator for Stellar Activity". PhD thesis. URL: http://nbn-resolving.de/urn:nbn:de:gbv:18-90454.

Mason, Brian D. et al. (2001). "The 2001 US Naval Observatory Double Star CD-ROM. I. The Washington Double Star Catalog". In: *The Astronomical Journal* 122.6, pp. 3466–3471. DOI: 10.1086/323920.

Mayor, Michel and Didier Queloz (1995). "A Jupiter-mass companion to a solar-type star". In: *Nature* 378.6555, pp. 355–359. DOI: 10.1038/378355a0.

McCall, B. (2021). *DIB Database*. URL: http://dibdata.org/ (visited on 03/05/2021).

Melo, C. et al. (2006). "On the age of stars harboring transiting planets". In: *Astronomy & Astrophysics* 460.1, pp. 251–256. DOI: 10.1051/0004-6361:20065954. arXiv: astro-ph/0609259 [astro-ph].

Mendez, A. (2020). *The Habitable Exoplanets Catalog*. URL: http://phl.upr.edu/projects/habitable-exoplanets-catalog (visited on 03/05/2021).

Mittag, M. et al. (2016). "Chromospheric activity and evolutionary age of the Sun and four solar twins". In: *Astronomy & Astrophysics* 591, A89, A89. DOI: 10.1051/0004-6361/201527542. arXiv: 1607.01279 [astro-ph.SR].

Mohr, Peter J. et al. (2016). "CODATA Recommended Values of the Fundamental Physical Constants: 2014*". In: *Journal of Physical and Chemical Reference Data* 45.4, 043102, p. 043102. DOI: 10.1063/1.4954402.

Monreal-Ibero, A. and R. Lallement (2017). "Measuring diffuse interstellar bands with cool stars. Improved line lists to model background stellar spectra". In: *Astronomy & Astrophysics* 599, A74, A74. DOI: 10.1051/0004-6361/201629757. arXiv: 1612.00202 [astro-ph.GA].

Monsch, Kristina et al. (2019). "The imprint of X-ray photoevaporation of planet-forming discs on the orbital distribution of giant planets". In: *Monthly Notices of the Royal Astronomical Society* 483.3, pp. 3448–3458. DOI: 10.1093/mnras/sty3346. arXiv: 1812.02173 [astro-ph.EP].

Müller, Holger Matthias (2015). "Limb-darkening Measurements on Exoplanet Host Stars and the Sun = Messungen der Randverdunkelung auf Exoplaneten-Zentralsternen und der Sonne". PhD thesis. URL: http://ediss.sub.uni-hamburg.de/volltexte/2016/8041/.

Nevelius, E. (2019). *The Nobel Prize in Physics 2019*. URL: https://www.nobelprize.org/prizes/physics/2019/press-release/ (visited on 03/05/2021).

Ni, Dongdong (2018). "Empirical models of Jupiter's interior from Juno data. Moment of inertia and tidal Love number k_2". In: *Astronomy & Astrophysics* 613, A32, A32. DOI: 10.1051/0004-6361/201732183.

Oelkers, Ryan J. et al. (2018). "Variability Properties of Four Million Sources in the TESS Input Catalog Observed with the Kilodegree Extremely Little Telescope Survey". In: *The Astronomical Journal* 155.1, 39, p. 39. DOI: 10.3847/1538-3881/aa9bf4. arXiv: 1711.03608 [astro-ph.SR].

Otruba, W. and W. Pötzi (2003). "The new high-speed Hα imaging system at Kanzelhöhe Solar Observatory". In: *Hvar Observatory Bulletin* 27.1, pp. 189–195.

Park, R. (2020). *Planets and Pluto: Physical Characteristics*. URL: https://ssd.jpl.nasa.gov/?planet_phys_par (visited on 03/05/2021).

Peron, M. (2020). *VLT Instrument Pipelines*. URL: http://www.eso.org/sci/software/pipelines/ (visited on 03/05/2021).

Petit, P. et al. (2010). "The rapid rotation and complex magnetic field geometry of Vega". In: *Astronomy & Astrophysics* 523, A41, A41. DOI: 10.1051/0004-6361/201015307. arXiv: 1006.5868 [astro-ph.SR].

Piskunov, N. E. and J. A. Valenti (2002). "New algorithms for reducing cross-dispersed echelle spectra". In: *Astronomy & Astrophysics* 385, pp. 1095–1106. DOI: 10.1051/0004-6361:20020175.

Poppenhaeger, K. et al. (2013). "Transit Observations of the Hot Jupiter HD 189733b at X-Ray Wavelengths". In: *The Astrophysical Journal* 773.1, 62, p. 62. DOI: 10.1088/0004-637X/773/1/62. arXiv: 1306.2311 [astro-ph.SR].

Pötzi, W. (2020a). *Kanzelhöhe Observatory – Instruments*. URL: https://www.kso.ac.at/instrumente/instrumente_en.php (visited on 03/05/2021).

— (2020b). *Solar Flares Patrol*. URL: http://cesar.kso.ac.at/flare_data/kh_flares_query.php (visited on 03/05/2021).

Pötzi, W. et al. (2015). "Real-time Flare Detection in Ground-Based Hα Imaging at Kanzelhöhe Observatory". In: *Solar Physics* 290.3, pp. 951–977. DOI: 10.1007/s11207-014-0640-5. arXiv: 1411.3896 [astro-ph.SR].

Quirrenbach, A. et al. (2014). "CARMENES instrument overview". In: *Ground-based and Airborne Instrumentation for Astronomy V*. Ed. by Suzanne K. Ramsay et al. Vol. 9147. Society of Photo-Optical Instrumentation Engineers (SPIE) Conference Series, 91471F. DOI: 10.1117/12.2056453.

Quirrenbach, A. et al. (2018). "CARMENES: high-resolution spectra and precise radial velocities in the red and infrared". In: *Ground-based and Airborne Instrumentation for Astronomy VII*. Ed. by Christopher J. Evans et al. Vol. 10702. Society of Photo-Optical Instrumentation Engineers (SPIE) Conference Series, 107020W. DOI: 10.1117/12.2313689.

Rackham, Benjamin V. et al. (2019). "The Transit Light Source Effect. II. The Impact of Stellar Heterogeneity on Transmission Spectra of Planets Orbiting Broadly Sun-like Stars". In: *The Astronomical Journal* 157.3, 96, p. 96. DOI: 10.3847/1538-3881/aaf892. arXiv: 1812.06184 [astro-ph.EP].

Radick, Richard R. et al. (2018). "Patterns of Variation for the Sun and Sun-like Stars". In: *The Astrophysical Journal* 855.2, 75, p. 75. DOI: 10.3847/1538-4357/aaaae3.

Raimond, S. et al. (2012). "A southern hemisphere survey of the 5780 and 6284 Å diffuse interstellar bands: correlation with the extinction". In: *Astronomy & Astrophysics* 544, A136, A136. DOI: 10.1051/0004-6361/201219191. arXiv: 1207.6092 [astro-ph.GA].

Redfield, Seth and Jeffrey L. Linsky (2008). "The Structure of the Local Interstellar Medium. IV. Dynamics, Morphology, Physical Properties, and Implications of Cloud-Cloud Interactions". In: *The Astrophysical Journal* 673.1, pp. 283–314. DOI: 10.1086/524002. arXiv: 0804.1802 [astro-ph].

Reiners, A. and U. R. Christensen (2010). "A magnetic field evolution scenario for brown dwarfs and giant planets". In: *Astronomy & Astrophysics* 522, A13, A13. DOI: 10.1051/0004-6361/201014251. arXiv: 1007.1514 [astro-ph.EP].

Reiners, A. et al. (2016). "The IAG solar flux atlas: Accurate wavelengths and absolute convective blueshift in standard solar spectra". In: *Astronomy & Astrophysics* 587, A65, A65. DOI: 10.1051/0004-6361/201527530. arXiv: 1511.03014 [astro-ph.SR].

Robrade, J. (2016). "eROSITA - Nearby Young Stars in X-rays". In: *Young Stars & Planets Near the Sun*. Ed. by J. H. Kastner et al. Vol. 314, pp. 280–285. DOI: 10.1017/S1743921315005943. arXiv: 1510.01161 [astro-ph.SR].

Rothman, L. S. et al. (2009). "The HITRAN 2008 molecular spectroscopic database". In: *Journal of Quantitative Spectroscopy and Radiative Transfer* 110.9-10, pp. 533–572. DOI: 10.1016/j.jqsrt.2009.02.013.

Royer, F. et al. (2014). "Normal A0-A1 stars with low rotational velocities. I. Abundance determination and classification". In: *Astronomy & Astrophysics* 562, A84, A84. DOI: 10.1051/0004-6361/201322762. arXiv: 1401.2372 [astro-ph.SR].

Rutten, R. G. M. (1984). "Magnetic structure in cool stars. VII. Absolute surface flux in CA IIH and K line cores." In: *Astronomy & Astrophysics* 130, pp. 353–360.

Salz, M. et al. (2016a). "Energy-limited escape revised. The transition from strong planetary winds to stable thermospheres". In: *Astronomy & Astrophysics* 585, L2, p. L2. DOI: 10.1051/0004-6361/201527042. arXiv: 1511.09348 [astro-ph.EP].

Salz, M. et al. (2016b). "Simulating the escaping atmospheres of hot gas planets in the solar neighborhood". In: *Astronomy & Astrophysics* 586, A75, A75. DOI: 10.1051/0004-6361/201526109. arXiv: 1511.09341 [astro-ph.EP].

Sarazin, M. and F. Roddier (1990). "The ESO differential image motion monitor". In: *Astronomy & Astrophysics* 227.1, pp. 294–300.

Sbordone, L. and C. Ledoux (2020). *Very Large Telescope Paranal Science Operations UV-Visual Echelle Spectrograph User manual*. URL: https://www.eso.org/sci/facilities/paranal/instruments/uves/doc/VLT-MAN-ESO-13200-1825_v103.pdf (visited on 03/05/2021).

Schmitt, J. H. M. M. et al. (2014). "TIGRE: A new robotic spectroscopy telescope at Guanajuato, Mexico". In: *Astronomische Nachrichten* 335, p. 787. DOI: 10.1002/asna.201412116.

Schrijver, Carolus J., ed. (2010). *Heliophysics evolving solar activity and the climates of space and Earth*. Cambridge University Press. URL: http://www.gbv.de/dms/goettingen/629895325.pdf.

Schröder, K. P. et al. (2017). "Carrington cycle 24: the solar chromospheric emission in a historical and stellar perspective". In: *Monthly Notices of the Royal Astronomical Society* 470.1, pp. 276–282. DOI: 10.1093/mnras/stx1147. arXiv: 1705.03777 [astro-ph.SR].

Seidelmann, P. Kenneth et al. (2007). "Report of the IAU/IAG Working Group on cartographic coordinates and rotational elements: 2006". In: *Celestial Mechanics and Dynamical Astronomy* 98.3, pp. 155–180. DOI: 10.1007/s10569-007-9072-y.

Sing, David K. et al. (2016). "A continuum from clear to cloudy hot-Jupiter exoplanets without primordial water depletion". In: *Nature* 529.7584, pp. 59–62. DOI: 10.1038/nature16068. arXiv: 1512.04341 [astro-ph.EP].

Smette, A. et al. (2015). "Molecfit: A general tool for telluric absorption correction. I. Method and application to ESO instruments". In: *Astronomy & Astrophysics* 576, A77, A77. DOI: 10.1051/0004-6361/201423932. arXiv: 1501.07239 [astro-ph.IM].

Soubiran, C. et al. (2010). "The PASTEL catalogue of stellar parameters". In: *Astronomy & Astrophysics* 515, A111, A111. DOI: 10.1051/0004-6361/201014247. arXiv: 1004.1069 [astro-ph.SR].

Southworth, J. et al. (2020). "A multiplicity study of transiting exoplanet host stars. II. Revised properties of transiting planetary systems with companions". In: *Astronomy & Astrophysics* 635, A74, A74. DOI: 10.1051/0004-6361/201937334. arXiv: 2001.08225 [astro-ph.EP].

Stassun, Keivan G. et al. (2017). "Accurate Empirical Radii and Masses of Planets and Their Host Stars with Gaia Parallaxes". In: *The Astronomical Journal* 153.3, 136, p. 136. DOI: 10.3847/1538-3881/aa5df3. arXiv: 1609.04389 [astro-ph.EP].

Stein, A. (2020). *NOAA weather data*. URL: ftp://ftp.arl.noaa.gov/archives/gdas1/ (visited on 03/05/2021).

Talens, G. J. J. et al. (2018). "MASCARA-2 b. A hot Jupiter transiting the $m_V = 7.6$ A-star HD 185603". In: *Astronomy & Astrophysics* 612, A57, A57. DOI: 10.1051/0004-6361/201731512. arXiv: 1707.01500 [astro-ph.EP].

Tanabashi, M. et al. (2018). "Review of Particle Physics*". In: *Physical Review D* 98.3, 030001, p. 030001. DOI: 10.1103/PhysRevD.98.030001.

Temmer, M. et al. (2001). "Statistical analysis of solar Hα flares". In: *Astronomy & Astrophysics* 375, pp. 1049–1061. DOI: 10.1051/0004-6361:20010908. arXiv: astro-ph/0207239 [astro-ph].

Tipler, Paul Allen 1933 (2015). *Physik für Wissenschaftler und Ingenieure*. Ed. by Gene Mosca. 7. deutsche Auflage. Lehrbuch. Springer Spektrum. URL: http://www.gbv.de/dms/weimar/toc/787133132_toc.pdf.

Vidotto, A. A. et al. (2010). "Early UV Ingress in WASP-12b: Measuring Planetary Magnetic Fields". In: *The Astrophysical Journal Letters* 722.2, pp. L168–L172. DOI: 10.1088/2041-8205/722/2/L168. arXiv: 1009.5947 [astro-ph.EP].

Vidotto, A. A. et al. (2011). "Shock formation around planets orbiting M-dwarf stars". In: *Astronomische Nachrichten* 332, p. 1055. DOI: 10.1002/asna.201111622. arXiv: 1112.1512 [astro-ph.SR].

Vidotto, A. A. et al. (2014). "Stellar magnetism: empirical trends with age and rotation". In: *Monthly Notices of the Royal Astronomical Society* 441.3, pp. 2361–2374. DOI: 10.1093/mnras/stu728. arXiv: 1404.2733 [astro-ph.SR].

Vidotto, Aline A. (2018). "Stellar Coronal and Wind Models: Impact on Exoplanets". In: *Handbook of Exoplanets*. Ed. by Hans J. Deeg and Juan Antonio Belmonte, p. 26. DOI: 10.1007/978-3-319-55333-7_26.

Wenger, M. et al. (2000). "The SIMBAD astronomical database. The CDS reference database for astronomical objects". In: *Astronomy and Astrophysics Supplement* 143, pp. 9–22. DOI: 10.1051/aas:2000332. eprint: astro-ph/0002110.

Winter, L. M. et al. (2016). "Comparing SSN Index to X-Ray Flare and Coronal Mass Ejection Rates from Solar Cycles 22 - 24". In: *Solar Physics* 291.9-10, pp. 3011–3023. DOI: 10.1007/s11207-016-0901-6. arXiv: 1605.00503 [astro-ph.SR].

Wöllert, Maria and Wolfgang Brandner (2015). "A Lucky Imaging search for stellar sources near 74 transit hosts". In: *Astronomy & Astrophysics* 579, A129, A129. DOI: 10.1051/0004-6361/201526525. arXiv: 1506.05456 [astro-ph.SR].

Yan, Fei and Thomas Henning (2018). "An extended hydrogen envelope of the extremely hot giant exoplanet KELT-9b". In: *Nature Astronomy* 2, pp. 714–718. DOI: 10.1038/s41550-018-0503-3. arXiv: 1807.00869 [astro-ph.EP].

A&A 591, A20 (2016)
DOI: 10.1051/0004-6361/201628482

Astronomy & Astrophysics

On the nature of absorption features toward nearby stars⋆

S. Kohl, S. Czesla, and J. H. M. M. Schmitt

Hamburger Sternwarte, Universität Hamburg, Gojenbergweg 112, 21029 Hamburg, Germany
e-mail: skohl@hs.uni-hamburg.de

Received 10 March 2016 / Accepted 6 April 2016

ABSTRACT

Context. Diffuse interstellar absorption bands (DIBs) of largely unknown chemical origin are regularly observed primarily in distant early-type stars. More recently, detections in nearby late-type stars have also been claimed. These stars' spectra are dominated by stellar absorption lines. Specifically, strong interstellar atomic and DIB absorption has been reported in τ Boo.
Aims. We test these claims by studying the strength of interstellar absorption in high-resolution TIGRE spectra of the nearby stars τ Boo, HD 33608, and α CrB.
Methods. We focus our analysis on a strong DIB located at 5780.61 Å and on the absorption of interstellar Na. First, we carry out a differential analysis by comparing the spectra of the highly similar F-stars, τ Boo and HD 33608, whose light, however, samples different lines of sight. To obtain absolute values for the DIB absorption, we compare the observed spectra of τ Boo, HD 33608, and α CrB to PHOENIX models and carry out basic spectral modeling based on Voigt line profiles.
Results. The intercomparison between τ Boo and HD 33608 reveals that the difference in the line depth is 6.85 ± 1.48 mÅ at the DIB location which is, however, unlikely to be caused by DIB absorption. The comparison between PHOENIX models and observed spectra yields an upper limit of 34.0 ± 0.3 mÅ for any additional interstellar absorption in τ Boo; similar results are obtained for HD 33608 and α CrB. For all objects we derive unrealistically large values for the radial velocity of any presumed interstellar clouds. In τ Boo we find Na D absorption with an equivalent width of 0.65 ± 0.07 mÅ and 2.3 ± 0.1 mÅ in the D_2 and D_1 lines. For the other Na, absorption of the same magnitude could only be detected in the D_2 line. Our comparisons between model and data show that the interstellar absorption toward τ Boo is not abnormally high.
Conclusions. We find no significant DIB absorption in any of our target stars. Any differences between modeled and observed spectra are instead attributable to inaccuracies in the stellar atmospheric modeling than to DIB absorption.

Key words. ISM: general – stars: late-type – local insterstellar matter – ISM: lines and bands – solar neighborhood – stars: atmospheres

1. Introduction

For a long time, early-type binaries at large distances have been known to show peculiar absorption bands in their spectra. These bands cannot be attributed to stellar lines because they do not follow the Doppler shift caused by the radial motion of the binary components (Merrill 1936). Later, similar absorption bands have also been found in several hundred single stars (Duke 1951). Today, these absorption features are known as diffuse interstellar bands (DIB), which show widths typically ranging from a few mÅ up to several Å. It is assumed that the DIBs are a superposition of different components. The nature of the absorbing material is still under debate for most DIBs (Cami & Cox 2014). However, recently it has been confirmed that three DIBs can be assigned to the absorption spectrum of fullerenes (Campbell et al. 2015). There is consensus that the diffuse bands are of interstellar nature and thus the strength of individual bands depends on the chemical environment along the line of sight, implying a dependence on the stellar distance and the direction of the line of sight (e.g., Hobbs et al. 2008).

Diffuse interstellar bands are most easily observed in bright and distant objects that have few intrinsic spectral lines such as early-type supergiants, for which the equivalent widths of interstellar absorption features have been extensively studied (Herbig 1995). More recently, Hobbs et al. (2009) presented a detailed characterization of the DIB properties in the early-type supergiant HD 183143. One of the DIBs with the highest equivalent width is located at 5780.61 Å and, in the specific case of HD 183143, its shape can be modeled adequately by a single Gaussian function with a full-width at half maximum of 2.14 Å (Hobbs et al. 2009).

In late-type stars DIBs are more challenging to detect because stellar and interstellar lines are blended. Therefore DIB studies inside our Galaxy remain largely restricted to giants at large distance and high column densities of interstellar matter. Comprehensive surveys have been carried out for DIBs that are narrow and have large equivalent widths. Based on several thousand spectra, three-dimensional maps showing the distribution of the interstellar medium have been produced, e.g., using the DIBs at 6614 Å (Puspitarini et al. 2015), 8620 Å (Kos et al. 2013) and 15 272 Å (Zasowski et al. 2015). These maps typically cover distances from a few hundred parsec up to several kilo-parsec and show that the strength of the DIB absorption generally rises with distance. Moreover, Friedman et al. (2011) show that for various DIBs interstellar extinction and hydrogen absorption are correlated.

In addition to DIBs, sharp interstellar atomic absorption lines can be found. Garcia (1991) gives a compilation of the strength

⋆ The spectra are available at the CDS via anonymous ftp to cdsarc.u-strasbg.fr (130.79.128.5) or via http://cdsarc.u-strasbg.fr/viz-bin/qcat?J/A+A/591/A20

of interstellar atomic Na and Ca lines in various stellar spectra. These lines are typically much narrower than the stellar lines because they are not affected by the usual stellar line broadening mechanisms. Like DIBs they are most easily detected in distant early-type stars.

Until recently, surveys targeting the local interstellar medium were restricted to early-type stars. Lallement et al. (2003) mapped the equivalent width of the interstellar Na D lines along different lines of sight. For stars within 70 pc, the authors find no interstellar D_2 absorption line stronger than 75 mÅ, respectively, 60 mÅ for the D_1 line. Similar studies have also been carried out for the DIBs at 5780 Å and 6284 Å by Raimond et al. (2012). Out of the 24 objects in their sample with distances below 200 pc, only two show an equivalent width larger than 100 mÅ in the DIB at 5780 Å.

Studies of DIBs in late-type stars are not only hampered by ubiquitous stellar line blends and the notorious weakness of the DIBs in the spectra of nearby stars, but also by the presence of telluric lines. This is important because inaccuracies in the telluric correction contaminate the spectral signatures of the DIBs. Using the intermediate dispersion spectrograph (IDS) with a spectral resolution of ~2000 mounted at the 2.5 m Isaac Newton Telescope, Farhang et al. (2015) carried out a search for Na absorption features and DIBs in nearby late-type stars. These authors studied absorption features located at 5780, 5896, and 5890 Å and conclude that DIBs and interstellar Na can indeed be distinguished in the spectra of a number of nearby late-type stars. Farhang et al. (2015) specifically investigated the nearby star τ Boo, a triple system whose primary component hosts a planet; the stellar parameters of τ Boo are listed in Table 1. As a result of their analysis, Farhang et al. (2015) claim that τ Boo shows abnormally high interstellar absorption, and derived substantial equivalent widths for the various DIBs, viz., 137.08 ± 16.61 mÅ for the DIB at 5780 Å, and 407.16 ± 32.95 mÅ and 344.03 ± 32.62 mÅ for the equivalent widths of the interstellar Na D_2 and D_1 lines.

These equivalent widths are surprisingly large and therefore we decided to examine high-resolution spectra of τ Boo and other, similar objects. With these spectra we are in a position to revise the strength of the interstellar absorption and thus the outline of the paper is as follows: in Sect. 2.1, we present our stellar sample and summarize the stellar parameters and present our approach to correct for telluric lines in Sect. 2.2. Subsequently, we compare the spectrum of τ Boo to the spectrum of the highly similar star, HD 33608, in Sect. 2.3 and compare PHOENIX models to observed data around the location of the DIB at 5780 Å and the Na D lines in Sects. 2.4 and 2.5. We present the same analysis for the A star, α CrB, in Sects. 2.6 and summarize our findings and conclusions in Sect. 3.

2. Observations and data analysis

Our analysis is based on TIGRE spectra. TIGRE is a 1.2 m robotic telescope, located in central Mexico and equipped with an echelle spectrograph with a nominal resolution of 20 000; for further details about the instrument and telescope we refer to Schmitt et al. (2014). The raw data was reduced with the TIGRE reduction pipeline in version 2, which is based on the REDUCE package described in detail by Piskunov & Valenti (2002).

All spectra were first corrected for telluric absorption, as described in Sect. 2.2. Then, the wavelength scale was converted to a uniform reference frame to account for systematic stellar radial motion and the barycentric motion of the Earth.

Table 1. List of observed objects.

Parameter	Value	References
	τ Boo	
Spectral type	*F6IV*	1
$T_{\rm eff}$	6450 ± 150	2
log (g)	4.27 ± 0.10	2
[M/H]	0.26 ± 0.08	2
$v_{\rm rot}$[km s^{-1}]	13.0	3
$v_{\rm rad}$[km s^{-1}]	–16.03	1
Parallaxes [mas]	64.03	1
Epoch of obs. [yr]	2015.01–2015.22	
S/N at 5780 Å[a]	618	
S/N at 5892 Å[a]	763	
Total exposure time [s]	8288	
# spectra	20	
	HD 33608	
Spectral type	*F5.5IV-V*	1
$T_{\rm eff}$	6530 ± 100	2
log (g)	4.08 ± 0.07	2
[M/H]	0.22 ± 0.04	2
$v_{\rm rot}$[km s^{-1}]	15.5 ± 0.5	4
$v_{\rm rad}$[km s^{-1}]	33.90	1
Parallaxes [mas]	33.9	1
Epoch of obs. [yr]	2015.03–2015.23	
S/N at 5780 Å[a]	188	
S/N at 5892 Å[a]	234	
Total exposure time [s]	2160	
# spectra	4	
	α CrB A	
Spectral type	*A1IV*	5
$T_{\rm eff}$	9900	2
log (g)	3.89	5
[M/H]	–	
$v_{\rm rot}$[km s^{-1}]	128.8 ± 6.2	4
$v_{\rm rad}$[km s^{-1}]	1.7	1
Parallaxes [mas]	43.46	1
Epoch of obs. [yr]	2015.34	
S/N at 5780 Å[a]	569	
S/N at 5892 Å[a]	739	
Total exposure time [s]	1170	
# spectra	1	
	α CrB B	
Spectral type	*G5*	5
$T_{\rm eff}$	5800	5
log (g)	4.5	5
[M/H]	–	
$v_{\rm rot}$[km s^{-1}]	–	

Notes. [(a)] Average signal-to-noise ratio (S/N) of the coadded spectrum.

References. (1) Wenger et al. (2000); (2) Soubiran et al. (2010); (3) Han et al. (2014); (4) Głębocki & Gnaciński (2005); (5) Tomkin & Popper (1986).

2.1. The stellar sample

We used TIGRE observations of the F-type stars τ Boo and HD 33608, as well as the binary system, α CrB. τ Boo is a triple system consisting of an F-type primary, a nearby M dwarf in a long-period orbit (distance: 1.8″ in 2012), and a distant L-type

companion, whose distance was 42.6″ in 1998 (Mason et al. 2001). In principle, the spectrum of the M dwarf contaminates the primary spectrum. However, this contamination was neglected because the brightness ratio between the two stars is approximately 10^{-3} in the wavelength regions of interest.

Furthermore, the primary component also hosts a planet with a velocity semiamplitude of 466.4 m/s (Brogi et al. 2012), which corresponds to a wavelength shift of ±9.2 mÅ. Since this shift is much smaller than the width of the spectral features, it only weakly affects their shape when spectra of different epochs are averaged.

HD 33608 is very similar to the primary of the τ Boo system. In contrast to τ Boo, it is neither a member of a multiple system, nor does it host any (known) substellar companions. For this reason we chose it to validate the results obtained for τ Boo. Since τ Boo and HD 33608 have very similar stellar parameters, their intrinsic spectra are expected to be almost identical. If interstellar absorption is different toward τ Boo and HD 33608, an inter-comparison of their stellar spectra ought to reveal differences in interstellar absorption, as described in Sect. 2.3.

α CrB is a spectroscopic binary composed of an A1IV and a G5 component (Tomkin & Popper 1986). The primary is both an early-type star and a fast rotator, thus stellar lines are comparatively broad and shallow. To avoid any confusion between stellar lines of the secondary and interstellar features, a spectrum was chosen that was taken during the secondary eclipse. This avoids confusion between the stellar and interstellar Na D lines.

In total, 25 spectra of these objects were taken in the first half of 2015. Details about the objects and observations are summarized in Table 1. Most stellar parameter values were taken from the compilations of Głębocki & Gnaciński (2005) and Soubiran et al. (2010). When several values were listed for a stellar parameter, we averaged all given values, but discarded outliers. The typical spread in the listed values is smaller than 5%. As expected, the different values for the metallicity differ by up to 0.08 dex (≈20%), although outliers had already been removed. We note that the spread is generally much larger than the cited error bars, in case errors are given at all. The adopted values as well as the typical spread in the individual values (if applicable) are also listed in Table 1.

2.2. Telluric absorption correction

We corrected each raw spectrum individually for telluric absorption features using the `molecfit` code (Smette et al. 2015; Kausch et al. 2015). The `molecfit` software package creates a synthetic transmission spectrum of the Earth's atmosphere, taking into account the local temperature and humidity profiles that are delivered at a cadence of three hours by weather satellites[1]. We use this model transmission spectrum to correct the raw stellar spectrum.

In Figs. 1 and 2, we present an example to show the effect of the telluric line correction on the spectrum of α CrB. Before the correction, the shape of the broad stellar Na D lines is completely distorted by the telluric lines, while around 5780 Å the influence of the telluric lines is much smaller, as can be seen in Fig. 2. To quantify the accuracy of the telluric correction, we analyzed TIGRE spectra of α CrB. This object is particularly well suited for this task because it is a fast-rotating early-type star showing shallow, broad spectral lines, which enabled us to distinguish the narrow telluric lines with relative ease.

[1] ftp://ftp.arl.noaa.gov/archives/gdas1/

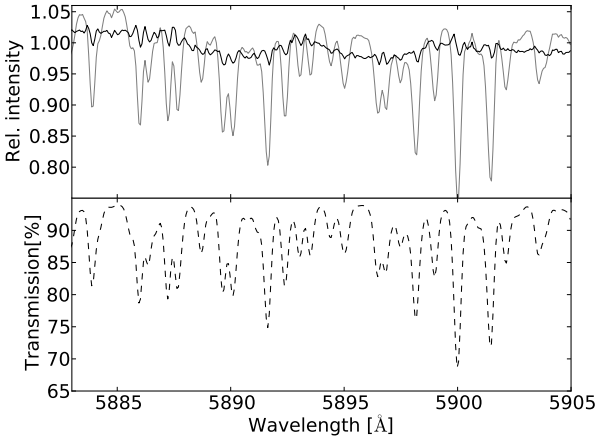

Fig. 1. *Top panel*: uncorrected stellar spectrum of α CrB (grey), corrected stellar spectrum (black). *Bottom panel*: atmospheric transmission spectrum (dashed).

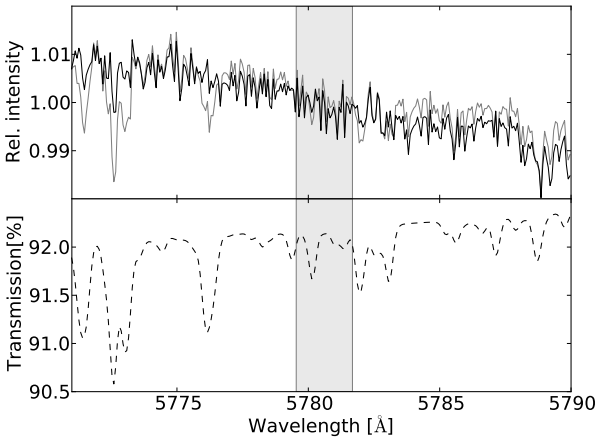

Fig. 2. *Top panel*: uncorrected stellar spectrum of α CrB (grey), corrected stellar spectrum (black). *Bottom panel*: atmospheric transmission spectrum (dashed). The shaded area denotes the position and FWHM of the putative DIB.

We tested the telluric correction in the three wavelength ranges 5770–5790 Å, 5880–5910 Å, and 7080–7140 Å. To estimate the accuracy of the correction, we modeled the stellar spectrum by a polynomial and added rotationally-broadened Gaussian absorption lines to represent the Na D lines. In the modeling, we tried out polynomials of varying degrees and found that a second-order polynomial provides satisfactory fits in all the wavelength ranges considered; polynomials of higher order did not improve the fit significantly. We note that in the modeling, we split the wavelength range from 7080 to 7140 Å into two subranges from 7080 to 7116 Å and 7116 to 7140 Å. We then used the resulting fit to normalize the spectrum and calculated the standard deviation to estimate the quality of the telluric correction. Our results are summarized in Table 2. According to Smette et al. (2015), the depth of an unsaturated telluric line can be modeled with an accuracy that is better than 2%. A comparison with our results shows that the selected wavelength ranges the accuracy is generally consistent or even better than this value.

Table 2. Deviations between continuum model and data

Wavelength range [Å]	std. deviation[%]	Model
5770–5790	0.3	polynomial
5880–5910	1.0	absorption lines
7080–7140	0.4	polynomial

As a consequence, the corrected stellar spectrum has an additional systematic error component owing to the telluric correction. In contrast to the statistical noise, this error term cannot be suppressed by more observations. The total error budget is on the order of the magnitude of the standard deviation listed in Table 2. The final S/N after telluric correction is about 100 in the wavelength range of the Na D lines and around 300 at 5780 Å.

2.3. Intercomparison of HD 33608 and τ Boo

We compared the spectra of HD 33608 and τ Boo to identify any differences between these two stars. Both stars have very similar values of effective temperature, surface gravity, metallicity, and are fast rotators (see Table 1 for details). However, the stars are located at different lines of sights. The distance to HD 33608 is almost twice the distance of τ Boo, therefore no correlation of the distribution and column depth of interstellar material is expected. This makes it highly unlikely that the strength of interstellar features is identical in the spectra of both objects.

The spectra around 5780 Å are shown in the top panel of Fig. 3; we normalized both spectra independently by adjusting the median flux between 5750 Å and 5810 Å to unity. From Fig. 3, it is clear that the putative DIB is blended by a stellar Fe II line located at 5780.37 Å and an Fe I line at 5780.60 Å[2]. In general, we find good agreement between both spectra. We note that none of the spectra has been rotationally broadened. Specifically, both figures show that the stellar lines of τ Boo are slightly deeper than the lines of HD 33608. Plausible explanations for this discrepancy are an increased metallicity in τ Boo and a slower rotation rate of τ Boo, or both.

To examine the differences between the spectrum of HD 33608 and τ Boo, we subtracted both spectra from each other (see lower panel of Fig. 3). Subsequently, we fitted a Gaussian at the expected position of the DIB. A variation in the line centroid was allowed to account for any heliocentric motion of the interstellar gas. According to Welsh et al. (2010), the heliocentric motion is rarely found to be larger than 30 km s^{-1} in the interstellar medium within 300 pc. For this reason this value was adopted as an upper limit. Furthermore, the line width was allowed to be smaller than 2.14 Å, the value measured in the spectrum of the distant supergiant HD 183143 (Hobbs et al. 2009), which we used as an upper bound. The chemical constituents of the DIBs are unknown and thus the exact intrinsic width of the absorption feature. In case of nearby stars, we expect a lower number of interstellar clouds along the line of sight. Since each cloud has its own heliocentric velocity and chemical composition, one expects a broader absorption feature in the spectra of distant stars, while sharper features may be present in the spectra of closer stars.

To quantify the differences in lines without any expected interstellar contributions, we also applied the fitting procedure to the neighboring stellar lines, which ought to be free of DIBs according to Hobbs et al. (2009). In this case, we allowed the central wavelength to vary by ±2 Å and enforced no constraints on the line width or equivalent width. Our results are given in the upper part of Table 3. They show that the feature at 5780 Å is not exceptionally broad, and therefore likely attributable to intrinsic differences between the stellar spectra.

To evaluate whether an additional broad DIB component is present, the fitting procedure was repeated by adding an additional component located at 5780.61 Å with a fixed FWHM of 2.14 Å. The results of this fitting procedure can be found in the lower part of Table 3. A comparison of our fits shows that the results at 5775 and 5785 Å are only marginally affected by this additional component, but the results for the stellar line at 5781 Å differ. In particular, it appears that its equivalent width increased, counterbalancing the influence of the broad component. The equivalent width of the putative DIB component is negative, implying that, if anything, the absorption of the interstellar medium is higher along the line of sight toward HD 33608. However, the presence of any difference in the interstellar absorption is not statistically significant. Depending on the adopted model (with or without additional DIB component) we obtain different values for the difference in the strength of the possible DIB absorption feature. At any rate, our results show that the difference in interstellar absorption must be less than 11.29 mÅ with a confidence of 3σ.

Table 3. Parameters of the best-fitting models.

Central wavelength [Å]	σ [Å]	EW [mÅ]
Without additional DIB component		
5774.88	0.112 ± 0.034	3.95 ± 1.02
5780.57	0.270 ± 0.062	6.85 ± 1.48
5784.98	0.248 ± 0.047	7.18 ± 1.37
With additional DIB component		
5774.88	0.113 ± 0.034	3.96 ± 1.04
5780.57	0.308 ± 0.074	9.10 ± 3.38
5780.61	2.14	–4.39 ± 4.87
5784.98	0.249 ± 0.048	7.24 ± 1.38

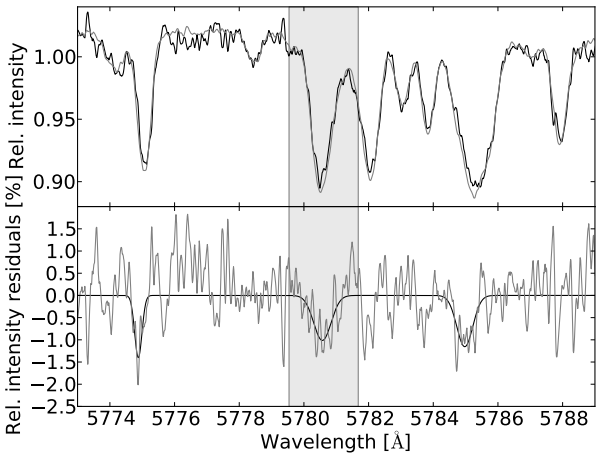

Fig. 3. *Top panel*: comparison between τ Boo (gray) and HD 33608 (black). *Bottom panel*: comparison of residuals (gray) and best-fitting DIB (black). The shaded area denotes the position and FWHM of the putative DIB.

[2] http://physics.nist.gov/PhysRefData/ASD/lines_form.html

Table 4. Influence of stellar parameters on modeled flux of F-stars.

Parameter	Default value	Range	max ($\Delta F(\lambda)$)
$T_{\rm eff}$[K]	6,400	6,300...6,600	1.7%
$\log(g)$	4.0	4.0...4.5	0.6%
[M/H]	0.0	0.0...0.5	6.7%
$v_{\rm rot}$[km s^{-1}]	15.5 km s^{-1}	13.0...17.0	0.4%
$v_{\rm rad}$[km s^{-1}]	0.0 km s^{-1}	0.0...3.0	0.8%
R	2.0×10^4	1.8×10^4...2.2×10^4	0.2%

2.4. Comparison between data and PHOENIX templates for τ Boo and HD 33608

The method applied in the preceding section is only sensitive to differences in the strength of the interstellar absorption. Following the approach adopted by Farhang et al. (2015), we compared our TIGRE spectra to synthetic stellar models to obtain an absolute value of the equivalent width of interstellar absorption. We specifically compared PHOENIX atmosphere models in the wavelength region between 5750 and 5810 Å to the observed TIGRE spectra. The atmosphere models were rotationally broadened and convolved with the instrumental resolution of TIGRE ($R \sim 20\,000$) and that of the IDS ($R \sim 2000$) used by Farhang et al. (2015). To disentangle interstellar and stellar features, the synthetic template was subtracted from the stellar spectrum. Differences between the observed and synthetic spectrum can then either be ascribed to inaccuracies in the model or to the actual presence of interstellar matter.

2.4.1. Choosing the template

A precalculated atmospheric model grid can be found in the Göttigen Spectral Library, which provides densely sampled synthetic spectra for a wide range of effective temperatures, surface gravities, and metallicities (Husser et al. 2013). To assess if the model spectra have to be interpolated, the influence of each model parameter on the stellar template was quantified. Furthermore, the influence of the spectrograph's resolution, R, as well as discrepancies caused by an incorrect radial velocity have been taken into account. We modeled the effect of changing the spectral resolution and the radial velocity on the resulting flux. The spectral resolution of the individual exposures varied slightly between 19 000 and 21 000 from one exposure to the next during the period of data acquisition. For all other parameters, see Table 1 and references therein.

The wavelength-dependent normalized flux for a certain stellar PHOENIX model can be written as $F(\lambda, T_{\rm eff}, \ldots, R)$, where λ denotes wavelength and the other variables are the required model parameters. For two adjacent parameter values p_1 and p_2 on the grid we define

$$\Delta F(\lambda) := |F(\lambda, \ldots, p_2, \ldots) - F(\lambda, \ldots, p_1, \ldots)|,$$

with all other model parameters kept fixed. The default values for each parameter, as well as their upper and lower values, are listed in Table 4. The influence of each model parameter has been evaluated over a range that is larger than the scatter listed in Table 1 and the results are listed in Table 4. Between adjacent grid points, the stellar template is most sensitive to metallicity.

The effective temperature and surface gravity, as listed in Table 1, were used to choose the best-matching stellar model. Since the quality of the template depends mostly on metallicity, two model spectra with different metallicities were interpolated to obtain a spectrum with a metallicity equal to the mean of the literature values. Since the scatter is substantial, we checked if this metallicity leads to the best model. To that end, the metallicity was varied in steps of 0.0025 between 0.0 and 0.5. For each step an interpolated spectrum was obtained and χ^2 ([M/H]) was evaluated. Finally, we determined the best-fit metallicity by searching for min $\left(\chi^2([{\rm M/H}])\right)$. The associated value was found to be consistent with the literature values to within the error bars.

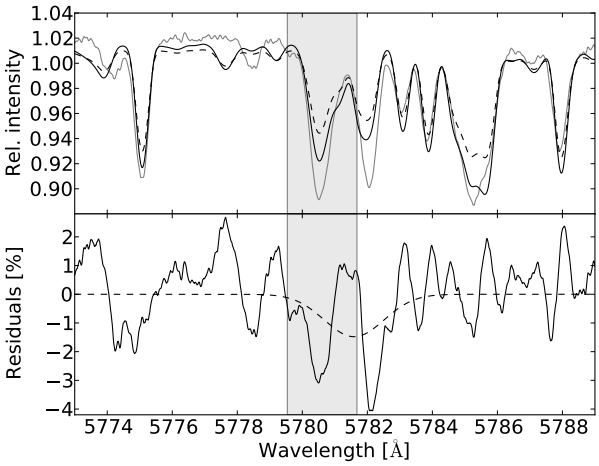

Fig. 4. *Top panel*: comparison between observed spectrum of τ Boo (gray) and PHOENIX models with best-fitting [M/H] (solid black) resp. [M/H] = 0 (dotted black). *Bottom panel*: differences between best-fitting model and data (solid line). Best-fitting Gaussian (solid line). The shaded area denotes the position and FWHM of the putative DIB.

2.4.2. Analysis of the residuals

After subtraction of the PHOENIX template, we fitted a Gaussian function that was expected to match the shape of the DIB to the residual spectrum. The width and position of the centroid were taken from Hobbs et al. (2009); these values are valid for HD 183143. Since the interstellar medium toward other objects may have a different radial velocity structure the centroid position was allowed vary. In the modeling, the continuum was approximated by a linear function. The resulting equivalent widths can be found in Table 5 and an example is shown in Fig. 4. Clearly, the depth of the observed spectral line around 5780.6 Å is deeper than the model prediction, suggesting the possible presence of a DIB. However, as can also be seen in Fig. 4, the observed line at 5782 Å is also deeper than the model prediction, although no DIB is known at this position (Hobbs et al. 2009). Furthermore, the pronounced influence of the metallicity on the model spectrum is evident. Apart from metallicity effects the spectra are also affected by inaccuracies of the atomic data used by PHOENIX to generate the models. Both problems contribute to the substantial offset between model and observation and the resulting systematic errors in the fit results.

For this reason, we emphasize that the results given in Table 5 are not presumed to represent DIB features but rather demonstrate the expected magnitude of systematic inaccuracies arising from the fact that the best-fitting models predominantly lead to radial velocities larger than 30 km s^{-1} for the DIB component, which is highly unlikely in the solar neighborhood (Welsh et al. 2010).

Table 5. Fit results for putative DIB feature.

Object	R	EW[mÅ]	RV[km s^{-1}]
HD 33608	20 000	41.7 ± 0.9	176.3
τ Boo	20 000	34.0 ± 0.3	35.0
α CrB	20 000	6.4 ± 1.4	165.9
HD 33608	2000	51.2 ± 1.8	85.6
τ Boo	2000	52.8 ± 1.0	27.2
α CrB	2000	8.4 ± 6.1	129.6

Table 6. Fit results for Na D lines.

Object	EW[mÅ]	RV[km s^{-1}]	$EW_{\rm lit}$[mÅ]	Ref.
		Na D_2		
HD 33608	3.57 ± 0.63	–25.4 ± 0.5	–	–
τ Boo	0.65 ± 0.07	9.9 ± 0.5	–	–
α CrB	2.83 ± 0.79	13.0 ± 1.7	–	–
		Na D_1		
HD 33608	–[a]	–[a]	–	–
τ Boo	2.30 ± 0.10	9.9 ± 0.5	–	–
α CrB	–[a]	–[a]	<2.50	1

Notes. [(a)] No such feature could be found at the presumed location.
References. (1) Welsh et al. (2010).

2.4.3. Analysis at low spectral resolution

To assess the influence of the spectrograph's resolution on the derived results, the observed spectra were numerically broadened to a resolution of 2000 and the data reduction, as described above, was also applied to these lower resolution spectra. Here, we used the same synthetic templates also adopted in the context of the high-resolution analysis. The results of this analysis are also given in Table 5. With a degraded resolution the resulting equivalent widths are larger by between 20% and up to more than 50% compared to the high-resolution analysis. Again, the radial velocities of the putative DIB components are unrealistically large, with only τ Boo being somewhat of an exception.

2.5. Interstellar Na D lines in τ Boo and HD 33608

In addition to the unknown constituents responsible for the DIB absorption, the interstellar space is filled with atomic gas, which manifests itself by sharp absorption lines unique for each chemical element. In the visible wavelength range, strong absorption lines can be found for instance from sodium, with regard to the Na D lines at 5889.95 and 5895.92 Å. In the case of F-type stars, strong stellar lines are also expected at this position. Since τ Boo and HD 33608 are fast rotators, substantial rotational line broadening is present. In contrast, the velocity dispersion in the interstellar Na is expected to be small in the solar neighborhood and thus the absorption line is narrow, which enables the stellar and interstellar contribution to be distinguished.

We approximated the stellar lines by a Voigt profile. The data, together with the best-fitting model, are shown in the upper panels of Fig. 5. Based on these models, we can determine the strength of the stellar Na D lines. While visual inspection of the residuals shown in the lower panels of Fig. 5 demonstrates good agreement between model and data, there is a W-shaped mismatch between model and data in the region around the D_2 line. This type of mismatch indicates that the data deviates systematically from a Voigt profile.

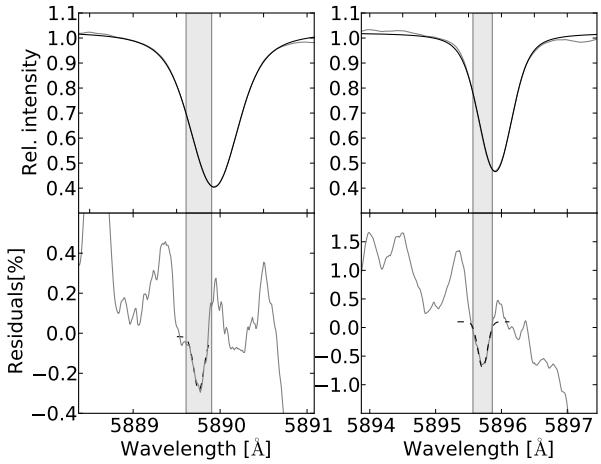

Fig. 5. *Top panel*: comparison between observed spectrum of τ Boo (gray) and best-fitting Voigt profile (black). *Left*: Na D_2 line, *right*: Na D_1 line. *Bottom panel*: differences between model and data (solid line). Best-fitting Voigt profile (dotted line). The shaded area denotes the position and FWHM of the putative Na D lines.

An interstellar component, if present, is expected to only cause a small deviation from the Voigt model. To search for possible interstellar lines, we searched the residuals for the largest visible structure whose width is compatible with an instrumentally broadened interstellar line. This width is solely determined by the instrumental line profile for which we assumed a Gaussian with a FWHM of 0.29 Å. Furthermore, it is assumed that all residuals pertaining to the potential interstellar feature are negative. In the lower panels of Fig. 5, we show that the agreement between model and data is better in the region around the D_2 line; in this region the residuals do not exceed 0.5%. In contrast, around the D_1 line the residuals can be as large as 1.6%. Furthermore, the D_2 line is more symmetric than the D_1 line. An inspection of PHOENIX models shows that the D_1 line is more strongly contaminated by other weak stellar lines. For this reason, the feature was first searched in the D_2 line and then at the same RV shift in the D_1 line. This type of feature was found around 5890 Å, and 5896 Å in the case of τ Boo. The radial velocity of the feature is between 9 km s^{-1} and –26 km s^{-1}. Inside the Na D_2 line, we were always able to locate a feature whereas, in most cases, we could not find it inside the D_1 line. We summarize our results in Table 6.

We also carried out an identical examination for HD 33608. First, we identified a potential feature in the D_2 line (see Table 6) and then attempted to find a corresponding feature at the same radial velocity shift in the D_1 line. However, in the case of HD 33608, we could not identify such feature in the D_1 line.

2.6. Interstellar absorption in α CrB

For α CrB, we also carried out a search for the DIB at 5780 Å and interstellar Na D absorption by a comparison with PHOENIX template spectra, as described in Sects. 2.4 and 2.5. However, in α CrB we considered it unnecessary to accurately quantify the influence of the stellar parameters on the template because the template only weakly depends on the chosen model, since α CrB

is a hot star and a rapid rotator. Since hot stars have weak metallic lines that are, moreover, rotationally broadened, the spectrum of α CrB shows only few distinguishable stellar lines. In addition, the noise of the spectrum is too high to distinguish the small differences (about 2%) in the templates that are caused by the variations in the stellar parameters. The results are also given in Table 5, which indicates that by far the lowest value for the equivalent width is found for α CrB. However, the results for the radial velocity shift of the DIB component in α CrB are unreasonable.

The analysis is similar to that described in Sect. 2.5. The shape of the stellar Na D lines is dominated by the fast stellar rotation. For that reason a rotationally broadened Gaussian was fitted to model the stellar lines instead of a Voigt profile. The results for α CrB can be found in Table 6. In the region of the Na D_2 line, we found a small absorption feature at a reasonable wavelength shift. In contrast, inside the stellar D_1 line we are not able to confirm the results that are published in literature.

3. Discussion and conclusions

Motivated by the claims of Farhang et al. (2015), who measured the equivalent widths of DIBs in excess of 100 mÅ, we have analyzed high-resolution spectra of the nearby stars α CrB, HD 33608, and τ Boo to search and study possible interstellar absorption in the Na D lines and at a strong DIB at 5780 Å. We applied two methods: as a first step, we carried out an intercomparison of the spectra of HD 33608 and τ Boo for a differential analysis of the two stars. At the putative position of the DIB, we obtain a difference in line depth of 6.85 ± 1.48 mÅ, but also in neighboring regions of the spectra such differences of a few mÅ can be found, which are typically located in the cores of stellar absorption lines. Neither the width of the feature at 5781 Å nor its equivalent width show any peculiarities when compared to a neighboring absorption feature at 5785 Å, although no DIB has been observed by Hobbs et al. (2009) at these locations. The only feature that differs significantly in width and equivalent width is at 5775 Å. To rule out a possible broad and shallow DIB component, we repeated the fitting with an additional component with fixed FWHM and obtained results that are identical within the error bars. We are thus lead to the conclusion that the differences between the spectra can be attributed to intrinsic stellar properties and that the interstellar chemical environment of both objects must be very similar.

As a second step we therefore carried out a closer examination using stellar atmosphere models. The comparison between PHOENIX model and data reveals that the lines at 5780 Å and 5782 Å have been modeled too shallow. The difference in equivalent width is 41.7 mÅ and 34.0 mÅ for the F-stars and 6.4 mÅ for the A-star. If we degrade the resolution to 2000, the equivalent width is 51.2 mÅ and 52.8 mÅ for the F-stars and 8.4 mÅ for the A-star. Furthermore, our approach requires a velocity of the interstellar medium on the order of 35 km s^{-1}.

Both methods show that differences are not only present at the assumed locations of DIBs but also in other regions where no DIBs are known. This leads us to the conclusion that the discrepancies between model and data cannot be ascribed to interstellar features, but rather to inaccuracies of stellar models in that stellar absorption lines are incorrectly modeled. The reasons for the incorrect modeling can be grouped into two categories: inaccuracies in stellar modeling and incorrect stellar parameters. For instance, the catalog of Soubiran et al. (2010) lists a wide range of metallicities for each object. Depending on what value is adopted, this will affect the stellar model. Inaccuracies in atomic line parameters will affect the shape and depth of a stellar line. Furthermore, the radial velocity of the derived DIB component is fairly high, these values have only been found rarely and are unusual for nearby stars.

Our results are therefore at variance with those by obtained Farhang et al. (2015). Equivalent widths in excess of 100 mÅ are not confirmed with our data. Of course, we cannot rule out the possible presence of DIBs. However, if present, their equivalent widths must be smaller than the inaccuracies of the stellar line modeling and we conclude that the equivalent width of any DIB in the sightline of τ Boo is below 34.9 mÅ with a confidence of 3σ.

Acknowledgements. This research has made use of the SIMBAD database, operated at CDS, Strasbourg, France, of the Washington Double Star Catalog maintained at the US Naval Observatory, of the Exoplanet Orbit Database and the Exoplanet Data Explorer at exoplanets.org, and of the NIST Atomic Spectra Database, maintained at the National Institute of Standards and Technology, Gaithersburg, MD.

References

Brogi, M., Snellen, I. A. G., de Kok, R. J., et al. 2012, Nature, 486, 502
Cami, J., & Cox, N. L. J. 2014, in The Diffuse Interstellar Bands, IAU Symp., 297
Campbell, E. K., Holz, M., Gerlich, D., & Maier, J. P. 2015, Nature, 523, 322
Duke, D. 1951, ApJ, 113, 100
Farhang, A., Khosroshahi, H. G., Javadi, A., et al. 2015, ApJ, 800, 64
Friedman, S. D., York, D. G., McCall, B. J., et al. 2011, ApJ, 727, 33
Garcia, B. 1991, A&AS, 89, 469
Głębocki, R., & Gnaciński, P. 2005, in 13th Cambridge Workshop on Cool Stars, Stellar Systems and the Sun, eds. F. Favata, G. A. J. Hussain, & B. Battrick, ESA SP, 560, 571
Han, E., Wang, S. X., Wright, J. T., et al. 2014, PASP, 126, 827
Herbig, G. H. 1995, ARA&A, 33, 19
Hobbs, L. M., York, D. G., Snow, T. P., et al. 2008, ApJ, 680, 1256
Hobbs, L. M., York, D. G., Thorburn, J. A., et al. 2009, ApJ, 705, 32
Husser, T.-O., Wende-von Berg, S., Dreizler, S., et al. 2013, A&A, 553, A6
Kausch, W., Noll, S., Smette, A., et al. 2015, A&A, 576, A78
Kos, J., Zwitter, T., Grebel, E. K., et al. 2013, ApJ, 778, 86
Lallement, R., Welsh, B. Y., Vergely, J. L., Crifo, F., & Sfeir, D. 2003, A&A, 411, 447
Mason, B. D., Wycoff, G. L., Hartkopf, W. I., Douglass, G. G., & Worley, C. E. 2001, AJ, 122, 3466
Merrill, P. W. 1936, ApJ, 83, 126
Piskunov, N. E., & Valenti, J. A. 2002, A&A, 385, 1095
Puspitarini, L., Lallement, R., Babusiaux, C., et al. 2015, A&A, 573, A35
Raimond, S., Lallement, R., Vergely, J. L., Babusiaux, C., & Eyer, L. 2012, A&A, 544, A136
Schmitt, J. H. M. M., Schröder, K.-P., Rauw, G., et al. 2014, Astron. Nachr., 335, 787
Smette, A., Sana, H., Noll, S., et al. 2015, A&A, 576, A77
Soubiran, C., Le Campion, J.-F., Cayrel de Strobel, G., & Caillo, A. 2010, A&A, 515, A111
Tomkin, J., & Popper, D. M. 1986, AJ, 91, 1428
Welsh, B. Y., Lallement, R., Vergely, J.-L., & Raimond, S. 2010, A&A, 510, A54
Wenger, M., Ochsenbein, F., Egret, D., et al. 2000, A&AS, 143, 9
Zasowski, G., Ménard, B., Bizyaev, D., et al. 2015, ApJ, 798, 35

A&A 619, A96 (2018)
https://doi.org/10.1051/0004-6361/201833567

Astronomy & Astrophysics

HD 189733 b: bow shock or no shock?⋆

S. Kohl, M. Salz, S. Czesla, and J. H. M. M. Schmitt

Hamburger Sternwarte, Universität Hamburg, Gojenbergweg 112, 21029 Hamburg, Germany
e-mail: skohl@hs.uni-hamburg.de

Received 4 June 2018 / Accepted 23 August 2018

ABSTRACT

Context. Hot Jupiters are surrounded by extended atmospheres of neutral hydrogen. Observations have provided evidence for in-transit hydrogen Hα absorption as well as variable pre-transit absorption signals. These have been interpreted in terms of a bow shock or an accretion stream that transits the host star before the planet.
Aims. We test the hypothesis of planetary-related Hα absorption by studying the time variability of the Hα and stellar activity-sensitive calcium lines in high-resolution TIGRE (Telescopio Internacional de Guanajuato Robótico Espectroscópico) spectra of the planet host HD 189733.
Methods. In the framework of an observing campaign spanning several months, the host star was observed several times per week randomly sampling the orbital phases of the planet. We determine the equivalent width in the Hα and Ca IRT(calcium infrared triplet) lines, and subtract stellar rotationally induced activity from the Hα time series via its correlation with the IRT evolution. The residuals are explored for significant differences between the pre-, in-, and out-of-transit phases.
Results. We find strong stellar rotational variation with a lifetime of about 20–30 days in all activity indicators, but the corrected Hα time series exhibits no significant periodic variation. We exclude the presence of more than 6.2 mÅ pre-transit absorption and 5.6 mÅ in-transit absorption in the corrected Hα data at a 99% confidence level.
Conclusions. Previously observed Hα absorption signals exceed our upper limits, but they could be related to excited atmospheric states. The Hα variability in the HD 189733 system is dominated by stellar activity, and observed signals around the planetary transit may well be caused by short-term stellar variability.

Key words. planets and satellites: atmospheres – planets and satellites: gaseous planets – planets and satellites: individual: HD 189733

1. Introduction

Today our knowledge about extrasolar planets is not only limited to basic parameters like mass and radius, but information on the chemical composition has also been derived from transmission spectroscopy in multiple cases (e.g., Sing et al. 2016). During transit, a planetary atmosphere causes excess absorption in atomic or molecular lines. In the extended atmospheres of large close-in gas planets, hydrogen remains mostly neutral and in the ground state, despite equilibrium temperatures of several thousand Kelvin, resulting in strong hydrogen line absorption. In fact, observations verified Lyα excess absorption around the transits of HD 189733 b (Lecavelier Des Etangs et al. 2010; Bourrier et al. 2013), HD 209458 b (Vidal-Madjar et al. 2003; Ehrenreich et al. 2008), and GJ 436 b (Kulow et al. 2014; Ehrenreich et al. 2015). For the aforementioned planets, transit depths of more than 10% were measured in the Lyα line wings, in contrast to broadband optical transit depth measurements of 0.6% for GJ 436 b and 2.5% for HD 189733 b (Han et al. 2014). Clearly, these planets must host extended envelopes of hydrogen.

These close-in planets are exposed to extreme high-energy irradiation levels, which are thought to drive a significant loss of atmospheric material through an energy-limited planetary wind (Watson et al. 1981; Lammer et al. 2003; Salz et al. 2016). Such a wind can carry considerable amounts of neutral hydrogen into elevated atmospheric layers. For example, interactions with the stellar wind could increase the local excitation level, which would lead to enhanced absorption in the Balmer lines. In contrast to the Lyα line, the Balmer series can be studied with ground-based telescopes equipped with medium-resolution spectrographs covering the visible wavelength range. Particularly, excess hydrogen Hα absorption has been claimed to occur around the transit of HD 189733 b (Jensen et al. 2012; Cauley et al. 2015).

Here we investigate possible Hα absorption in the HD 189733 system with a very general observing approach. In Sect. 2, we present the properties of HD 189733 and introduce the concept of a bow shock. In Sect. 3 we describe our dataset and go through the data reduction steps. We present our results and conclusions in Sects. 4 and 5.

2. The case of HD 189733 b

The K dwarf HD 189733 is orbited by a Jupiter-sized planet in 2.2 days, a so-called hot Jupiter. The host star is considerably more active than the Sun, although with a presumed age of 5.3 ± 3.8 Gyr it is not a young star (Bonfanti et al. 2016); we list the stellar and planetary properties in Table 1. The high level of stellar irradiation in the close planetary orbit leads to a bloated planetary atmosphere, which has been subject to intensive studies because of the stellar brightness (m_V = 7.65). For example, Boisse et al. (2009) present a spectroscopic observing campaign, which was carried out with the high-resolution spectrograph

⋆ Full Table 2 is only available in electronic form at the CDS via anonymous ftp to cdsarc.u-strasbg.fr (130.79.128.5) or via http://cdsarc.u-strasbg.fr/viz-bin/qcat?J/A+A/619/A96

Table 1. Parameters of HD 189733 and its planet b.

Parameter	Value	References
HD 189733		
m_V	7.65	1
M_V–M_B	0.93	1
Spectral type	K0V + M4V	1
T_{eff}[a]	5052 ± 46	2
$\log(g)$[a]	4.49 ± 0.13	2
(M/H)[a]	0.02 ± 0.02	2
$v_{rot} \sin(i)$(km s^{-1})	3.5 ± 1.0	3
Rotation period (d)	11.953 ± 0.009	11
v_{rad}(km s^{-1})	-2.55 ± 0.21	1
Parallaxes (mas)	50.40 ± 0.22	1
$\log(R'_{HK})$	$-4.524 \cdots -4.458$	9
age (Gyr)	5.30 ± 3.80	10
Mass ($M_\odot$)	0.846 ± 0.049	6
Radius ($R_\odot$)	0.805 ± 0.016	6
HD 189733 b		
Planet mass [M_{Jup}]	1.144 ± 0.056	3
Semi-major axis (AU)	0.03100 ± 0.00062	3
Transit midpoint (MJD)	$53955.0 \cdots \pm 8.8 \times 10^{-6}$	4
Orbital period (d)	$2.2 \cdots \pm 7.7 \times 10^{-8}$	4
Planetary radius (R_{Jup})	1.138 ± 0.027	3
Duration of transit (h)	1.8036 ± 0.0023	4
Transit depth (%)	2.413 ± 0.003	8
Planetary density (g cm^{-3})	$0.963^{+0.088}_{-0.079}$	3
Observations		
Epoch of obs. (yr)	2017.32–2017.88	
Exposure time (s)	≈700–2500	
S/N at Hα	≈85 (line core)	
No. of spectra	108	

Notes. [(a)]When several values were listed for a stellar parameter, we averaged all the given values, however discarding outliers.
References. (1) Wenger et al. (2000); (2) Soubiran et al. (2010); (3) Han et al. (2014); (4) Baluev et al. (2015); (5) Gray et al. (2006); (6) Głębocki & Gnaciński (2005); (7) Akeson et al. (2013); (8) Morello et al. (2014); (9) Pace (2013); (10) Bonfanti et al. (2016); (11) Henry & Winn (2008).

SOPHIE (Spectrographe pour l'Observation des Phénomènes des Intérieurs stellaires et des Exoplanètes) mounted on the 1.93-m telescope at the Observatoire de Haute-Provence, to study the impact of stellar activity on RV (radial velocity) measurements. The authors concluded that the activity indices Ca H&K, He I, and Hα show a periodicity close to the stellar-rotation period of 12 days (Henry & Winn 2008). Boisse et al. also searched for planetary signals with a period of 2.2 days in these lines. The Hα variability was not found to change with the planetary orbital phase on a level of 2% over a 0.678 Å passband.

Later observations studied single transits in detail. Jensen et al. (2012) show a statistically significant Hα excess absorption signal during the transit of the hot Jupiter. Recently, Cauley et al. (2015) studied the planetary transit also covering several hours before and after the transit, and found Hα excess absorption during the pre-transit phase as deep as 10 mÅ and lasting about 2 h. In contrast, no absorption was found in the cores of the chromospheric activity indicators Ca H&K. Therefore, they concluded that the observed feature is related to an extended planetary atmosphere and not to stellar activity, and speculate that the transit of a bow shock could precede the transit of the planetary disk.

The presence of pre-transit absorption seems to be confirmed by additional data (Cauley et al. 2016), where an excess absorption depth of 7 mÅ over a duration of 2.5 h was detected in the pre-transit phase. Cauley et al. interpret this signal as accretion clumps spiraling toward the star, but also point out that this interpretation has serious limitations. Further investigations by Barnes et al. (2016) challenge the results and note that the Hα variations are well correlated with the Ca H&K lines, indicating that the Hα time series are dominated by stellar activity. Yet, additional out-of-transit time series taken by Cauley et al. (2017) show significantly lower Hα residual equivalent width than the previously presented pre-transit signals. Thus, in summary, the origin of the Hα features has to be treated as an open issue.

3. Observations and data reduction

3.1. Observations

To test the nature of the Balmer line absorption features in HD 189733, we initiated an observing campaign to monitor chromospheric and possibly planet-induced variations. The campaign was performed with our 1.2 m TIGRE (Telescopio Internacional de Guanajuato Robótico Espectroscópico) telescope located in the central Mexican highlands. TIGRE is equipped with a spectrograph with a nominal resolution of 20 000. For details about the spectrograph and telescope, we refer to Schmitt et al. (2014). The brightness of the host star allows us to reach a signal-to-noise ratio (S/N) of about 84 inside the Hα line core with typically 900 s exposures. The actual exposure times were varied according to the observing conditions to reach the required S/N.

We typically obtained several spectra of HD 189733 per week, randomly sampling the stellar rotation phase and the planetary orbit. Because the pre- and in-transit phases cover only a small fraction of the planetary orbit, we randomly increase the sampling rate around the transit phase. Therefore, during transit nights our goal was to take three spectra; if no transit was expected, we took a single exposure per night. The target is only observable from spring to fall and the weather is generally more unstable during the summer, causing larger observation gaps (see Fig. 1). Nevertheless, this is one of the most extensive spectral time series of HD 189733 to our knowledge. In total we acquired 108 spectra; the precise observing dates are listed in Table 2.

The raw CCD (charge-coupled device) frames are automatically reduced by the TIGRE reduction pipeline (Mittag et al. 2010), currently in version 3.1; it is based on the REDUCE package described in detail by Piskunov & Valenti (2002).

3.2. Telluric correction

In the visible and near infrared wavelength range, molecules like O_2 and H_2O cause telluric absorption that depends on the airmass and meteorological parameters such as relative humidity. To achieve the data quality required for the study of planetary absorption, our first step is the correction of the telluric absorption lines, for which we use the ESO (European Southern Observatory) code molecfit (Smette et al. 2015). It works as follows: first, we choose wavelength regions that are heavily affected by telluric lines and show the least stellar lines. The wavelength ranges we use and the dominant telluric absorbers are given in Table 3. Strong stellar lines in these regions are masked.

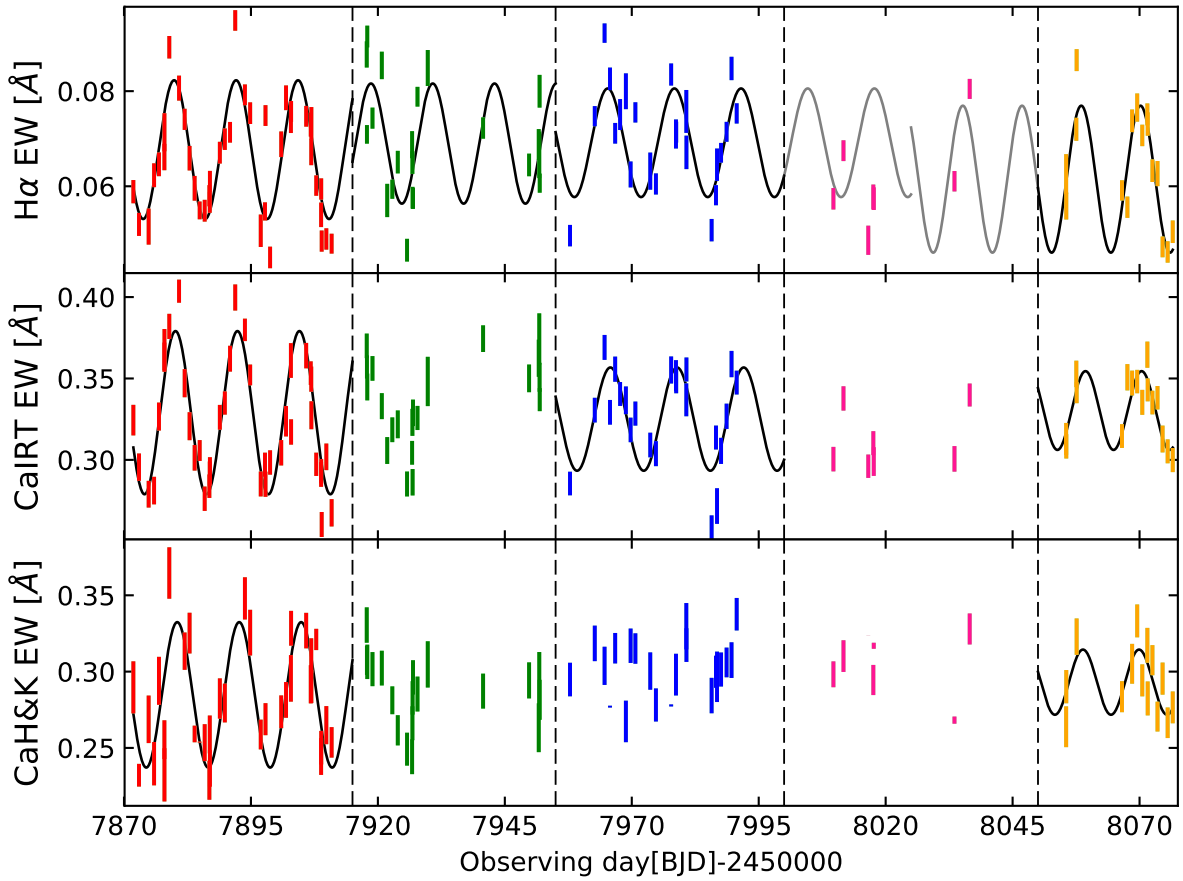

Fig. 1. Hα, Ca IRT, and Ca H&K excess equivalent width versus time. The thin black lines are the maximum power sine waves derived from our periodogram analysis and thin gray lines represent extrapolations to emphasize phase jumps. Vertical dashed lines denote the different subsamples. If the rotation period of the best-fit solution deviates significantly from the literature value of 12 days, we do not plot it. In case of Ca H&K, we removed two outliers.

Table 2. Observed excess equivalent width in different lines.

BJD−2.4·10^6	Ca H&K [mÅ]	Ca IRT [mÅ]	Hα [mÅ]
57871.84115	290 ± 17	324 ± 9	59 ± 2
57872.95254	232 ± 7	296 ± 8	52 ± 2
57874.85382	269 ± 16	279 ± 8	52 ± 4
57875.92284	240 ± 14	281 ± 8	62 ± 3
57876.88535	294 ± 16	327 ± 9	65 ± 2
57877.95397	255 ± 13	363 ± 9	66 ± 3

Notes. Here we give only the first lines. The whole table is only available at the CDS.

Table 3. Wavelength ranges for telluric column density fitting.

Dominant molecule	Begin (Å)	End (Å)
O_2 (*B* band)	6860	6940
H_2O	7160	7340
O_2 (*A* band)	7590	7690
H_2O	8120	8340

Molecfit calculates a synthetic telluric absorption spectrum based on the HITRAN (high-resolution transmission) molecular database (Rothman et al. 2009). The code takes into account the spectrograph's resolution, and local airmass, temperature, pressure, and humidity profiles from model atmospheres (Noll et al. 2013). The initially derived atmospheric transmission spectrum is the starting point of a χ^2 minimization that typically converges after only a dozen iterations. The stellar spectrum is divided by the telluric transmission spectrum, which strongly reduces the equivalent width of telluric lines.

In the calcium infrared triplet lines located at 8498, 8542, and 8662 Å, the differences between corrected and uncorrected data are small, but this is not true for the Hα line. Earth's barycentric motion in the direction of HD 189733 changes from $-22.3\,\mathrm{km\,s^{-1}}$ in April to $+8.4\,\mathrm{km\,s^{-1}}$ in August, which causes H_2O absorption lines with equivalent widths of 3.5 and 4.5 mÅ to drift across the stellar Hα line. This is on the order of the observed changes in the equivalent width of the Hα line, therefore a proper correction is vital for our analysis. We note that the depth of an unsaturated telluric line can be modeled with an accuracy of better than 2% (Smette et al. 2015). This corresponds

to an error of about 0.1 mÅ in the Hα equivalent width, which is small compared to the typical error margin. Therefore, telluric residuals introduce only a negligible error on the line equivalent width that is studied in the following.

3.3. Derivation of the excess emission

Stellar chromospheric variations and planetary absorption manifest themselves as (subtle) changes in the equivalent width of sensitive lines. Calcium and hydrogen lines are among the most common stellar activity indicators. To subtract photospheric contributions, we compute the excess equivalent width within the cores of activity sensitive lines after the subtraction of an inactive template spectrum. Our template star is HD 10476 (see Fig. 2 for a comparison). In general, HD 10476 and HD 189733 are very similar, but HD 10476 is 2.4 mag brighter. A detailed listing of its properties can be found in Table 4. While metallicity and surface gravity are identical within the error bars, this is not true for the effective temperature (cf. Tables 1 and 4). As pointed out by Martin et al. (2017), the effective temperature difference has a negligible effect on our results. Our template star is an inactive, slow rotator with a $\log(R'_{\rm HK}) = -5.092$. While small emission cores are visible in the Ca H&K lines, the core emission is much stronger in HD 189733. This leads to a systematic but constant underestimation of the absolute excess flux. Since we are only interested in the temporal evolution of the Hα excess, we could in principle also take an average spectrum of HD 189733 or a stellar model atmosphere as template. This would only cause a vertical offset of the data points in Fig. 1.

We follow the analysis of Martin et al. (2017) and summarize only the most important steps. After telluric correction, we normalize the spectra. In the case of the Hα line, we select the wavelength region from 6551 to 6580 Å. Inside this region we regard the upper envelope as continuum data points. To this envelope we fit a linear function that we use to normalize the whole region. Next, we perform a wavelength shift to bring object and template to a common wavelength grid by cross-correlating them. The template spectrum is artificially broadened to match the rotational broadening of HD 189733. Then we subtract the template from our HD 189733 observations. In most wavelength ranges, the residuals are zero within the error bars, but chromospheric excess emission of HD 189733 is present in the cores of activity sensitive lines. Next, we integrate the excess flux in the line cores using a 2 Å band in Hα and a 1.5 Å band in the other lines. The bands are chosen by visual inspection to cover the strongest excess flux in the line cores. The result is the excess equivalent width (see Table 2), which we use as activity indicator. The average S/N of the excess equivalent widths is about 18 in the Ca H&K, 36 in the Ca IRT, and 22 in the Hα region.

4. Results

4.1. Time series

In Fig. 1 we show the temporal evolution of the measured excess equivalent widths of the Hα, Ca infrared triplet (IRT), and Ca H&K lines; the individual IRT and H&K equivalent widths are averaged. Clearly, all three time series are correlated, which we investigate in Sect. 4.3. Livingston et al. (2007) observed a similar behavior in solar lines. In HD 189733 the amplitude of the variation is about 100 mÅ in Ca H&K, 150 mÅ in Ca IRT, and 50 mÅ in Hα. The solar variation in these lines is much smaller: 30 mÅ in Ca K, 8 mÅ in Ca 8542, and 7 mÅ in Hα (see Figs. 11 and 12 in Livingston et al. 2007).

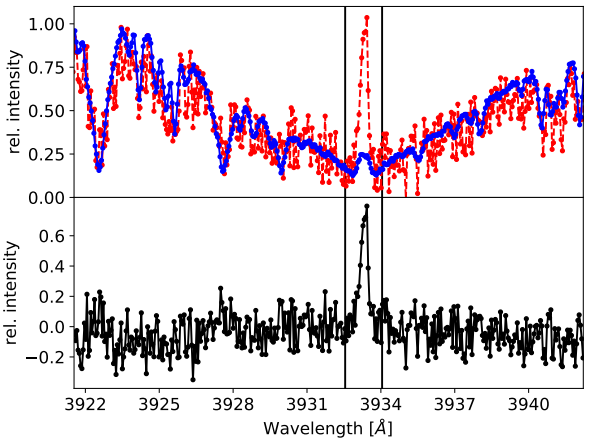

Fig. 2. *Upper panel*: comparison of the Ca K line in HD 189733 (dashed red) and HD 10476 (solid blue). *Lower panel*: chromospheric excess spectrum of HD 189733 after the subtraction of HD 10476. The vertical lines denote our 1.5 Å integration band.

Table 4. Parameters of template star HD 10476.

Parameter	Value	References
Spectral type	K1V	1
$m_{\rm V}$	5.24	1
$M_{\rm V}$–$M_{\rm B}$	0.84	1
$T_{\rm eff}$	5155	2
$\log(g)$	4.48	2
(M/H)	0.03	2
$v_{\rm rot}\sin(i)^a$ (km s^{-1})	0.8 ± 1.2	6
$v_{\rm rad}$ (km s^{-1})	-33.84 ± 0.08	1
Parallaxes (mas)	132.76 ± 0.50	1
$\log(R'_{\rm HK})$	−5.092	5
Epoch of obs. (yr)	2015.85	
Exposure time (s)	1429	

Notes. [(a)]When several values were listed for a stellar parameter, we averaged all given values, discarding outliers however.
References. (1) Wenger et al. (2000); (2) Soubiran et al. (2010); (5) Gray et al. (2006); (6) Głębocki & Gnaciński (2005).

4.2. Periodogram analysis

In the Sun, activity variations are related to spots, faculae, and other surface features, which have lifetimes ranging from several days to months (Hathaway & Choudhary 2008). Van Driel-Gesztelyi & Green (2015) conclude that bigger sunspot groups[1] take longer to decay, so that larger active regions can modulate solar activity over several solar rotations.

Assuming that HD 189733 behaves similar to the Sun, an isolated activity feature causes modulation of the stellar activity indicators related to the star's rotation phase. To account for the limited lifetimes of active regions, we split our time series into shorter subsamples. To that end, we visually investigate the best-fit sine waves and introduce a subsample where phase shifts are apparent. This procedure is repeated until the data are well reproduced by sine waves, which leads to five subsamples (see Fig. 1).

[1] We are strictly speaking about the time it can be identified in magnetic field observations.

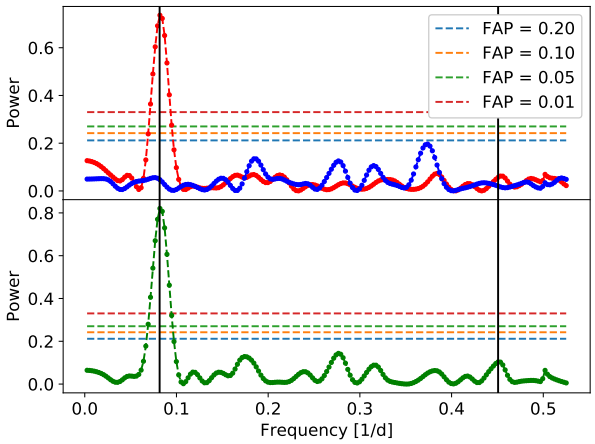

Fig. 3. *Upper panel*: periodogram of the Hα excess equivalent width based on data of subsample 1 (red). The same data, but corrected for chromospheric activity are also shown (blue). The horizontal lines denote the false alarm probabilities. The vertical lines represent the stellar rotation period and the planetary orbit period (from low to high frequency). *Lower panel*: identical, but for the average Ca IRT equivalent width.

For each subsample we calculate periodograms of all three excess equivalent width time series using the algorithm given in Zechmeister & Kürster (2009). Only during the middle of the rainy season do we have too few observations for the periodogram analysis, which corresponds to sample number 4. We focus our description on the first time interval from April 28 until June 6 that visually shows a clear sinusoidal variation. The periodogram for the Hα line is shown in Fig. 3. The strongest peak is located at 12.2 ± 0.3d. This value is in good agreement with the photometric rotation period of 11.953 ± 0.009 days reported in Henry & Winn (2008). We repeated this analysis also for the Ca IRT and found an almost identical value of 12.2 ± 0.2 days.

We then repeat this analysis for subsamples 2, 3, and 5. Here the variation is less pronounced, most likely because the active region causing the strong modulation during the first subsample decayed and new active regions formed that are more evenly distributed over different longitudes. In most cases the stellar rotation period is recovered but with a larger error bar (see Table 5). The rotation periods derived from Hα and Ca IRT are identical within the error bars. The only exception is Ca IRT in subsample 2, where the strongest peak is located at 34 days, but a slightly smaller peak also occurs at about 12 days. We note that subsample 2 was problematic due to relatively large data gaps in our time series (see Fig. 1). We omit a discussion of the Ca H&K results, because they provide the lowest S/N.

While the rotation periods agree within their error bars, this is not true for the rotation phases at T_0, which we define as midnight of July 1 2017. Thus, T_0 in Table 5 is the rotation phase at this date. A natural explanation is the dynamical nature of stellar active regions. Figure 1 shows that a single sine wave typically describes two to three rotation periods adequately. This would correspond to mean active region lifetimes of about 20–30 days, which is in agreement with the lifetime of large sunspot groups (Hathaway & Choudhary 2008). The phases of the different lines are mostly in agreement within the error bars, again with the exception of the second subsample of the Ca IRT series. To verify our solutions, we phase-folded the data of every subsample accounting for the phase jumps. This exhibits a clear phase-dependent modulation in the Hα excess equivalent width on the order of 50 mÅ (see Fig. 4).

Table 5. Dominant rotation periods.

Parameter	Value
Subsample 1	
Date range (BJD)	2457872–2457915
No. of data points	41
Best Hα sine period (d)	12.2 ± 0.3
False alarm probability	2e−10
Hα rotation phase at T_0	0.19 ± 0.18
Ca IRT rotation phase at T_0	0.21 ± 0.13
Best Ca IRT sine period (d)	12.2 ± 0.2
False alarm probability	1e−13
Subsample 2	
Date range (BJD)	2457915–2457955
No. of data points	21
Best sine period (d)	12.2 ± 0.6
False alarm probability	9e−03
Hα rotation phase at T_0	0.64 ± 0.03
Ca IRT rotation phase at T_0	$0.0^b \pm 0.6$
Best Ca IRT sine period (d)	$34^b \pm 2$
False alarm probability	3e−04
Subsample 3	
Date range (BJD)	2457955–2458000
No. of data points	23
Best sine period (d)	13.1 ± 0.7
False alarm probability	3e−03
Hα rotation phase at T_0	0.02 ± 0.03
Ca IRT rotation phase at T_0	0.06 ± 0.02
Best Ca IRT sine period (d)	13.1 ± 0.6
False alarm probability	6e−05
Subsample 5	
Date range (BJD)	2458050–2458077
No. of data points	16
Best sine period (d)	11.7 ± 0.7
False alarm probability	1e−04
Hα rotation phase at T_0	0.30 ± 0.02
Ca IRT rotation phase at T_0	0.39 ± 0.02
Best Ca IRT sine period (d)	11.1 ± 0.6
False alarm probability	1e−03

Notes. [a] T_0 denotes the stellar rotation phase at July 1 2017. [b] Visual inspection of the periodogram shows that there are three almost equal strong peaks ranging between 10 and 34 days.

4.3. A search for planetary Hα absorption

Our Hα time series is clearly dominated by stellar activity with an amplitude of about 50 mÅ, which strongly exceeds the planetary signal between 7 and 10 mÅ observed by Cauley et al. (2015, 2016). However, Fig. 1 shows a clear correlation between the hydrogen- and calcium-based activity indicators, which can be used to derive an activity-corrected Hα equivalent width. We base this correction on the Ca IRT lines, because they exhibit a larger S/N than the H&K lines. The analysis of Cauley et al. (2015, 2016) basically includes a first order activity correction, because the authors use the nightly out-of-transit data in the computation of the residual equivalent width. This

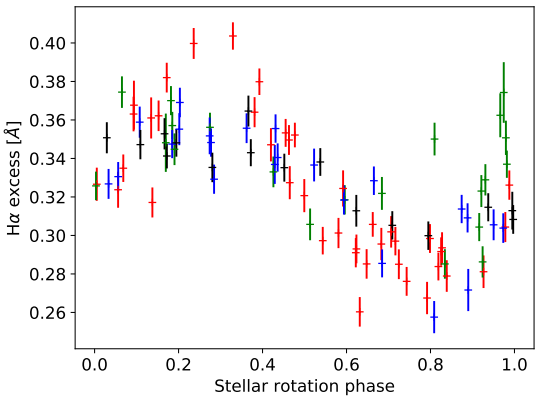

Fig. 4. Hα excess folded on stellar rotation period within each subsample individually. The colors of the data points are identical to the subsamples denoted in Fig. 1.

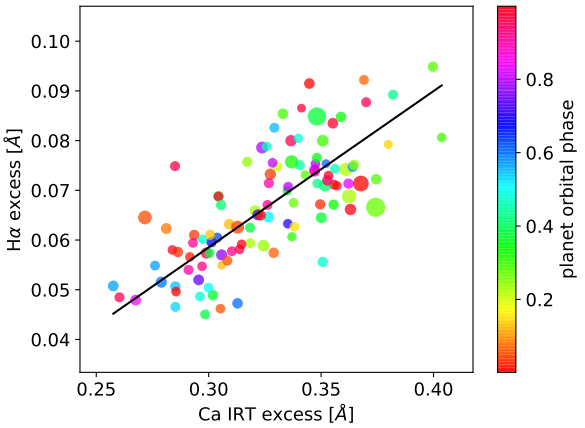

Fig. 5. Correlation between excess equivalent width in Hα and the average Ca IRT excess. Black line: best linear fit between the quantities. The colors of the data points correspond to the phase angle of the planet and the sizes correspond to the error margins.

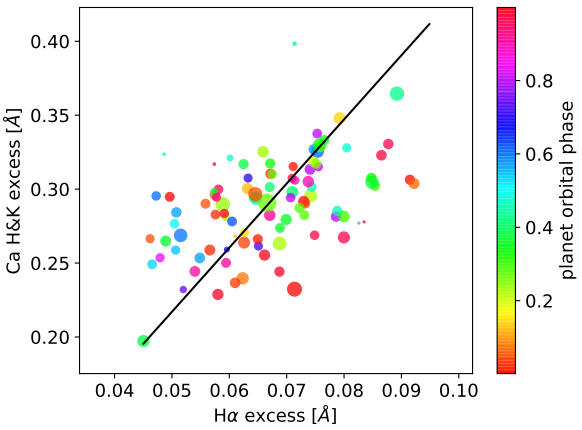

Fig. 6. As Fig. 5, but for Hα against Ca H&K.

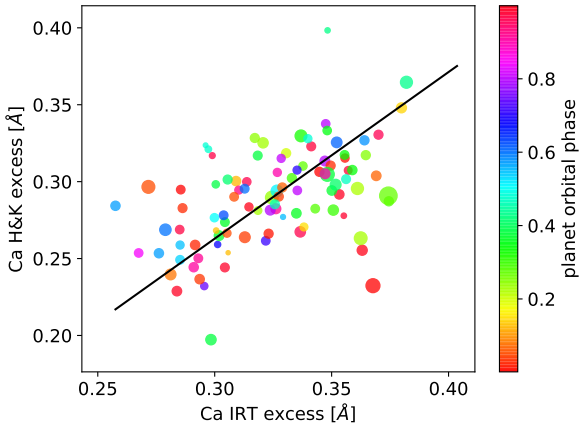

Fig. 7. As Fig. 5, but for Ca IRT against Ca H&K.

removes stellar activity patterns over days and months so that only short-term variations over hours remain in their data.

Using the Ca IRT lines to correct the Hα time series is only valid if calcium is depleted in the upper planetary atmosphere and does not produce an absorption signal by itself. Depletion of calcium in upper planetary atmospheres has been argued by several authors, and, for example, Sing et al. (2016) show a pressure-temperature profile for HD 189733 b in combination with condensation curves of chemical species. According to their results, the atmosphere of HD 189733 is cold enough to allow for the condensation of chemical species like Ca-Ti and Al-Ca. Therefore, it is a reasonable assumption that the upper planetary atmosphere is virtually free of atomic calcium and consequently does not cause any absorption either in Ca H&K no in Ca IRT. We note, however, that this remains an assumption.

Figures 5–7 show the correlations between the Hα, Ca H&K, and Ca IRT excess equivalent widths. Although the data show a significant scatter, positive correlations are obvious between all activity indicators. Pearson's correlation coefficient is 0.74, 0.50, and 0.51 for the three correlations with p-values of 5×10^{-20}, 2×10^{-7}, and 1×10^{-7}, respectively. We fit a simple linear function of the form

$$EW_{\mathrm{H}\alpha} = A\,EW_{\mathrm{IRT}} + B, \tag{1}$$

and find $A = 0.31 \pm 0.03$ and $B = -36 \pm 9$ mÅ for the relation between Hα and Ca IRT. We then subtract the IRT-based expected Hα equivalent width from our data and call the resulting quantity the corrected Hα equivalent width. The periodogram of this value does not show any stellar rotational modulation and the remaining peaks remain below a false alarm probability of 20% (Fig. 3, blue curve). The activity correction also significantly reduces the scatter in the equivalent width values from 11.5 to 7.8 mÅ after the correction.

In Fig. 8 we plot the corrected Hα equivalent width against the planetary phase. A steady bow shock or in-transit absorption would manifest itself as systematically lower values during the corresponding phase. In contrast, we do not find any obvious phase-related variation. For a statistical analysis, we now define three samples. None of the investigations (Jensen et al. 2012; Cauley et al. 2015, 2016) found pre-transit absorption earlier than 4 h before first contact in any of their studies. Therefore, we do not expect any planetary absorption to occur more than 6 h after the end of the transit or 6 h before first contact, which we define as S_{out} sample. This corresponds to phases greater than +0.147 or smaller than −0.147. We further define a bow-shock sample

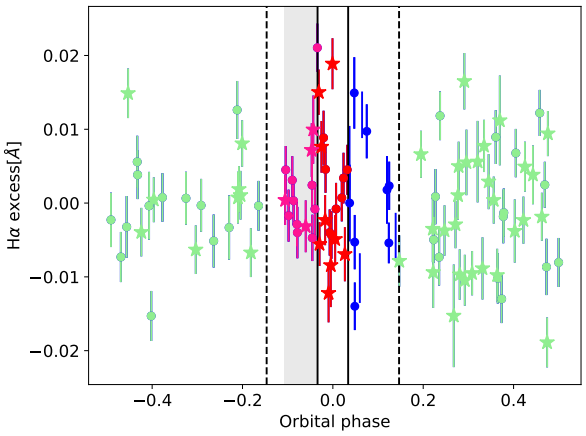

Fig. 8. Phase-folded, corrected Hα excess. The gray shaded area denotes a pre-transit phase of 4 h. The solid vertical lines denote the first and fourth contact. The dashed lines denote the exclusion range of 6 h before first and after the fourth contact. Observations marked with an asterisk denote epochs of high stellar activity, in which the Ca IRT excess is above median.

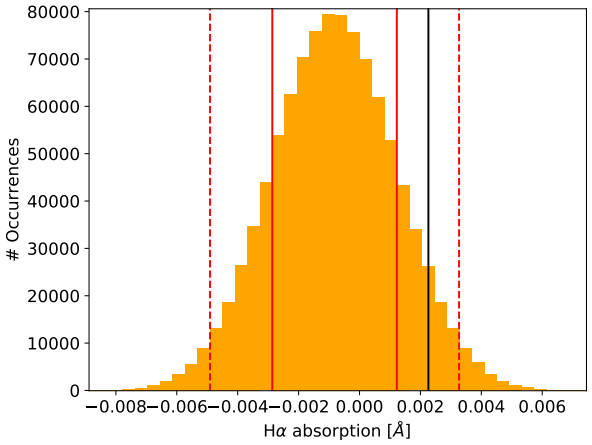

Fig. 9. Distribution of the results for the t-test. The black line denotes the mean of the bow-shock data points, the solid red lines denote the 1σ interval of the distribution, and the dashed red lines denote the 2σ interval.

$S_{\rm bs}$ containing in total 14 data points observed between orbital phases −0.147 and −0.034, and an in-transit sample $S_{\rm in}$ containing all data points between transit phases −0.034 and +0.034.

We use the two-sided Kolmogorov–Smirnov test to check if we can reject the null hypothesis that the samples are drawn from the same distributions. For the bow-shock sample, the test returns

$$D = \sup |F_{\rm bs}(x) - F_{\rm out}(x)| = 0.31, \quad (2)$$

where F_i are the empirical distribution functions of the samples. The p-value is 0.18 and thus we cannot confirm that the bow-shock sample differs from the $S_{\rm out}$ sample. For the in-transit data, the Kolmogorov–Smirnov test returns $D = 0.13$ and $p = 0.97$. So far, our data provide no evidence for the existence of a bow shock or for in-transit absorption.

To further test if the means of $S_{\rm bs}$, $S_{\rm in}$, and $S_{\rm out}$ differ significantly and to derive upper limits, we perform a Monte Carlo analysis. We randomly chose the same number of Hα EWs (equivalent widths) as during the pre-transit phase (14 values) from the $S_{\rm out}$ sample and determine their mean for 10^6 draws. The resulting distribution of means is shown in Fig. 9. The mean of the $S_{\rm bs}$ sample shows a positive deflection between the 1 and 2σ interval of the distribution, which consistently provides no evidence for different parent distributions underlying $S_{\rm bs}$ and $S_{\rm out}$. Additionally we calculated $S_{\rm bs,h} = 4 \pm 5$ mÅ and $S_{\rm bs,l} = 2 \pm 7$ mÅ, where $S_{\rm bs,h}$ is the bow-shock sample obtained during periods of high stellar activity and $S_{\rm bs,l}$ likewise but during low stellar activity. As dividing line we adopt the median activity level. Since both values are identical within their error bars, we are confident that the stellar activity level does not alter our results substantially. Ninety-nine percent of the mean values are found within ± 6.1 mÅ around the peak of the distribution. Therefore, we exclude the presence of a bow shock causing excess Hα absorption with a depth of more than 6.1 mÅ during our observing season.

We repeat the analysis for the in-transit data, finding a mean of the in-transit values of 0.8 mÅ, that is, inside the 1σ interval of the distribution from $S_{\rm out}$. Likewise we obtain $S_{\rm in,h} = 0 \pm 10$ mÅ and $S_{\rm in,l} = 2 \pm 4$ mÅ. Again, we do not find any statistically significant dependence between the Hα flux and the stellar activity level. Here we place an upper limit of 5.6 mÅ for the maximal in-transit Hα absorption caused by the planetary atmosphere with a 99% confidence. The in-transit upper limit holds for an average absorption depth during the in-transit phases; we do not attempt to include further effects like center-to-limb variations in the stellar Hα line in the current analysis (see, e.g., Czesla et al. 2015).

We additionally investigated if data taken during high- and low-activity epochs differ significantly. We find $S_{\rm out,h} = -1 \pm 8$ mÅ and $S_{\rm out,l} = -1 \pm 7$ mÅ. This shows that also the out-of-transit data are not significantly affected by stellar activity.

5. Summary and conclusions

We have collected a large, high signal-to-noise spectral dataset of HD 189733 in the observing season 2017 to search for excess Hα absorption around the transit of the hot Jupiter. Our observations randomly cover the full planetary orbit. We have determined the stellar equivalent width in the Hα, Ca IRT, and Ca H&K lines and find clear evidence for stellar rotation-dominated variation. Based on the correlation between the Hα and Ca IRT equivalent widths, we derive a corrected Hα equivalent width that is free of stellar rotational modulation. In this dataset we find no evidence for the existence of a bow shock or in-transit absorption, and we place upper limits of 6.1 and 5.6 mÅ for any excess absorption during these phases with 99% confidence.

The available literature on the topic provides values of 7 and 10 mÅ bow-shock absorption and 14 mÅ in-transit absorption derived from individual transit observations (Jensen et al. 2012; Cauley et al. 2016, 2015). If calcium is indeed depleted in the upper atmosphere of HD 189733, our results exclude that such strong planetary absorption occurs on a regular basis. If the Ca IRT is absorbed in the planetary atmosphere in a similar way to the Hα line, our removal of stellar rotation-based activity variation would also remove any planetary signal. Of course, we also cannot exclude that individual transits differ from our results, for example, if strong flares or coronal mass ejections were to trigger an excited state of the planetary atmosphere. Nevertheless, our results favor the interpretation of

Barnes et al. (2016), who observed that variations in the stellar Hα profile are dominated by stellar activity and that the average atmosphere of HD 189733 b causes no large Hα absorption signals.

Acknowledgements. This research has made use of the SIMBAD database and the VizieR catalog access tool, operated at CDS, Strasbourg, France, the Exoplanet Orbit Database and the Exoplanet Data Explorer at exoplanets.org, the NA SA Exoplanet Archive, which is operated by the California Institute of Technology, under contract with the National Aeronautics and Space Administration under the Exoplanet Exploration Program, PyAstronomy and NASA's Astrophysics Data System. S.K., M.S., and S.C. acknowledge support by DFG SCHM 1032/57-1, DLR 50OR1710, BMBF 500R 1505, DFG Schm 1032/66-1, and DFG Schm 1382/2-1.

References

Akeson, R. L., Chen, X., Ciardi, D., et al. 2013, PASP, 125, 989
Baluev, R. V., Sokov, E. N., Shaidulin, V. S., et al. 2015, MNRAS, 450, 3101
Barnes, J. R., Haswell, C. A., Staab, D., & Anglada-Escudé, G. 2016, MNRAS, 462, 1012
Boisse, I., Moutou, C., Vidal-Madjar, A., et al. 2009, A&A, 495, 959
Bonfanti, A., Ortolani, S., & Nascimbeni, V. 2016, A&A, 585, A5
Bourrier, V., Lecavelier des Etangs, A., Dupuy, H., et al. 2013, A&A, 551, A63
Cauley, P. W., Redfield, S., Jensen, A. G., et al. 2015, ApJ, 810, 13
Cauley, P. W., Redfield, S., Jensen, A. G., & Barman, T. 2016, AJ, 152, 20
Cauley, P. W., Redfield, S., & Jensen, A. G. 2017, AJ, 153, 185
Czesla, S., Klocová, T., Khalafinejad, S., Wolter, U., & Schmitt, J. H. M. M. 2015, A&A, 582, A51
Ehrenreich, D., Lecavelier Des Etangs, A., Hébrard, G., et al. 2008, A&A, 483, 933
Ehrenreich, D., Bourrier, V., Wheatley, P. J., et al. 2015, Nature, 522, 459
Głębocki, R., & Gnaciński, P. 2005, in 13th Cambridge Workshop on Cool Stars, Stellar Systems and the Sun, eds. F. Favata, G. A. J. Hussain, & B. Battrick, ESA SP, 560, 571
Gray, R. O., Corbally, C. J., Garrison, R. F., et al. 2006, AJ, 132, 161
Han, E., Wang, S. X., Wright, J. T., et al. 2014, PASP, 126, 827
Hathaway, D. H., & Choudhary, D. P. 2008, Sol. Phys., 250, 269
Henry, G. W., & Winn, J. N. 2008, AJ, 135, 68
Jensen, A. G., Redfield, S., Endl, M., et al. 2012, ApJ, 751, 86
Kulow, J. R., France, K., Linsky, J., & Loyd, R. O. P. 2014, ApJ, 786, 132
Lammer, H., Selsis, F., Ribas, I., et al. 2003, ApJ, 598, L121
Lecavelier Des Etangs, A., Ehrenreich, D., Vidal-Madjar, A., et al. 2010, A&A, 514, A72
Livingston, W., Wallace, L., White, O. R., & Giampapa, M. S. 2007, ApJ, 657, 1137
Martin, J., Fuhrmeister, B., Mittag, M., et al. 2017, A&A, 605, A113
Mittag, M., Hempelmann, A., González-Pérez, J. N., & Schmitt, J. H. M. M. 2010, Adv. Astron., 2010, 101502
Morello, G., Waldmann, I. P., Tinetti, G., et al. 2014, ApJ, 786, 22
Noll, S., Kausch, W., Barden, M., et al. 2013, The Cerro Paranal Advanced Sky Model
Pace, G. 2013, A&A, 551, L8
Piskunov, N. E., & Valenti, J. A. 2002, A&A, 385, 1095
Rothman, L. S., Gordon, I. E., Barbe, A., et al. 2009, J. Quant. Spectr. Rad. Transf., 110, 533
Salz, M., Czesla, S., Schneider, P. C., & Schmitt, J. H. M. M. 2016, A&A, 586, A75
Schmitt, J. H. M. M., Schröder, K.-P., Rauw, G., et al. 2014, Astron. Nachr., 335, 787
Sing, D. K., Fortney, J. J., Nikolov, N., et al. 2016, Nature, 529, 59
Smette, A., Sana, H., Noll, S., et al. 2015, A&A, 576, A77
Soubiran, C., Le Campion, J.-F., Cayrel de Strobel, G., & Caillo, A. 2010, A&A, 515, A111
Van Driel-Gesztelyi, L., & Green, L. M. 2015, Liv. Rev. Solar Phys., 12, 1
Vidal-Madjar, A., Lecavelier des Etangs, A., Désert, J.-M., et al. 2003, Nature, 422, 143
Watson, A. J., Donahue, T. M., & Walker, J. C. G. 1981, Icarus, 48, 150
Wenger, M., Ochsenbein, F., Egret, D., et al. 2000, A&AS, 143, 9
Zechmeister, M., & Kürster, M. 2009, A&A, 496, 577